Studies on Integrated Optics Design for Diffraction Limited Light Sources

Ji Li

Hertford College

University of Oxford

Thesis submitted in fulfilment of the requirements for the degree of Doctor of Philosophy at the University of Oxford

Hilary Term, 2021

Abstract

After more than a decade of operation, the Diamond Light Source (DLS) is planning an upgrade to the next generation of diffraction limited synchrotron light sources based on an ultra-low emittance accelerator lattice design. The optimisation of the photon beam properties like flux, brilliance and coherence of the light generated in the storage ring (SR), is a key driver for the storage ring design. The key performance parameters (KPP) characterizing the photon beamlines (BL) define the requirements on the electron beam and on the storage ring design. The storage ring design is supported by the development of optimisation tools that allow the simultaneous modelling of the photon and the electrons beams.

A strategy has been developed to bridge the gap between storage ring lattice and beamline needs, based on an integrated approach of accelerator physics tracking codes (ELEGANT) and of radiation codes (SRW, SHADOW). Python is the interface for these codes. This thesis presents the integrated approach used to track electron beams and propagate the synchrotron radiation wavefronts through the beamline. The optimisation of the performance of the beamline is achieved by using multi-objective genetic algorithms. Such an integrated approach is new and promises to achieve the best exploitation of the beamlines, by tailoring the photon beams to the need of the applications.

This thesis is dedicated to my parents.

Acknowledgements

First of all, I would like to express my deepest gratitude to my DPhil supervisor, Prof. Riccardo Bartolini, for his support, guidance, patience and understanding throughout my doctoral research in the University of Oxford. His broad knowledge and excellent experience always guide me in the right way to approach a problem. I would also like to express gratitude to Prof. Philip Burrows for his kind support and advice at the final stage of my study.

Many people at Diamond have supported me during this project, especially Dr. Marco Apollonio who has provided me with continued guidance and suggestions for the studies taken in the Diamond Light Source. A big thank to Dr. Faissal Bakkali Taheri who has been tremendously generous with his time and knowledge, I have benefited greatly from many useful discussions with him. Similarly, I would like to thank all the members in the Accelerator Physics Group at Diamond Light Source who have been providing me with helpful suggestions. I also wish to acknowledge the kind help from Beamline I13 Group, the Engineering Group, Lucia Alianelli and Hongchang Wang in the Optics Group.

Furthermore, I would like to thank Xia. Liu, a Senior Mechanical Project Engineer at Diamond Light Source who was always patient to give me advice and motivate me both in study and life. I would also like to express a special thank to the department secretaries: Sue Geddes, Kim Proudfoot

and Hertford college for their excellent administrative assistance since the beginning of my study at the University of Oxford.

Last but not least, I would like to thank my family as a whole, to my parents and my husband in particular. Their love and support have continuously driven me forward in the challenging times and inspired me to be a physicist.

Contents

List of Figures

Chapter 1

Introduction and motivations

1.1 Background of sychrotron radiation

The theoretical prediction of the properties of synchrotron radiation was first developed by Liénard in 1898 [1]. In 1947, the first synchrotron radiation light was observed at a 70 MeV synchrotron at General Electric [2]. In 1949, Schwinger gave a full description of the radiation from a charged particle moving in a circle [3].

Later, in 1956, the first spectroscopy experiments using radiation from an accelerator were carried out. From then on, synchrotron radiation became a very powerful tool for research on material structure and composition. In the 1950s and 1960s, synchrotron radiation research was based on modified particle accelerators. This is considered as the first generation synchrotron radiation light sources, sometimes also called parasitic facilities because the accelerators were operated primarily for nuclear physics research. As the number of synchrotrons with budding synchrotron radiation devices continued to grow, the next major improvement was the development of electron storage rings (SR), which are the foundation of all synchrotron sources today.

With the successful use of synchrotron radiation in different research areas, equipment optimised for its production and specially designed for its use had begun to appear. In the second generation of synchrotron radiation light sources, the light is

produced by bending the electron beam in dedicated dipole magnets. However, the radiation from dipoles is broadband and has a wide angular distribution, therefore only a fraction of the photon beam can be used [4].

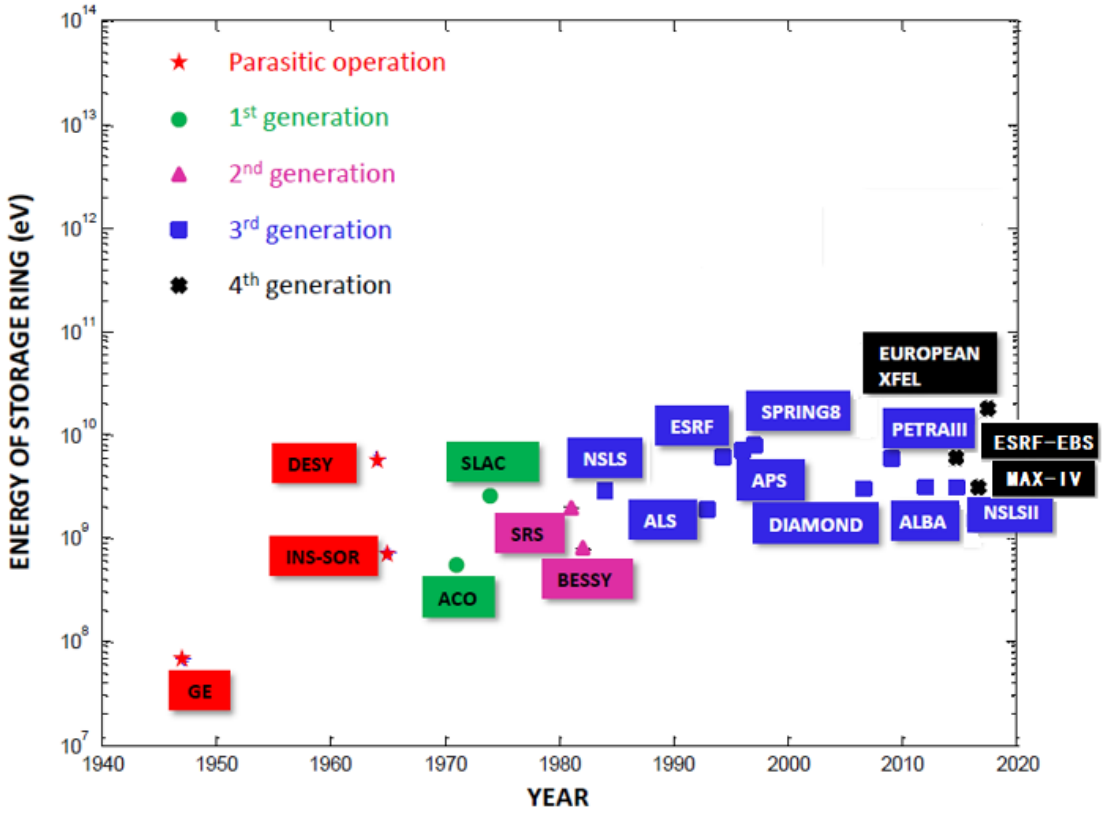

Figure 1.1: Development of synchrotron radiation facilities from first generation (depends on the facility of nuclear physics experiments) to the third generation (modern facilities commonly used today). Several fourth generation light sources are also shown. (Revised from [5]).

Since then experiments have been requiring better photon beam quality, with a typical increment in brightness by several orders of magnitude. Brightness is a physical quantity that indicates how well a photon beam can be focused. Enhanced brightness can be achieved by reducing the emittance of a synchrotron radiation light source. The emittance is an intrinsic property of the electron beam, used to measure its size and angular divergence. As we will see in the following chapter, a lower emittance results in a brighter synchrotron light source.

Modern storage rings are the third generation synchrotron radiation sources which provide highly collimated and narrow photon beams. They are designed not only for lower emittance but also optimised for the use of insertion devices such as undulators and wigglers. A detailed description of insertion devices will be introduced in section 1.2.2. There are now about 50 operational synchrotron light sources of all generations in 14 countries, 10 of which are classifiable as third generation sources [6]. Fig. 1.1 traces the progress of the synchrotron radiation facilities from 1947 to present, which includes fourth generation light sources [5].

Fourth generation light sources are designed to achieve ′ultra-low′ emittance and high brightness with innovative magnetic sequence design. ′Ultra-low′ emittance rings and free electron lasers (FEL) comprise fourth generation light sources [6].

1.2 Synchrotron radiation

Synchrotron radiation is the radiation generated by an ultra-relativistic electron beam travelling through a magnetic field [7]. The characteristics of the photon beam from the synchrotron radiation source are mainly defined by the electron beam parameters at the photon beam source, which are bending magnets or insertion devices. The general characteristics of synchrotron radiation including the radiation field, the photon flux density, power density, brilliance, intensities and coherence will be derived in the following subsections.

1.2.1 Synchrotron radiation from dipole magnets

The spectral and angular characteristics of synchrotron radiation can be described from the photon flux in the unit vector $\widehat{n}$ (Fig. 1.2) direction per unit solid angle and unit relative frequency bandwidth for an electron in arbitrary motion as described in [7]:

$$\frac{d\Phi}{d\Omega d\omega/\omega} = \alpha\frac{I}{e}|H(\hat{n},\omega)|^2 \tag{1.1}$$

where Φ is the photon flux in number of photons per second, Ω is the solid angle in steradians, ω is the frequency in Hz. α is the fine structure constant ($e^2/4\pi\epsilon_0\hbar c = 1/137$), I is the beam current (A) and e is the electron charge in Coulomb. $\vec{H}(\hat{n},\omega)$ is a dimensionless field vector which is directly related to the radiation amplitude, and is given by

$$\vec{H}(\hat{n},\omega) = \frac{\omega}{2\pi}\int_{-\infty}^{\infty}\hat{n}\times(\hat{n}\times\vec{v})\exp[i\omega(\tau - \frac{\hat{n}\cdot\hat{R}}{c})]d\tau \tag{1.2}$$

where $\vec{R}$ is the position of the electron with respect to the origin, and $\vec{v}$ is its velocity. In the horizontal-longitudinal plane, the observation point is orthogonal to the electron acceleration at some time $\tau = 0$ and making an angle θ with respect to the plane of motion, as shown in Fig. 1.2.

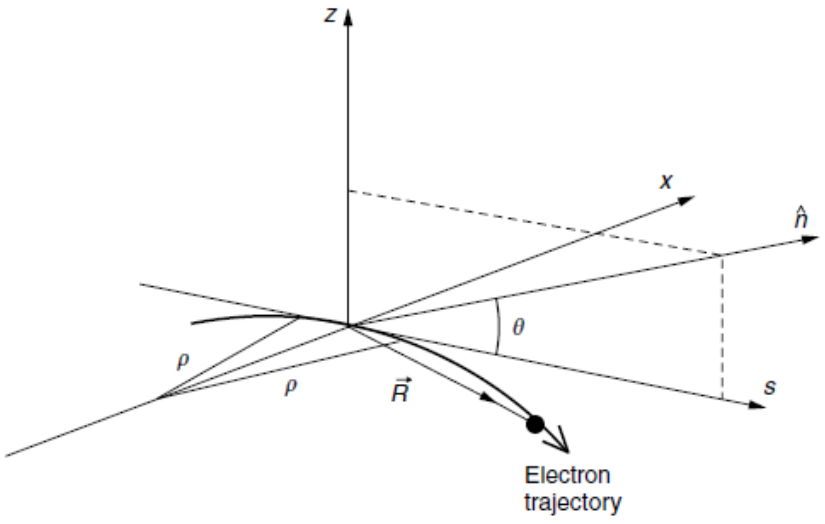

Figure 1.2: The coordinate system of the moving charged particle. (Reprint from [7]).

Since only small angles and times around 0 are considered, the expression for the radiation amplitudes can be approximated by:

$$H_x = \frac{\omega}{2\pi}\frac{\rho}{c}(\frac{1}{\gamma^2}+\theta^2)\int_{-\infty}^{\infty} x\exp\{i\frac{3\xi}{2}(x+\frac{x^3}{3})\}dx$$
$$H_z = \frac{\omega}{2\pi}\theta\frac{\rho}{c}(\frac{1}{\gamma^2}+\theta^2)^{\frac{1}{2}}\int_{-\infty}^{\infty} \exp\{i\frac{3\xi}{2}(x+\frac{x^3}{3})\}dx \quad (1.3)$$

where

$$x = \frac{c\tau}{\rho}(\frac{1}{\gamma^2}+\theta^2)^{-1/2}$$
$$\xi = \frac{\omega\rho}{3c}(\frac{1}{\gamma^2}+\theta^2)^{3/2} \quad (1.4)$$

Here we introduce the modified Bessel functions which are defined as follows:

$$\int_{-\infty}^{\infty} x\sin[\frac{3\xi}{2}(x+\frac{x^3}{3})]dx = \frac{1}{\sqrt{3}}K_{2/3}(\xi)$$
$$\int_{-\infty}^{\infty} x\cos[\frac{3\xi}{2}(x+\frac{x^3}{3})]dx = \frac{1}{\sqrt{3}}K_{1/3}(\xi) \quad (1.5)$$

which allows to re-write the exponential term in the radiation amplitude,

$$H_x = i\frac{\omega}{\omega_c}\frac{\sqrt{3}\gamma}{2\pi}(1+\gamma^2\theta^2)K_{2/3}(\xi)$$
$$H_z = \frac{\omega}{\omega_c}\frac{\sqrt{3}\gamma^2\theta}{2\pi}(1+\gamma^2\theta^2)^{1/2}K_{1/3}(\xi) \quad (1.6)$$

ω_c is the critical frequency defined by $\omega_c = \frac{3c\gamma^3}{2\rho}$. With $y = \omega/\omega_c$, $X = \gamma\theta$, $\xi = y(1+X^2)^{3/2}/2$, in practical units [photons/s/$mrad^2$/0.1%bandwidth] finally we have

$$\frac{d\Phi}{d\Omega d\omega/\omega} = \frac{3\alpha}{4\pi^2}\frac{I}{e}\gamma^2y^2(1+X^2)^2[K_{2/3}^2(\xi)+\frac{X^2}{X^2+1}K_{1/3}^2(\xi)]$$
$$= 1.327\times10^{13}E[\mathrm{GeV}]^2I[A]y^2(1+X^2)^2[K_{2/3}^2(\xi)+\frac{X^2}{X^2+1}K_{1/3}^2(\xi)] \quad (1.7)$$

The corresponding critical wavelength (λ_c) and critical photon energy (ϵ_c) are

$$\lambda_c[\text{Å}] = \frac{18.6}{B[T]E[\text{GeV}]^2}$$
$$\epsilon_c[\text{keV}] = 0.665B[T]E[\text{GeV}]^2 \tag{1.8}$$

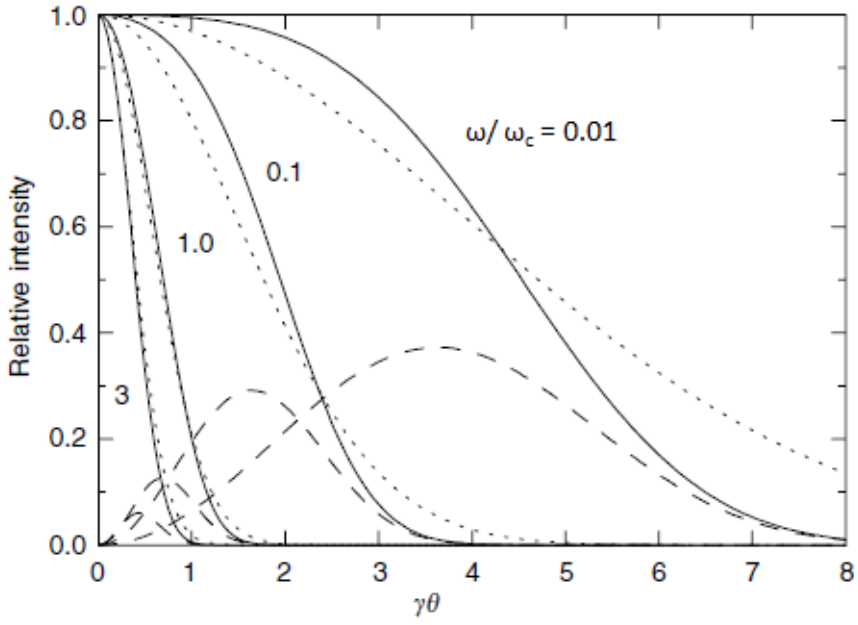

Figure 1.3: Relative intensity of horizontally (solid line) and vertically (dashed line) polarized synchrotron radiation emitted as a function of the angle from the plane of the electron orbit. Dotted line is the horizontal component that is approximated by a Gaussian distribution with the standard deviation. (Reprint from [7]).

Fig. 1.3 shows the angular distribution of the radiation. The intensity is normalized to the peak value on-axis. It is clear that the angular divergence significantly reduces as the radiation frequency increases.

In some experimental situations, the vertical acceptance angle is sufficient to collect all the radiation in the vertical plane, hence it would be convenient to have an expression for the total flux integrated over the vertical angle [7]. By integrating the Eq. 1.7 over the vertical angle, we get the expression for the photon flux per relative bandwidth per unit horizontal angle:

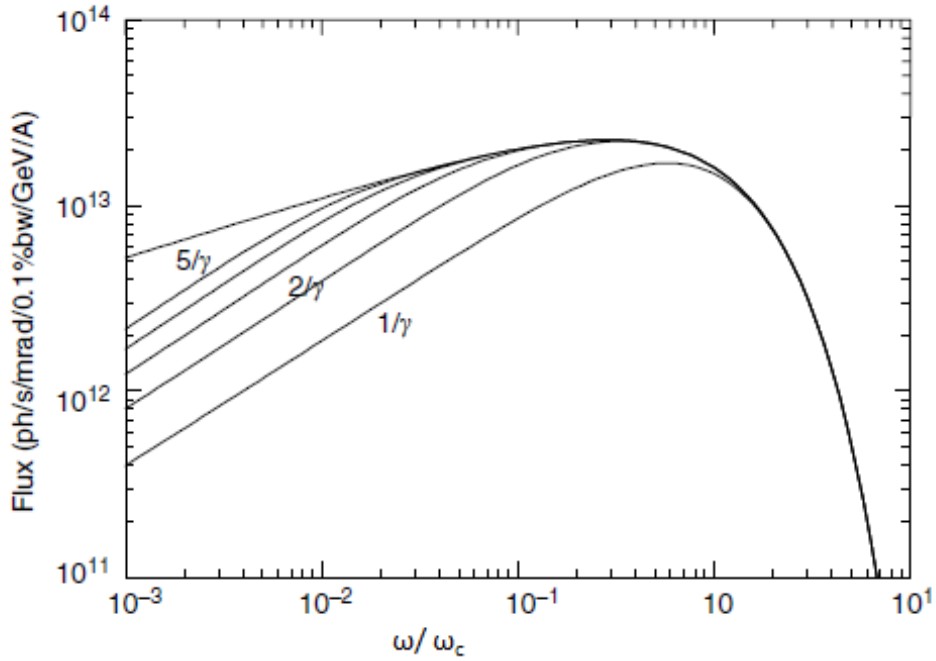

Figure 1.4: The photon flux emitted as a function of the photon beam frequency. (Reprint from [7]).

$$\frac{d\Phi}{d\theta_x d\omega/\omega} = \frac{\sqrt{3}}{2\pi}\alpha\gamma\frac{I}{e}y\int_y^\infty K_{5/3}(y')dy' \tag{1.9}$$

Fig. 1.4 shows the integrated flux curve as a function of the photon beam frequency. The curves are valid for rings of any energy, current and bending magnet field strength.

The angular distribution of the radiation flux as described in Eq. 1.7 can be converted into power units by the following relation [7]:

$$\text{photons/s/0.1\%bandwidth} = \frac{W/eV}{e} \tag{1.10}$$

By integrating Eq. 1.7 over all frequencies, we get the expression of the angular distribution of radiation power P in practical units,

$$\frac{dP}{d\Omega}[W/mm^2] = 5.420E[\text{GeV}]^4 B[T]I[A]\frac{1}{(1+\gamma^2\theta^2)^{5/2}}[1+\frac{5\gamma^2\theta^2}{7(1+\gamma^2\theta^2)}] \tag{1.11}$$

After integrating Eq. 1.11 over all the solid angle, the total power P_T of synchrotron radiation emitted from the bending magnets is therefore:

$$P_T = \frac{e^2}{3\epsilon_0}\frac{\gamma^4}{\rho}\frac{I}{e} = 2.652 \times 10^4 E[\mathrm{GeV}]^3 B[T] I[A] \tag{1.12}$$

Another quantity related to the flux is the radiation brightness B, defined as,

$$B = \frac{\mathrm{Flux}}{(2\pi)^2\sqrt{\sigma_x^2+\sigma_r^2}\sqrt{\sigma_y^2+\sigma_r^2}\sqrt{\sigma_{x'}^2+\sigma_{r'}^2}\sqrt{\sigma_{y'}^2+\sigma_{r'}^2}} \tag{1.13}$$

where $\sigma_x, \sigma_{x'}, \sigma_y, \sigma_{y'}$ are the electron beam size and divergence in the horizontal and in the vertical plane, $\sigma_r, \sigma_{r'}$ are the photon beam size and divergence. Brightness describes the concentration of photons in the phase space and it is a conserved quantity during the transport in an optical system.

1.2.2 Synchrotron radiation from insertion devices

In third generation synchrotrons, insertion devices are commonly used to generate radiation. Undulators and wigglers are two categories of insertion devices. They are made from a number of short dipoles with alternating polarity. The idea of using undulators in high energy synchrotrons and storage rings as a source of X-ray radiation was initially discussed by several authors in [8] [9] [10]. Another interesting use of the periodic magnets is to compensate the interference effect. In this case, the photon spectrum at high photon energies becomes smooth and similar to that of a bending magnet. This development of the wiggler is discussed thoroughly in [11] [12]. In this section, a brief introduction of the radiation from insertion devices will be presented. Fig. 1.5 shows an example of an undulator, where electron position and velocity are periodic functions of s.

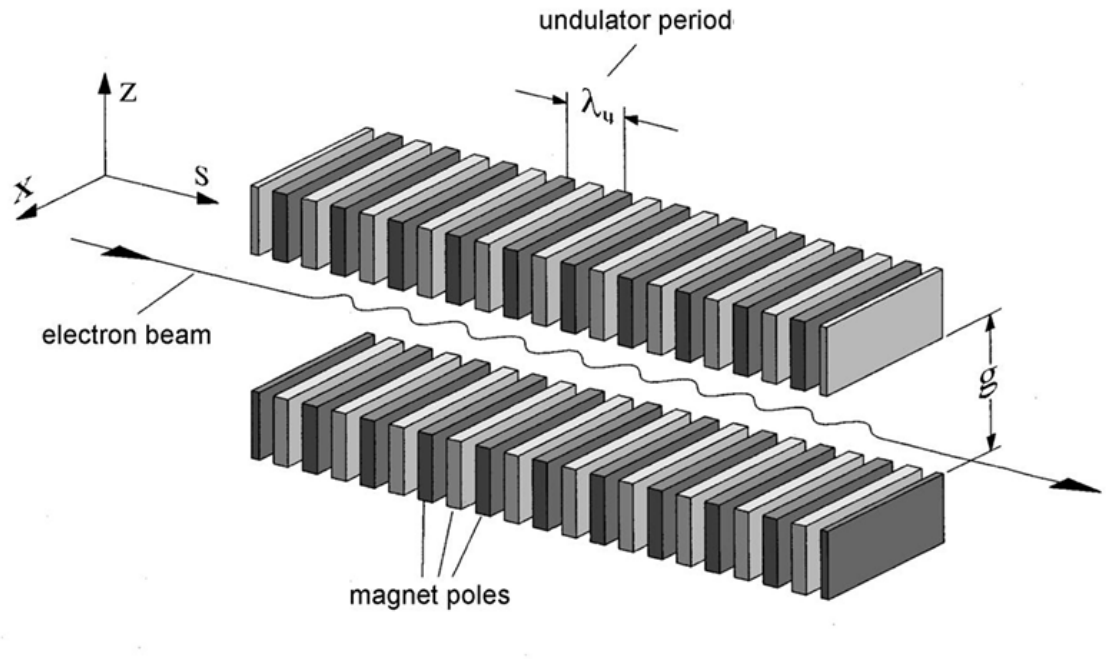

Figure 1.5: Principles of an undulator or wiggler. λ_u is the period length, g is the gap. (Reprint from [13]).

Consider an electron beam travelling through a periodic magnetic field as shown in Fig. 1.5. The vertical field component along the magnet axis is $B_y = B_0 sin(kz)$ where $k = 2\pi/\lambda_u$, λ_u is the undulator period or distance between two equal poles. The simplified electron motion is then:

$$\begin{aligned} \ddot{x} &= \frac{-e}{\gamma m}\dot{s}B_z \\ \ddot{s} &= \frac{e}{\gamma m}\dot{x}B_z \end{aligned} \tag{1.14}$$

We can integrate the $\ddot{x}$ directly:

$$\dot{x} = \frac{eB_0}{\gamma m}\frac{\cos(kz)}{k} \tag{1.15}$$

and hence

$$\beta_x = \frac{\dot{x}}{c} = \frac{K}{\gamma}\cos(kz) \tag{1.16}$$

here K is a dimensionless quantity called the deflection parameter, defined as:

$$K = \frac{eB_0\lambda_u}{2\pi mc} = 93.4B_0[T]\lambda_u[m] \tag{1.17}$$

After considering the interference of wavefronts emitted by the same electron at different points in the magnet, one can express the radiation wavelength [14]:

$$\lambda = \frac{\lambda_u}{2\gamma^2}\frac{1}{n}(1 + \frac{K^2}{2} + \gamma^2\theta^2) \tag{1.18}$$

where n=1,2,3... is the harmonic number. Assume we have an insertion device consisting of N periods in a length of L, with the on-axis wavelength, the width of the radiation can be described [14]:

$$\Delta\theta = \sqrt{\frac{2\lambda}{L}} = \frac{1}{\gamma}\sqrt{\frac{1 + K^2/2}{N}} \tag{1.19}$$

The cone can be significantly smaller in opening angle compared to the bending magnet radiation whose typical aperture goes as $1/\gamma$ [7]. There is not a hard line defining the difference between wigglers and undulators, however a typical definition can be cast from Eq. 1.19,

$$\begin{aligned}\sqrt{\frac{1 + K^2/2}{N}} \leq 1, \Delta\theta \leq 1/\gamma, \text{Undulator} \\ \sqrt{\frac{1 + K^2/2}{N}} > 1, \Delta\theta > 1/\gamma, \text{Wiggler}\end{aligned} \tag{1.20}$$

Therefore, the main difference between undulator and wiggler is the larger magnetic field and longer periodic length in wiggler.

For a filament electron beam passing through an insertion device, in the case of a pure sinusoidal motion [15] [16], the energy radiated per unit frequency per unit solid angle given by Eq. 1.1 can be re-expressed [14]:

$$\frac{d^2\Phi}{d\omega d\Omega} = \frac{e^2\gamma^2N^2}{4\pi\epsilon_0 c}L(\frac{N\Delta\omega}{\omega_r(\theta)})F_n(K,\theta,\phi) \tag{1.21}$$

where $\omega_r(\theta)$ is the resonant frequency, $\Delta\omega = \omega - \omega_r(\theta)$. $F_n(K,\theta,\phi)$ is the integration of the magnetic field over a single period [17]. For the on-axis case, $F_n(K)$ is only proportional to K:

$$F_n(K) = \frac{n^2K^2}{(1+(K^2/2))^2}(J_{(n-1)/2}(\frac{nK^2}{4+2K^2}) - J_{(n+1)/2}(\frac{nK^2}{4+2K^2}))^2 \tag{1.22}$$

$J_n(x)$ is the Bessel Function of the variable x and order n. $L(\frac{N\Delta\omega}{\omega_r(\theta)})$ is the lineshape for each harmonic and can be expressed as,

$$L(\frac{N\Delta\omega}{\omega_r(\theta)}) = \frac{\sin^2(N\pi\Delta\omega/\omega_r(\theta))}{N^2\sin^2(\pi\Delta\omega/\omega_r(\theta))} \tag{1.23}$$

Fig. 1.6 shows the transition from undulator radiation ($K \leq 1$) to wiggler radiation ($K \gg 1$) as a function of photon energy. From the undulator spectral flux we can clearly see that only odd harmonics of the radiation appear, and the spectral lines are very narrow meaning that emission away from harmonics of the resonant frequency is strongly suppressed [17]. With increasing of K, higher photon energies appear. In the wiggler regime one observes a continuous radiation with a spectral flux shape similar to the one of a bending magnet. Fig. 1.7 gives a summary of the electron trajectory, radiation cone size, and spectral flux from bending magnet, undulator and wiggler, respectively.

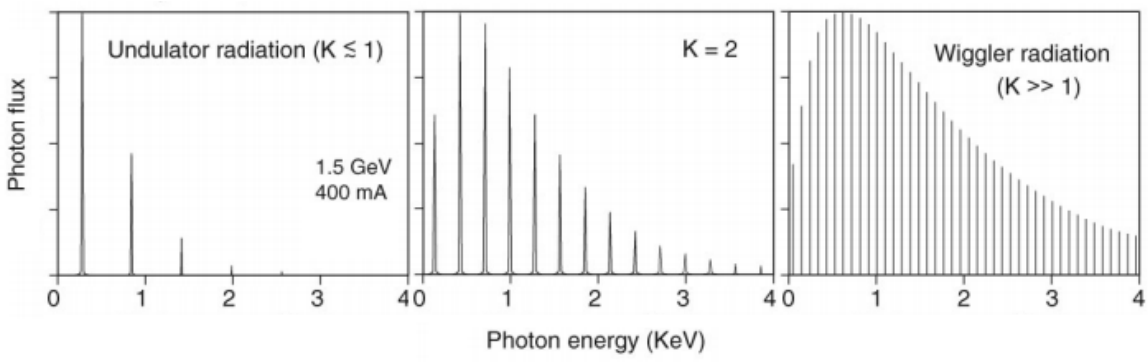

Figure 1.6: The transition from undulator Radiation ($K \leq 1$) to wiggler Radiation ($K \gg 1$) as a function of photon energy. The spectral flux is calculated with a 1.5GeV and 400mA machine and the electron beam is assumed to be zero emittance. (Revised from [18]).

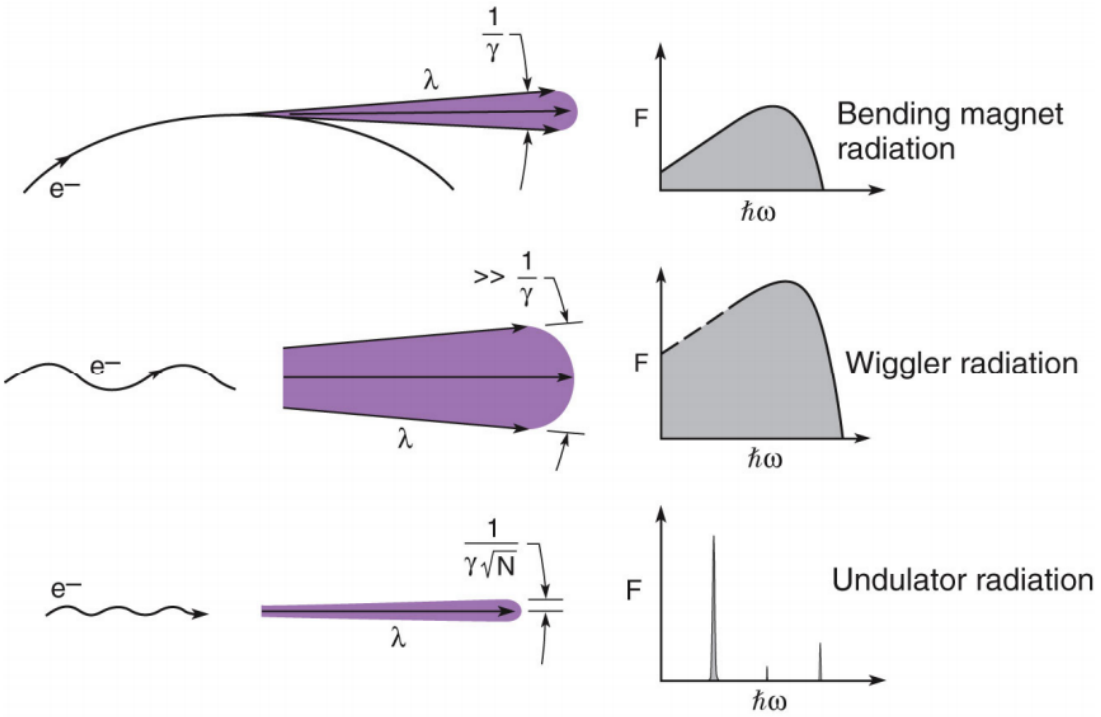

Figure 1.7: Spectral flux from different radiation sources. A sketch of electron trajectories and the radiation cone sizes are also shown. (Reprint from [18]).

The brilliance of the radiation from a bending magnet was described in Eq. 1.13. For undulator sources, the expression of brilliance on-axis for an odd harmonic is [19],

$$B = \frac{\text{Flux}}{(2\pi)^2 \Sigma_x \Sigma_z \Sigma_{x'} \Sigma_{z'}} \tag{1.24}$$

where $\Sigma_x, \Sigma_z, \Sigma_{x'}, \Sigma_{z'}$ are the RMS total beam sizes and divergences for the radiation beam. They are approximated by the convolution of electron beam distribution and photon beam distribution $\Sigma_{x,z}=\sqrt{\sigma_{x,z}^2 + \sigma_r^2}$, $\Sigma_{x',z'}=\sqrt{\sigma_{x',z'}^2 + \sigma_{r'}^2}$. The size and divergence of the photons from the undulator are defined as [7],

$$\begin{aligned} \sigma_r &= \sqrt{\frac{\lambda_u L}{8\pi^2}} \\ \sigma_{r'} &= \sqrt{\frac{\lambda_u}{2L}} \end{aligned} \tag{1.25}$$

Therefore, the two limit cases of Eq. 1.24 are:

i) If $\sigma_r > \sigma_{x,z}$, $\sigma_{r'} > \sigma_{x',z'}$. With long wavelength and small electron beam dimensions and divergences, the photon beam dimensions dominate. This is often referred as the "diffraction limit".

ii) If $\sigma_r < \sigma_{x,z}$, $\sigma_{r'} < \sigma_{x',z'}$. The brilliance is dominated by the electron beam emittance. Then $B = \frac{Flux}{4\pi^2 \epsilon_x \epsilon_y}$, where $\epsilon_x = \sigma_x \sigma_{x'}$ and $\epsilon_y = \sigma_y \sigma_{y'}$ are the emittances in the horizontal and vertical plane, respectively.

Fig. 1.8 shows an example of the brilliance curves of a 5m long undulator. Four odd harmonics are present and the maximum K is 2.4 resulting in a good overlap of the photon energy range covered by the first and the third harmonics.

For various synchrotron radiation experiments, the coherence of the radiation beam is an increasingly important parameter. Basically, there are two measures of coherence, temporal (or longitudinal) coherence and spatial (or transverse) coherence

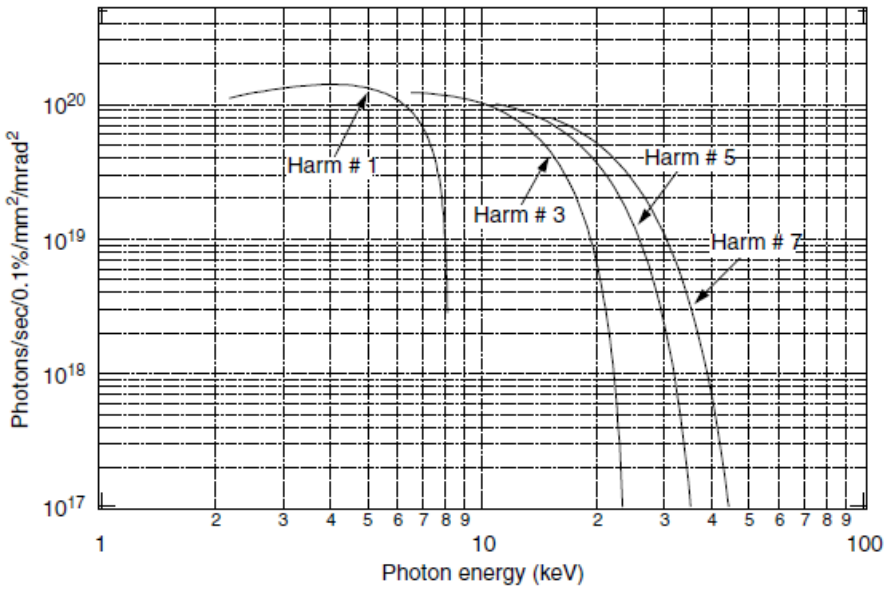

Figure 1.8: Brilliance produced by a 5m long undulator. The maximum K is 2.4. (Reprint from [7]).

[7]. Temporal coherence determines how much the two parts of the beam (one delayed relative to the other) can interfere with each other. It is determined by the degree of monochromaticity of the radiation and is described by the longitudinal coherence length l_c over which waves of different wavelength remain in phase [14],

$$l_c = \frac{\lambda^2}{2\Delta\lambda} \tag{1.26}$$

Spatial coherence determines the interference of two spatially separated parts. It is determined by the phase space transverse area of the source. For undulator radiation, consider a single photon beam from a single electron, the size and divergence of the spatial coherent radiation satisfy $\sigma_z\sigma_{z'} = \lambda/2\pi$. So the partial coherent flux is

$$F_{coh} = B(\frac{\lambda}{2\pi})^2 \tag{1.27}$$

hence the coherent fraction is,

$$\frac{F_{coh}}{F_{tot}} = \frac{(\lambda/2\pi)^2}{(2\pi)^2 \Sigma_x \Sigma_z \Sigma_{x'} \Sigma_{z'}} \tag{1.28}$$

The general formula of power radiated per unit solid angle by a single electron in arbitrary motion in a magnetic field is given in [20]. For electrons with a sinusoidal trajectory, θ and ϕ are the angles of observation in the horizontal and vertical directions, respectively, the formula can be simplified to [21]:

$$\frac{dp}{d\Omega} = \frac{dp^2}{d\theta d\phi} = P_T \frac{21\gamma^2}{16\pi K} G(K) f_k(\gamma\theta, \gamma\phi) \tag{1.29}$$

Here P_T is the total power calculated by integrating over angles and frequencies given by,

$$P_T = \frac{N}{6} Z_0 I \frac{2\pi ec}{\lambda_u} \gamma^2 K^2 = 0.633 E[\mathrm{GeV}]^2 B_0[T]^2 L[m] I[A](kW) \tag{1.30}$$

where N is the number of undulator periods, Z_0 is the vacuum impedance, I is the electron current, e is the electron charge, c is the velocity of light, γ is the Lorentz factor, E is the electron energy, L is the undulator length, and $G(K)$ is a normalization factor given by,

$$G(K) = K \frac{K^6 + \frac{24}{7}K^4 + 4K^2 + \frac{16}{7}}{(1+K^2)^{7/2}} \tag{1.31}$$

$f_k(\gamma\theta, \gamma\phi)$ gives the angular dependence as follows,

$$f_k(\gamma\theta, \gamma\phi) = \frac{16K}{7\pi G(K)} \int_{-\pi}^{\pi} d\alpha \left(\frac{1}{D^3} - \frac{4(\gamma\theta - K\cos\alpha)^2}{D^5}\right) \sin^2\alpha \tag{1.32}$$

where

$$D = 1 + (\gamma\phi)^2 + (\gamma\theta - K\cos\alpha)^2 \tag{1.33}$$

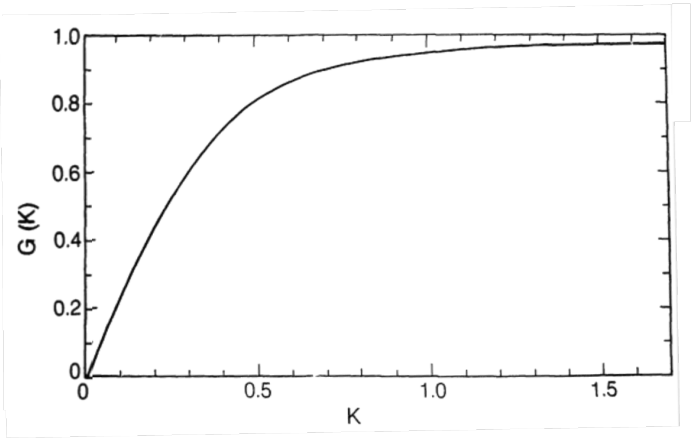

Figure 1.9: The behaviour of the function $G(K)$. (Reprint from [21]).

Fig. 1.9 shows the function $G(K)$, it is close to unity for $K > 1$. The function $f_k(\gamma\theta, \gamma\phi)$ has a peak value of unity on-axis and is shown in Fig. 1.10 in the horizontal and vertical planes for various K values [14].

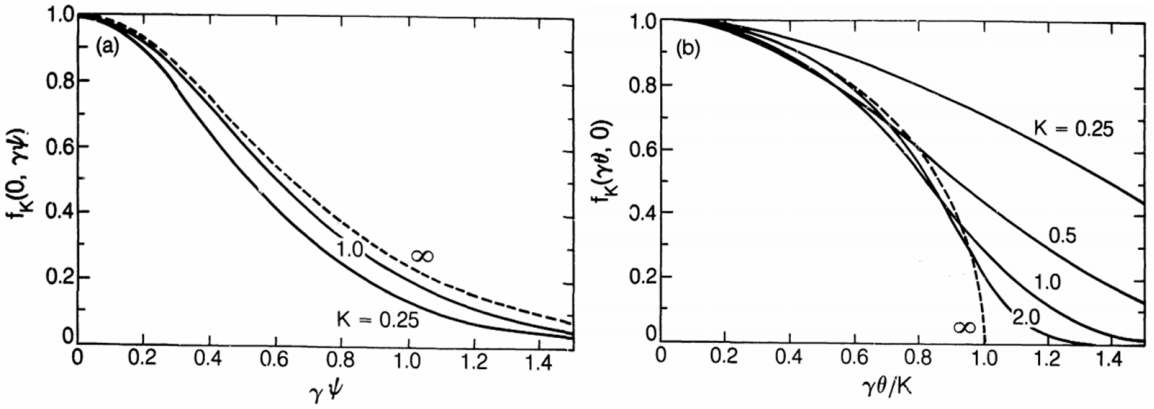

Figure 1.10: The functions $f_k(0, \gamma\phi)$ and $f_k(\gamma\theta, 0)$ are plotted for values of K ranging between 0.25 and ∞. (Reprint from [21]).

1.3 Electron beam dynamics with radiation

In this section, we give an overview of the basic theory that describes the motion of electrons in a storage ring. The main parameters for the electron beam that are relevant to synchrotron radiation will also be introduced.

1.3.1 Single particle beam dynamics

In a circular ring, the motion of a particle is usually studied from a reference trajectory with small deviations; Fig. 1.11 shows the conventional coordinates system to define a reference trajectory. The radius ρ of the arc depends on the bending magnets B,

$$\rho = \frac{p}{eB} \tag{1.34}$$

where p is the momentum of the particle and e is the charge of particle.

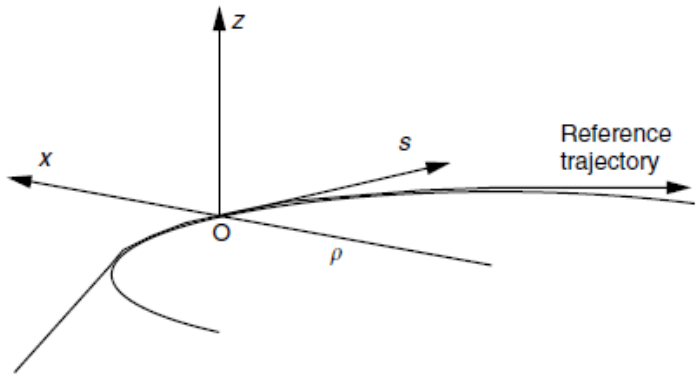

Figure 1.11: Coordinate system of a reference particle trajectory in circular motion. (Reprint from [7]).

In particle dynamics, phase space is used to describe the position and the transverse momentum of the particle. In accelerator physics, these are replaced by the set of coordinates in the system shown in Fig. 1.11 and a point in the 4-dimensional phase space can be defined as:

$$(x, x' = \frac{dx}{ds}, z, z' = \frac{dz}{ds}) \tag{1.35}$$

where the above coordinates represent deviations from the reference trajectory of the electrons.

To simplify the description of the motion of a particle, the deviation of the trajectory from reference is assumed to be small, which is the paraxial approximation,

and the machine is planar horizontal with a mid-plane symmetry. The condition to define such a machine is by using an anti-symmetric magnetic field [7]:

$$\begin{aligned} B_x(x,z,s) &= -B_x(x,-z,s) \\ B_z(x,z,s) &= B_z(x,-z,s) \\ B_s(x,z,s) &= -B_s(x,-z,s) \end{aligned} \tag{1.36}$$

Here we introduce the quantities h, k, m with respect to the normalisation of the momentum:

$$\begin{aligned} h &= \frac{B_0}{p_0/e} \\ k &= \frac{\partial B_z/\partial x}{p_0/e} \\ m &= \frac{\partial^2 B_z/\partial x^2}{2p_0/e} \end{aligned} \tag{1.37}$$

p_0 is the nominal momentum, e is the charge of an electron, B_0 is the uniform magnetic field, h is the curvature of the reference trajectory, k is the normalised field gradient and m is the normalised field second derivative. Typically the storage ring in a synchrotron facility consists of several identical sequences of magnetic elements, which are called superperiods. The set of sequences of the magnetic elements is the magnetic lattice. It is a combination of dipoles, quadrupoles and sextupoles which has a direct impact on the characteristics of the electron beam and on the light that is produced.

Eq. 1.38 presents the elements in a lattice described by the quantities introduced. Dipoles are used to bend the beam. Quadrupoles are used to focus or defocus the electron beam. Sextupoles are used for higher order corrections. Drift means there is no magnet.

$$
\begin{aligned}
&h = \text{constant}, k = 0, m = 0, \text{Dipole} \\
&h = 0, k = \text{constant}, m = 0, \text{Quadrupole} \\
&h = 0, k = 0, m = \text{constant}, \text{Sextupole} \\
&h = 0, k = 0, m = 0, \text{Drift}
\end{aligned} \tag{1.38}
$$

Then the magnetic field can be expanded with Taylor series up to second order in x and z:

$$
\begin{aligned}
\frac{B_x}{p_0/e} &= kz + 2mxz + \cdots \\
\frac{B_z}{p_0/e} &= h + kx + mx^2 - \frac{1}{2}(h'' + hk + 2m)z^2 + \cdots \\
\frac{B_s}{p_0/e} &= h'z + (k' - hh')xz + \cdots
\end{aligned} \tag{1.39}
$$

Since the deviation of the trajectory was assumed to be small, we can now define the momentum deviation $\delta = (p - p_0)/p_0 \ll 1$; therefore $p_0/p = 1/(1+\delta) \approx 1 - \delta + \delta^2$. Combining the Eq. 1.39 and the momentum deviation to the equation of motion in the local axis system, we can obtain the development of the equation of motion to second order. To simplify the calculation, we assume the magnetic field does not depend on the coordinate so $h' = h'' = 0$ and only keep the first order of x and z. The equation of motion can then be described as

$$
\begin{aligned}
&x'' + K_x^2 x = h\delta, \text{ with } K_x^2 = h^2 + k \\
&z'' + K_z^2 z = 0, \text{ with } K_z^2 = -k
\end{aligned} \tag{1.40}
$$

This is a system of Hill's equations, where the horizontal and vertical motion are independent. Assuming the on-momentum particle ($\delta = 0$), first we take a look at the horizontal plane, where a solution of $x(s)$ can be written in the form,

$$x(s) = a_i\sqrt{\beta(s)}\cos(\mu(s) + \phi_i) \tag{1.41}$$

In Eq. 1.41 $\beta(s)$ is the betatron function, $\mu(s)$ is the betatron phase, a_i and ϕ_i are two integration constants for particle i. Eq. 1.41 describes the particle oscillations with position dependent amplitude and phase, it is also called betatron oscillation. The vertical plane has a similar solution as Eq. 1.41. From Eq. 1.40 and Eq. 1.41, one can derive the betatron phase advance as a function of the longitudinal position s,

$$\mu(s) = \int_0^s \frac{1}{\beta(s)} ds \tag{1.42}$$

Since the betatron function $\beta(s)$ is periodic, we define the betatron tune $\nu_{x,z}$ as the number of betatron oscillations per revolution in the horizontal and vertical planes.

$$\nu_{x,z} = \frac{1}{2\pi}\oint \frac{1}{\beta_{x,z}(s)} ds \tag{1.43}$$

The betatron envelope is a position dependent quantity as well, it is defined as,

$$E_{x,z}(s) = \pm\sqrt{\epsilon_{x,z}\beta_{x,z}(s)} \tag{1.44}$$

where the invariant of motion, $\epsilon_{x,z}$, is the beam emittance corresponding to the area of the ellipse in the particle phase space as shown in Fig. 1.12. For the distribution of electrons, this area is the RMS emittance of the electron beam.

Up to now, we have considered the particle motion with $\delta = 0$ (on-momentum). For the off-momentum particles, when the electron energy changes, the ideal orbit will change correspondingly, the trajectory of a particle is given by a combination of the betatron orbit and dispersion from the reference orbit $x_\eta(s)$,

$$x(s) = x_\beta(s) + x_\eta(s) \tag{1.45}$$

where $x_\beta(s)$ is the betatron motion and $x_\eta(s)$ is the off momentum orbit defined as $x_\eta(s) = \delta\eta(s)$. When $\delta = 1$, we can define the dispersion function as

$$\eta'' + k_x(s)\eta(s) = h \tag{1.46}$$

the solution of dispersion function takes the similar form as Eq. 1.41.

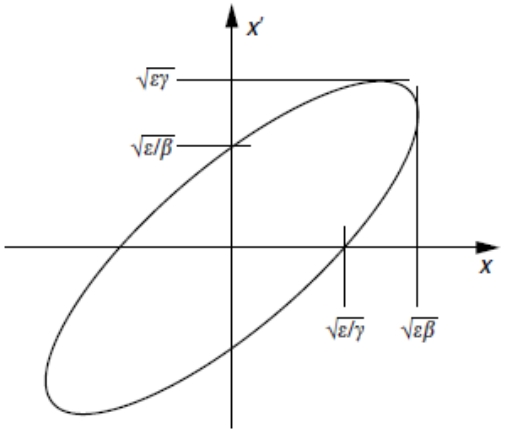

Figure 1.12: Electron beam ellipse in phase space. (Reprint from [7]).

In Fig. 1.12, the α, β, γ are the Twiss parameters describing the orientation of the ellipse in the phase space, ϵ is the area of the ellipse. The acceptance of the beam is the area in phase space where a particle can have a stable motion, it is limited by the dimensions of the vacuum chamber. The electron beam size and divergence can be calculated according to the formulae in Table. 1.1.

	Horizontal	Vertical
Size	$\sqrt{\epsilon_x\beta_x + \eta^2\delta^2}$	$\sqrt{\epsilon_z\beta_z}$
Divergence	$\sqrt{\epsilon_x\gamma_x + \eta'^2\delta^2}$	$\sqrt{\epsilon_z\gamma_z}$

Table 1.1: Formulae to calculate beam size and divergence in the horizontal and vertical planes as a function of Twiss and dispersion parameters.

1.3.2 Radiation damping and quantum excitation

There are many ways to get an off-momentum electron, the most common one is due to the energy loss from synchrotron radiation when the electron goes through a bending magnet. At the same time, RF cavities are used to store energy for accelerating beam. Therefore the synchrotron radiation from an electron circular machine could produce a natural damping of the electron beam oscillation in all the directions in 6D phase space (x, x', y, y', dE, t); this is radiation damping.

The equation of damping rate can be expressed as [13]:

$$a_s = \frac{1}{2T_0}\frac{dW}{dE} \tag{1.47}$$

where T_0 is the orbit period, W is the energy loss per turn for one electron, E is the energy deviation. In order to calculate the ration $\frac{dW}{dE}$, we should estimate the energy loss along a dispersion trajectory. Fig. 1.13 shows a curved element of the reference orbit in the horizontal plane for a particle with the nominal energy E_0, the radius of curvature is ρ. Another trajectory is the particle with the transverse displacement x.

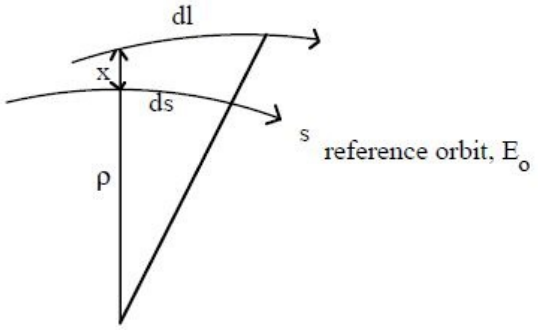

Figure 1.13: Elements of the reference orbit and a displaced trajectory. (Reprint from [22]).

The relation between the path length is [22],

$$\frac{dl}{ds} = 1 + \frac{x(s)}{\rho} \tag{1.48}$$

The closed orbit for an off-energy particle is defined by:

$$x(s) = D(s)\frac{\Delta E}{E_0} \tag{1.49}$$

where D(s) is the dispersion function. Therefore,

$$\frac{dl}{ds} = 1 + \frac{D}{\rho}\frac{\Delta E}{E_0} \tag{1.50}$$

Hence the energy loss per turn can be written as,

$$W = \frac{1}{c}\oint P_s(1 + \frac{D}{\rho}\frac{\Delta E}{E_0})ds \tag{1.51}$$

The energy deviation ΔE performs periodic vibrations about the reference energy and the influence of the energy deviation will vanish after averaging over a long time [13]. Therefore, differentiating gives

$$\frac{dW}{dE} = \frac{1}{c}\oint \left[\frac{dP_s}{dE} + \frac{D}{\rho}\frac{P_s}{E}\right] ds \tag{1.52}$$

Using the radiated power of the synchrotron radiation derived in section 1.2.1 and considering the field variation for quadrupoles with the non vanishing dispersion, Eq. 1.52 can be rewritten as,

$$\frac{dW}{dE} = \frac{2}{cE}\oint \frac{P_s}{ds} + \frac{1}{cE}\oint DP_s(\frac{2}{B}\frac{dB}{ds} + \frac{1}{\rho})ds \tag{1.53}$$

Therefore, the longitudinal damping rate in Eq. 1.47 is

$$a_s = \frac{W_0}{2T_0E}\left[2 + \frac{1}{cW_0}\oint DP_s(\frac{2}{B}\frac{dB}{ds} + \frac{1}{\rho})ds\right] \tag{1.54}$$

or

$$a_s = \frac{W_0}{2T_0E}(2 + \eta(s)) \tag{1.55}$$

where

$$\eta(s) = \frac{1}{cW_0} \oint DP_s(\frac{2}{B}\frac{dB}{ds} + \frac{1}{\rho})ds \tag{1.56}$$

Then we consider the damping of the betatron oscillations, starting with the transverse particle oscillations damping.

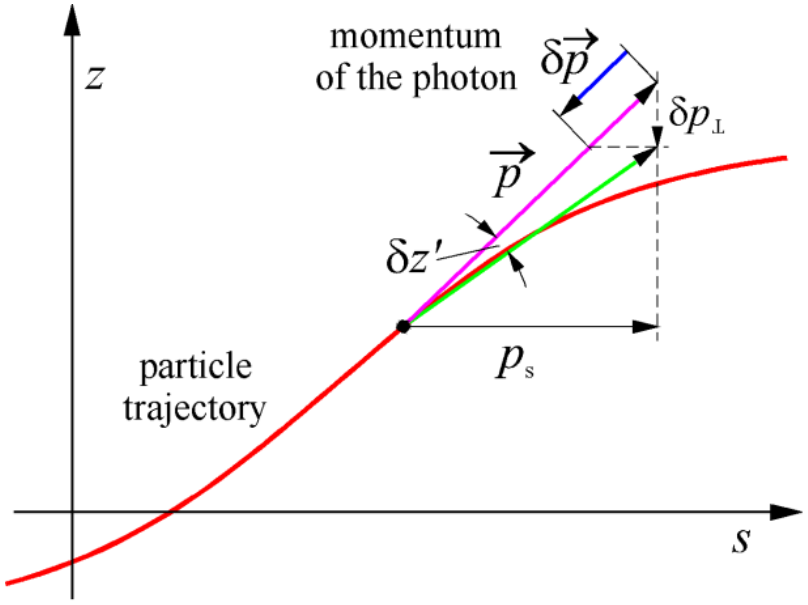

Figure 1.14: Transverse particle damping. The pink vector is the initial electron momentum $\vec{p}$, the blue vector is the momentum loss $\delta\vec{p}$ due to a photon emitted. The green vector is the momentum after emission and energy restoration by the RF cavity. The longitudinal component of momentum is p_s, $\delta p_\perp$ is the reduction of transverse momentum component. $\delta z'$ is the trajectory angle change.

The amplitude A of the transverse particle can be described by the trajectory parameters z and z' [13]:

$$A^2 = z^2 + (\beta(s)z')^2 \tag{1.57}$$

Assume that electrons with momentum $\vec{p}$ may randomly emit a photon with momentum $\delta\vec{p}$. The electron momentum is then $\vec{p} - \delta\vec{p}$. Since the acceleration in RF

cavities can compensate for losses, it will restore momentum in the longitudinal direction. The longitudinal component p_s of the electron momentum remains the same, but the transverse component is reduced as shown in Fig. 1.14. Accordingly the angle z' is reduced by

$$\delta z' = -\frac{\delta p_\perp}{|\vec{p}|} \tag{1.58}$$

With the relation $E = \mathrm{c}|\vec{p}|$,the energy variation follows,

$$\delta z' = -\frac{\delta E}{E} z' \tag{1.59}$$

Since p_s does not change, from Eq. 1.57 we get the variation of the amplitude

$$\delta(A^2) = \delta(z^2) + \delta(z'^2\beta^2(s)) = \beta^2(s)\delta z'^2 \tag{1.60}$$

and we find

$$A\delta A = \beta^2(s) z' \delta z' = -\beta^2(s) z'^2 \frac{\delta E}{E} \tag{1.61}$$

then by taking the average over $<z'^2>$, we find the relation in Eq. 1.61

$$A < \delta A >= -\frac{A^2}{2\beta^2(s)} \beta^2(s) \frac{\delta E}{E} = -\frac{A^2}{2} \frac{\delta E}{E} \tag{1.62}$$

After a full revolution, the energy loss δE has accumulated to the total loss W_0. The average amplitude variation per revolution can be expressed as the sum of all the average amplitudes $\Delta A = \Sigma < \delta A >$. From Eq. 1.62 we then get

$$\frac{\Delta A}{A} = -\frac{W_0}{2E} \tag{1.63}$$

Therefore due to the damping of betatron oscillation, the amplitude decreases. The damping constant can be evaluated according to

$$\frac{dA}{A} = -a_z dt \tag{1.64}$$

If the revolution time $\Delta t = T_0$, we find the expression for the vertical damping constant J_z is

$$a_z = \frac{-\Delta A}{A\Delta t} = \frac{W_0}{2ET_0} = J_z \frac{W_0}{2ET_0} \tag{1.65}$$

In the horizontal plane, the same process occurs, an additional effect due the finite dispersion has to be considered (which is usually zero in the vertical plane) [22]. The change in energy implies a change in the off-energy orbit as described in Eq. 1.49, hence the change in the betatron amplitude is:

$$\delta x = -D\frac{\delta E}{E_0} \tag{1.66}$$

Similarly, the change in angle is:

$$\delta x' = -D'\frac{\delta E}{E_0} \tag{1.67}$$

Therefore, the change in amplitude A is:

$$A\delta A = -(Dx + \beta^2 D'x')\frac{\delta E}{E_0} \tag{1.68}$$

By averaging over the betatron phase over one turn, combine the express for the energy loss as a function of x, we have

$$\frac{\Delta A}{A} = \frac{-W_0}{2E_0}(1 - \eta(s)) \tag{1.69}$$

using the earlier definition of $\eta(s)$ in Eq. 1.56.

Hence the damping rate in the horizontal plane is:

$$a_x = \frac{-\Delta A}{A\Delta t} = \frac{W_0}{2ET_0}(1-\eta(s)) = J_x\frac{W_0}{2ET_0} \tag{1.70}$$

Now, we can directly derive the Robinson criteria [23],

$$J_x + J_z + J_s = 4 \tag{1.71}$$

so the total damping is constant, the damping in a particular plane will affect the damping of other planes.

The energy loss per turn is relatively low compared with the electron beam energy, however after the photon is emitted in quanta of discretized energy, an oscillation of the electron around the orbit occurs. This is the effect of quantum excitation, which counteracts the radiation damping [4], thereby preventing the oscillation amplitude from reaching a zero value.

These two opposite effects will eventually reach an equilibrium, producing a well defined equilibrium emittance characterizing the dynamics of the system.

In phase space, an electron oscillating after the emission of a photon has therefore a finite emittance. It can be calculated using the ellipse relation in [13],

$$\begin{aligned}\epsilon &= \gamma\delta x^2 + 2\alpha\delta x x' + \beta\delta x'^2 \\ &= (\frac{dp}{p})^2(\gamma\eta^2 + 2\alpha\eta\eta' + \beta\eta'^2) \\ &= (\frac{dp}{p})^2\mathscr{H}(s)\end{aligned} \tag{1.72}$$

Then the equilibrium emittance can be obtained [13]

$$\epsilon_x = \frac{55}{32\sqrt{3}}\frac{\hbar c}{mc^2}\gamma^2\frac{<\frac{1}{\rho^3}\mathscr{H}(s)>}{J_x<\frac{1}{\rho^2}>} \tag{1.73}$$

The horizontal damping is represented by J_x. Therefore for a fixed beam energy, the equilibrium emittance depends mainly on the bending radius (ρ) and the dispersion invariant ($\mathscr{H}$).

1.4 Diamond Light Source and its upgrade

The Diamond Light Source is a third generation electron synchrotron machine with a circumference of 561.57m and an energy of 3 GeV, operating at a typical current of 300 mA, with a horizontal emittance of 2.7 nm.rad and a vertical emittance of 8pm.rad. It drives and supports science at UK universities and research institutes [24].

After 13 years of operations, today Diamond can offer 33 photon beamlines to contribute to the fields of science from physics, chemistry and biology to medicine, engineering. A suite of complementary facilities was built namely the Electron Bio-Imaging Centre (eBIC), the Electron Physical Science Imaging Centre (ePSIC), the MPL (Membrane Protein Lab), the XChem Fragment Screening service and the XFEL Hub, which develops technology for sample delivery and data analysis for Free Electron Lasers for life sciences [25].

Beamlines can be grouped into families, each dedicated to specific studies. The main beamline families encountered at Diamond are [24]:

- Spectroscopy (I08, I14, I18, I20, I21)

- Imaging (I06, I08, I12, I13, I14, I18, B22, B24)

- Coherence (I13)

- Diffraction (I07 I08, I09, I11, I12, I14, I15, I18, I19)

- Others (Tomography, Resonant Inelastic X-ray Scattering, Macromolecular Crystallography...)

Fig. 1.15 illustrates the schematic of beamlines and integrated facilities in Dia-

mond.

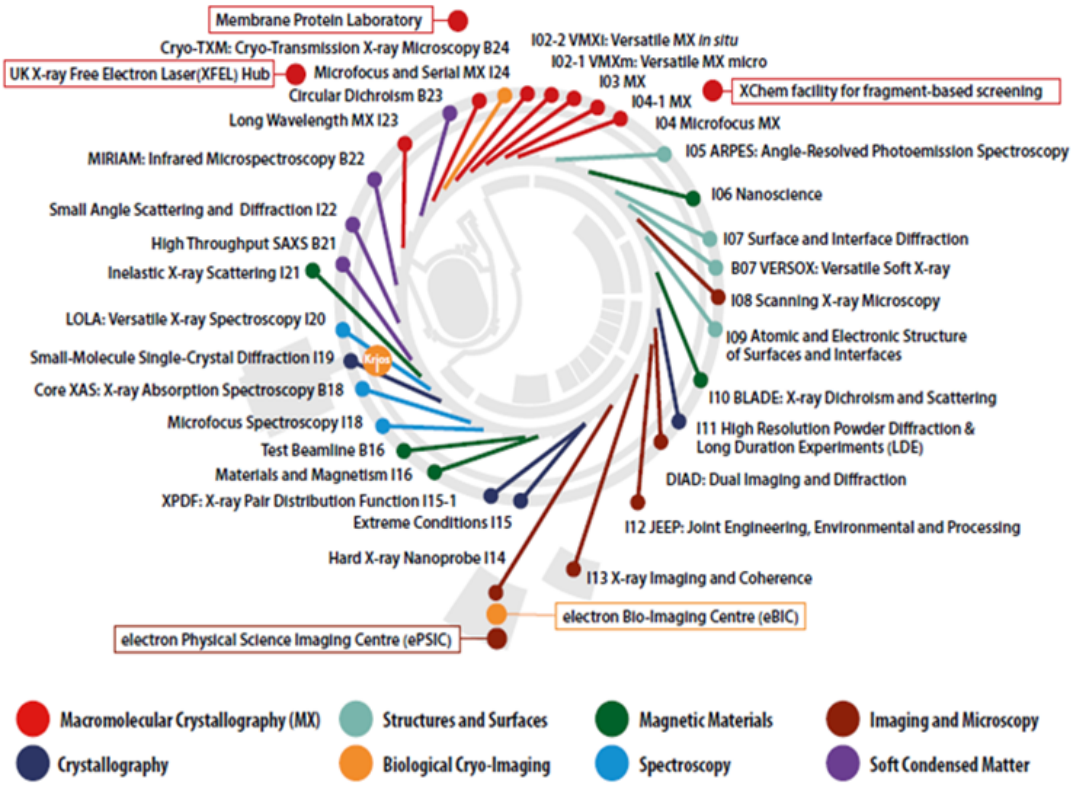

Figure 1.15: Instruments available within science groups and integrated facilities at Diamond. (Reprint from [25]).

For each beamline or family, some Key Performance Parameters (KPP) can be defined as targets to be reached. This project refers to the studies related to the Diamond machine and some of these beamlines.

The Diamond lattice was initially built based on 24 Double Bend Achromat (DBA) cells. In 2009 and 2011, two vertical mini-beta sections were introduced in straights 9 and 13. In 2016, a Double Double Bend Achromat cell was inserted in cell 2, which created an extra mid-straight for a new undulator [26].

High brightness is the goal for synchrotron machine design. Following the theoretical introduction in Section 1.2, we know the brightness is the photon flux per unit area per spectral bandwidth in phase space. Therefore in order to optimise the brightness we can either try to reduce the emittance, especially in the horizontal

plane, or to increase the photon flux.

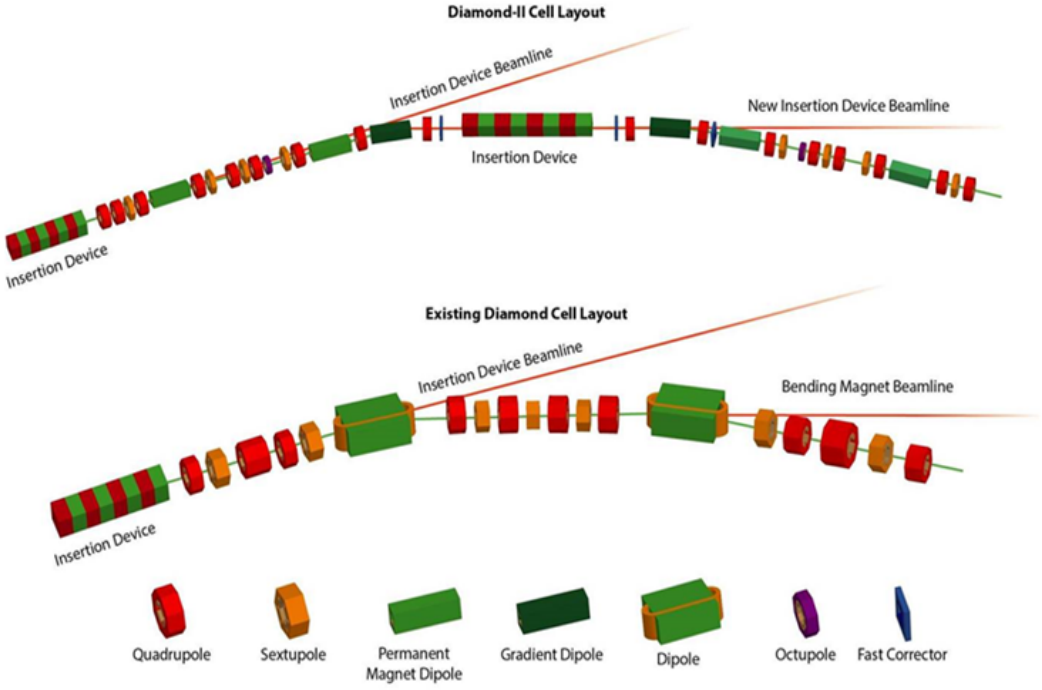

Figure 1.16: Schematic of the current Diamond DBA (Double Bend Achromat, bottom) and the proposed design for a M-HM6BA (Modified Hybrid-Multi-Bend-Achromat) for Diamond-II (top). The new insertion device locates at the new mid-straight section. (Reprint from [27]).

The Diamond-II lattice design is based on so-called Modified Hybrid-Multi-Bend-Achromat (M-HM6BA) [27]. This lattice introduces a mid-straight section per cell for a total of 24 new straights potentially capable of hosting insertion devices. A comparison of the existing Diamond and Diamond-II cell layout is shown in Fig. 1.16. The optics functions are shown in Fig. 1.17, where the reduction of the beta functions and dispersion is clearly visible.

Since the M-HMBA lattice provides a reduction in horizontal emittance by a factor of 20 and the electron beam energy for Diamond-II is 3.5 GeV, the photon beam brightness will be dramatically increased. The overall gain in brightness with respect to that of the current Diamond lattice over the entire spectral range is shown in Fig. 1.18. Clearly the lattice for 3.5 GeV electron energy and 160 pm.rad emittance

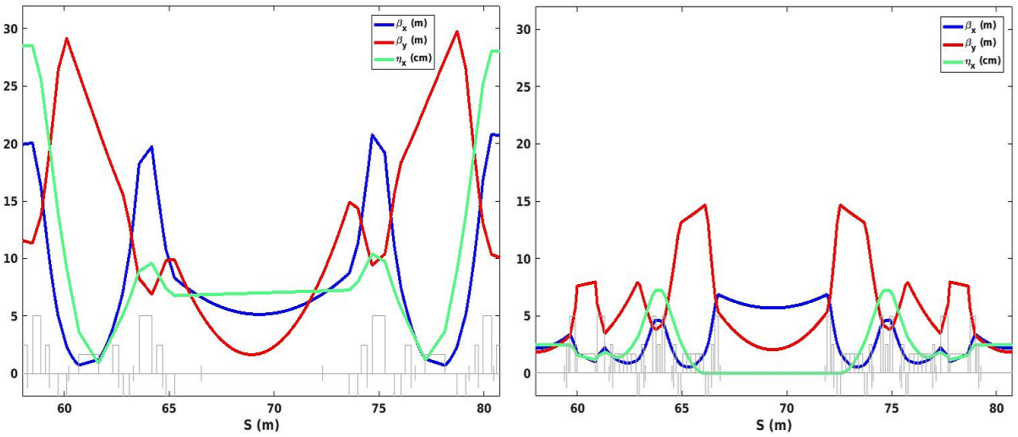

Figure 1.17: Optics functions at the third straight section in current Diamond (left) and Diamond-II (right).

can maximize the gain in brightness in the medium and high energies X-ray regime. A summary of the Diamond and Diamond-II main machine parameters and straight sections lengths is listed in Table. 1.2.

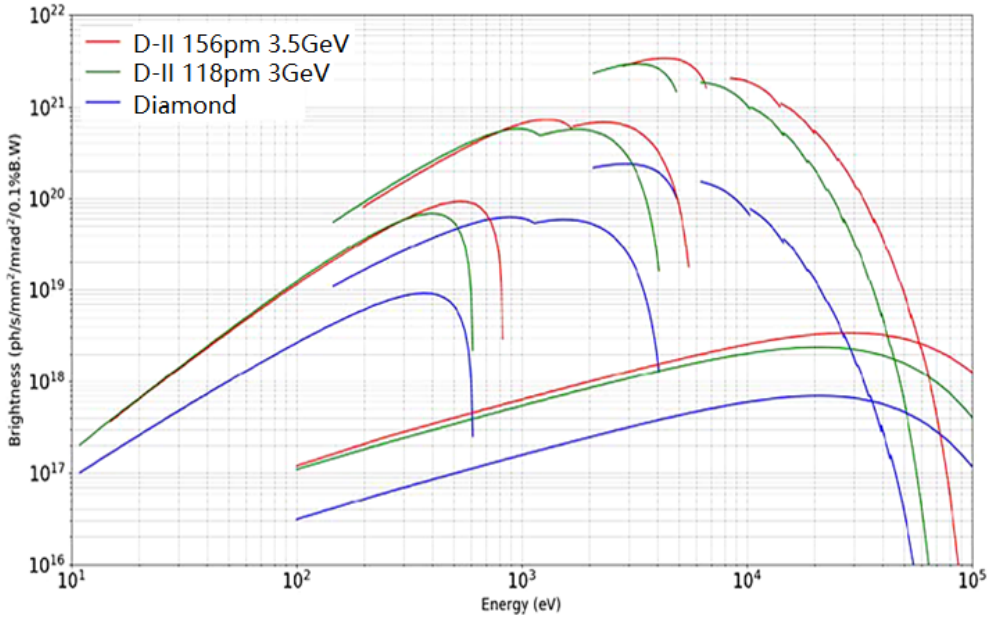

Figure 1.18: Brightness for a set of selected sources at Diamond (blue curves), Diamond-II at 3 GeV (green curves) and Diamond-II at 3.5 GeV (red curves). In the UV regime, soft X-ray regime and hard X-ray, the brightness curves are shown respectively for the I05, I21, the future CPMU 15.6 mm period, and for the superconducting wiggler on I12 [27]. (Reprint from [27]).

	E(GeV)	current(mA)	ϵ_x(pm)	Harmonic number	Energy spread(%)	LSS (m)	SSS (m)	MSS (m)
Diamond	3.0	300	2700	936	0.096	11.3	8.3	3.4
Diamond-II	3.5	300	160	934	0.078	7.5	5.2	2.9

Table 1.2: Diamond and Diamond-II main machine parameters and the lengths change of the respective straight sections. LSS means long straight sections, SSS means standard straight sections, MSS means mid-straight sections.

1.5 Beamline optics

Experiments based on synchrotron light always need a certain number of photons into a phase volume of some particular characteristics such as high flux, brightness and high coherence. Therefore, an optical path is needed to bring the light from the radiation source to the user. Normally the high beam divergence may cause high optical aberrations, requiring large optical device sizes, high costs and low optical qualities. In order to transfer the high quality radiation efficiently, beamlines are designed to transform the photon beam along the optical path in a controlled way: it de-magnifies, monochromatizes and refocuses the source onto a sample.

In a beamline, the synchrotron radiation will be steered, focused and monochromatized by the beamline optics constituted by mirrors, lenses and crystals. In this section, we will give a brief introduction of the optical elements commonly used in synchrotron radiation beamlines.

1.5.1 Focusing mirrors

X-ray mirrors can have different geometrical shapes; their typical optical surface can be a plane, a sphere, a paraboloid, an ellipsoid or a toroid. The coordinate system for the optical path of the focusing mirrors is shown in Fig. 1.19. AO $= r$ is the object distance, BO $= r'$ is the image distance, θ is the angle of incidence. The meridional or tangential plane contains the central incident ray and the normal to the surface and the sagittal plane is the plane perpendicular to the tangential plane and containing

the normal to the surface [28].

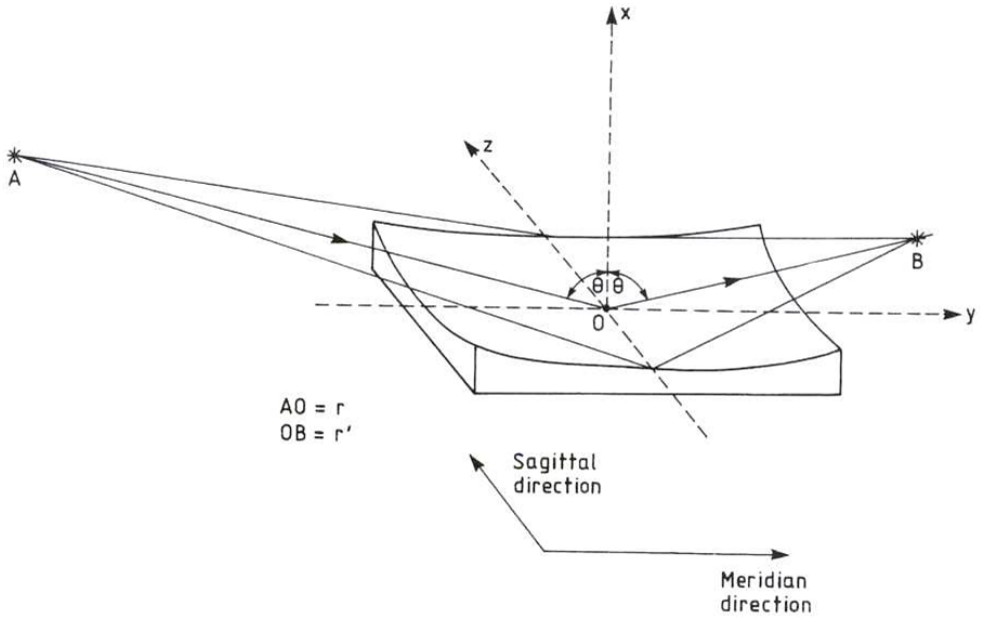

Figure 1.19: The coordinate system for the optical path of the focusing mirrors. (Reprint from [29]).

Fig. 1.20 shows the coordinate system for the optical path of paraboloid mirrors. Incident rays travelling parallel to the symmetry axis OX are focused to a point A. For a parabola the line equation is,

$$y^2 = 4ax \tag{1.74}$$

where $a = f\cos^2\theta$. The location of the pole P of the mirror is given by

$$\begin{aligned} X_0 &= a\tan^2\theta \\ Y_0 &= 2a\tan\theta \end{aligned} \tag{1.75}$$

The equation for a paraboloid is,

$$x^2\sin^2\theta + y^2\cos^2\theta + z^2 - 2xy\sin\theta\cos\theta - 4ax\sec\theta = 0 \tag{1.76}$$

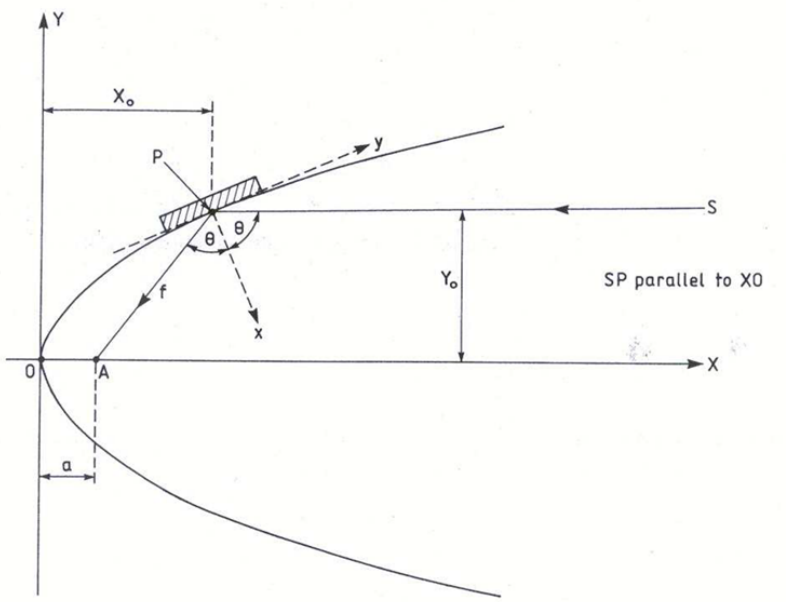

Figure 1.20: The coordinate system for the optical path of paraboloid mirrors. (Reprint from [30]).

An elliptical mirror is generated by simply extending the plane ellipse along an axis perpendicular to the plane of the ellipse [31]. The ellipse can focus rays from one focal point F to another focal point F_2 as shown in Fig. 1.21.

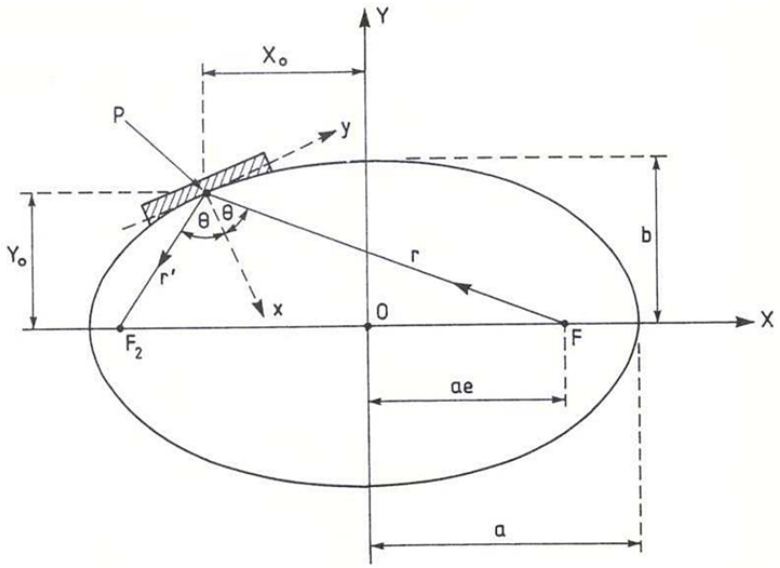

Figure 1.21: The coordinate system for the optical path of ellipsoid. (Reprint from [30]).

The ellipse function is,

$$\frac{x^2}{a^2} + \frac{y^2}{b^2} = 1 \tag{1.77}$$

where $a = \frac{r+r'}{2}$, $b = a\sqrt{1-e^2}$, $e = \frac{1}{2a}\sqrt{r^2 + r'^2 + 2rr'\cos(2\theta)}$. The location of pole of the mirror is,

$$\begin{aligned} X_0 &= a(1 - \frac{y^2}{b^2})^{1/2} \\ Y_0 &= \frac{rr'\sin(2\theta)}{2ae} \end{aligned} \tag{1.78}$$

And the equation for an ellipsoid is,

$$x^2(\frac{\sin^2\theta}{b^2} + \frac{1}{a^2}) + y^2(\frac{\cos^2\theta}{b^2} + \frac{z^2}{b^2}) - x(\frac{4f\cos\theta}{b^2}) - xy\left[\frac{2\sin\theta\sqrt{e^2 - \sin^2\theta}}{b^2}\right] = 0 \tag{1.79}$$

where $f = (\frac{1}{r} + \frac{1}{r'})^{-1}$. With an ellipsoidal mirror, the image of an extended source is an arc. This element is always used to focus the beam in one plane. However, an ellipsoid has its aberrations such as the photon beam in different directions failed to focus at the same observation point or flat object normal to the optical axis cannot be brought properly into focus on a flat image plane.

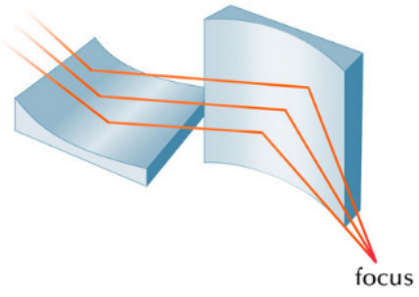

Figure 1.22: A schematic of the Kirkpatrick - Baez system. The two mirrors focus the vertical and horizontal planes correspondingly. (Reprint from [32]).

In 1948, Kirkpatrick and Baez presented a two mirror system, called the KB system [33]. Fig. 1.22 shows a schematic of the KB system: two mirrors are set independently to focus the object in the two orthogonal planes. With this setup, the aberrations of the elliptical mirror are avoided [31].

Another optical element that can focus the two planes is the toroid. In general, a toroid produces two non-coincident focal points: one in the tangential focal plane and one in the sagittal focal plane. It is commonly used when a beam must be focused and folded, hence both functions could be combined in one element. Fig. 1.23 shows the optical path system for a toroid.

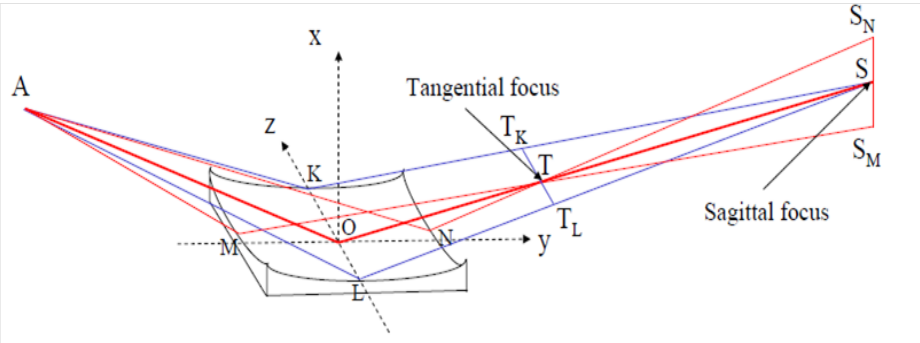

Figure 1.23: The coordinate system for the optical path of toroid. MN shows the tangential focus, KL shows the sagittal focus. (Reprint from [29]).

The focus of the two planes satisfies,

$$\begin{aligned}(\frac{1}{r}+\frac{1}{r'_t})\frac{\cos\theta}{2} &= \frac{1}{R}\\ (\frac{1}{r}+\frac{1}{r'_s})\frac{2}{\cos\theta} &= \frac{1}{\rho}\end{aligned} \tag{1.80}$$

where r is the source distance, r'_t and r'_s are the image distances for tangential and sagittal plane, respectively. R and ρ are the radius of tangential and sagittal arc respectively. For $\rho = R$, it becomes a spherical mirror.

1.5.2 Gratings and crystals

Gratings are commonly used in generating angular dispersion in a polychromatic incident X-ray beams, which can create effective monochromators. A grating system is designed with a periodic structure as shown in Fig. 1.24. The diffraction condition for a grating is

$$\sin\alpha + \sin\beta = NK\lambda \tag{1.81}$$

where α and β are the incident and outgoing beam angle respectively; the signs of α and β are opposite if they lie on opposite sides of the grating normal [31]. d is the periodic length of the groove, $N = 1/d$ is the groove density, K is the order of diffraction (±1,±2,...), λ is the incident wavelength.

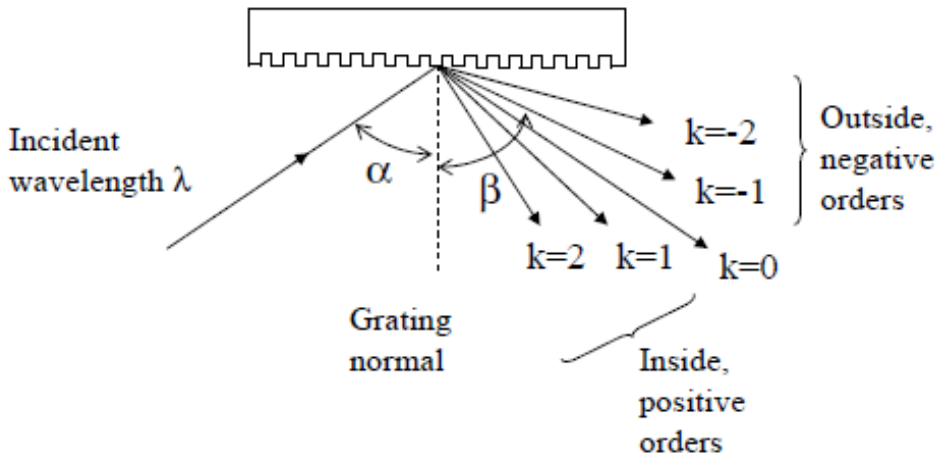

Figure 1.24: The optical path of a diffraction grating. In this diagram β is shown for the first negative (outside) order. (Revised from [31]).

The angular dispersion of the grating is the amount of change of diffraction angle per unit change of the wavelength [34]:

$$\frac{\Delta\beta}{\Delta\lambda} = \frac{NK}{\cos\beta} \tag{1.82}$$

Therefore, high angular dispersion can be achieved either by choosing a grating with a high groove density or by using a high diffraction order. For an instrument the spectral resolution is determined by the separation ($\Delta\lambda$) between two spectral peaks, the grating set characteristics define the limitation of the resolution. The resolving power (R) is used to describe the resolution limitation from gratings,

$$R = \frac{\lambda}{\Delta\lambda} = KnN \tag{1.83}$$

here nN is the total number of grooves on the entire grating surface [34].

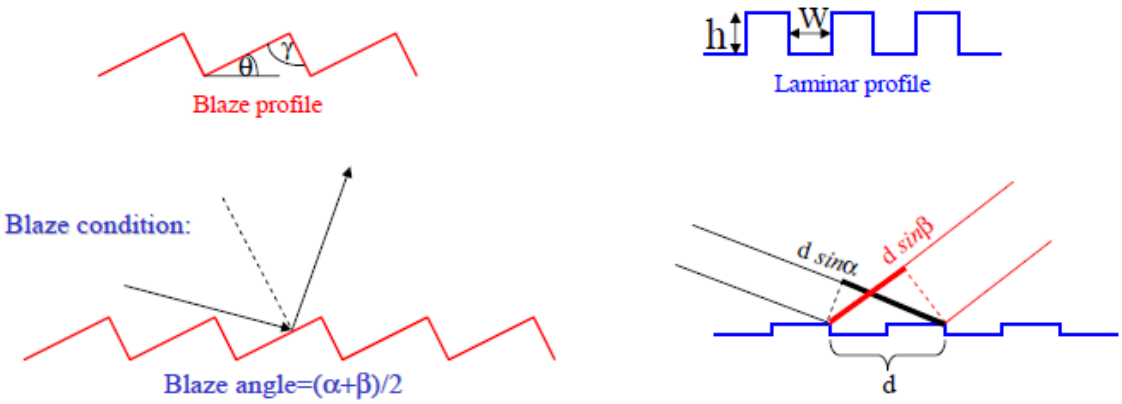

Figure 1.25: Two types of gratings profiles. Blaze gratings (left) and Laminar gratings (right). (Reprint from [29]).

There are two types of grating profiles. One is the Blaze grating shown in Fig. 1.25 (left), the angle θ is selected so that for a given wavelength, the diffraction direction is consistent with the specular reflection direction from each facet. Another is the Laminar gratings which can produce higher spectral purity. The structure is shown in Fig. 1.25 (right); the incident wavelength satisfies $\lambda = d(\sin\alpha + \sin\beta)$.

Monochromatic photon beams of high intensity are always required for imaging. Crystal monochromators are designed for selecting a range of wavelengths in the photon beam. In a crystal, X-ray diffraction will occur when the Bragg condition [35] is met

$$2d\sin\theta = n\lambda \tag{1.84}$$

where d is the spacing between crystal lattice planes, θ is the Bragg angle measured from the diffracting planes, λ is the wavelength of the incident X-rays, n is the order of diffraction. The Bragg condition indicates that the interference of the outcome rays is constructive when the optical path difference is an integer multiple of the incident radiation wavelength as shown in Fig. 1.26.

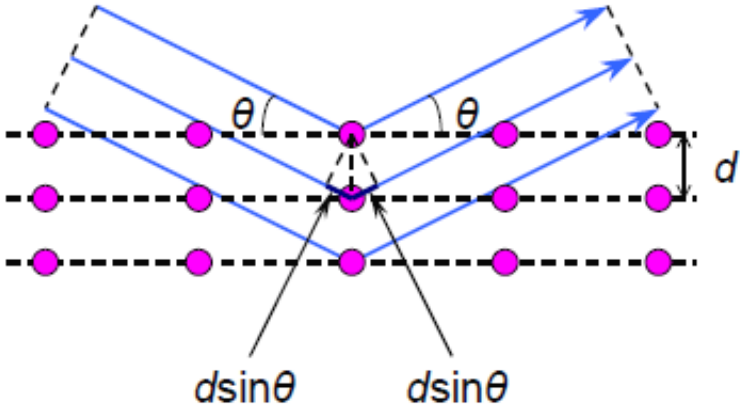

Figure 1.26: The Bragg case of the X-ray diffraction in a crystal. The spacing between crystal lattice planes is d, θ is the Bragg angle. (Revised from [36]).

The energy resolution of a crystal is defined by,

$$\frac{\Delta E}{E} = \frac{\Delta\lambda}{\lambda} = \Delta\theta\cot\theta \tag{1.85}$$

where E is the beam energy at the Bragg angle, λ is the wavelength corresponding to this energy and ΔE and $\Delta\lambda$ are energy and wavelength discrepancy caused by beam angular divergence. Therefore when a collimated beam passes through a crystal, this works as in Fig. 1.27 (left); the grazing angle is always same. While if the beam is with a certain divergence, as shown in Fig. 1.27 (right), the incident angle of rays is between θ_a and θ_b and the outgoing beam will have different wavelengths, which affects the reflectivity of crystal.

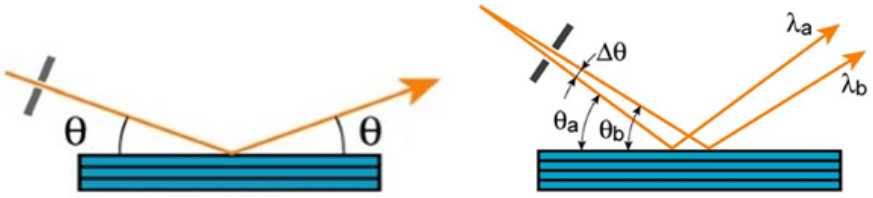

Figure 1.27: The crystal diffraction of a collimated beam(left) and a naturally divergent beam(right). (Revised from [36]).

In classical optics, the reflectivity of a perfect crystal depends on the wavelength of the incident radiation and on the incident angle [37]. The reflectivity R for the Bragg case, for no absorption and a thick crystal, is shown in Fig. 1.28, which satisfies the relation in Eq. 1.86.

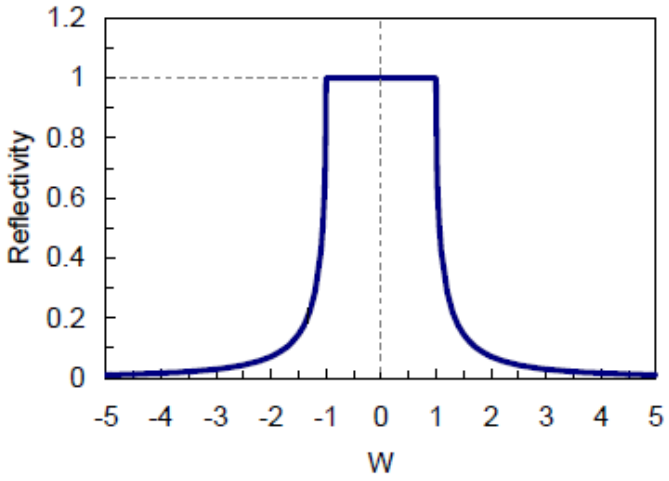

Figure 1.28: The reflectivity as a function of W of a thick crystal with no absorption for the Bragg case.

$$R = (W + \sqrt{W^2 - 1})^2 (W < -1)$$
$$R = 1 (-1 \leq W \leq 1)$$
$$R = (W - \sqrt{W^2 - 1})^2 (W > 1) \quad (1.86)$$

W is a function of the Bragg angle and incident beam angle [36] [38]. Here $\Delta W = 2$

is the Darwin width. The Darwin width is the full width half-maximum (FWHM) of the total reflective profile of the monochromator crystal and is given by [39],

$$\omega_n = 2.12 r_e (\frac{\lambda}{(n+1)})^2 \frac{N F_h}{\pi \sin(2\theta)} \tag{1.87}$$

r_e is the electron radius, N is the atomic density, F_h is the structural factor $F_h = F(sin\lambda/d)/(h^2+l^2+k^2)$, where h, k, l are Miller indices of the reflection plane and n is the order of the harmonic. In a realistic case, the curve has a typical asymmetric shape due to the absorption of the thick crystal and the diffraction will bring a shift to the angle [40].

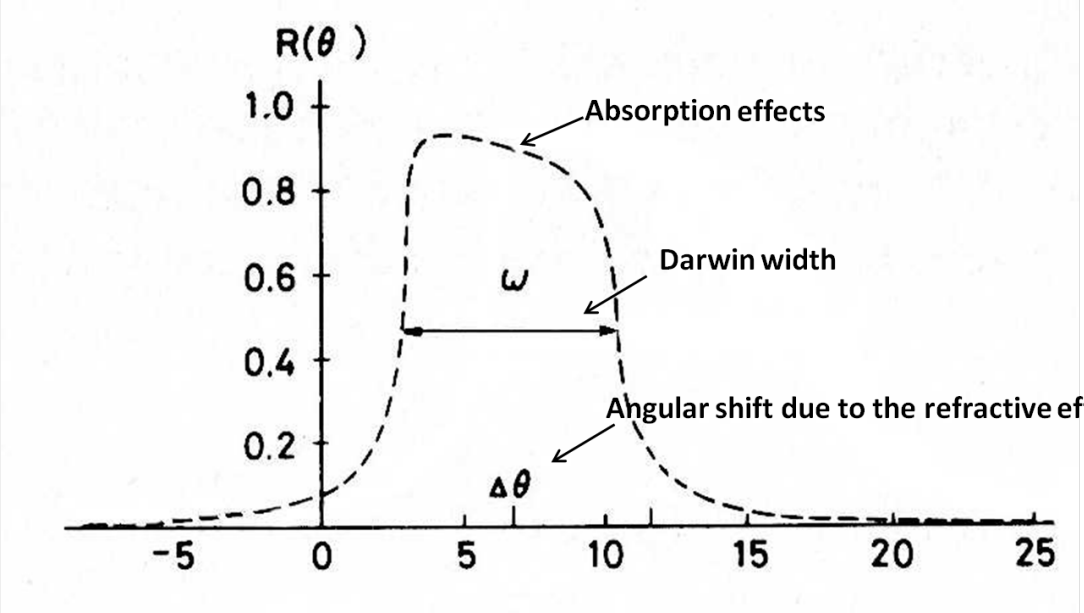

Figure 1.29: A typical reflection curve of a thick crystal. (Revised from [29]).

Fig. 1.29 shows a typical reflection curve of a thick crystal. This curve is also called the Darwin-Prins curve [41]. It is obtained by measuring the crystal reflectivity as a function of the angle difference between the incidence angle and the ideal Bragg value for a perfectly collimated monochromatic beam.

1.5.3 Compound refractive lens and zone plates

For hard X-rays, the refractive index for all materials is close to 1, therefore a CRL is designed by using many concave shape lenses to get a reasonable short focal length for X-ray beamlines [42]. Fig. 1.30 shows the schematic of CRL which results in a line focus of X-rays.

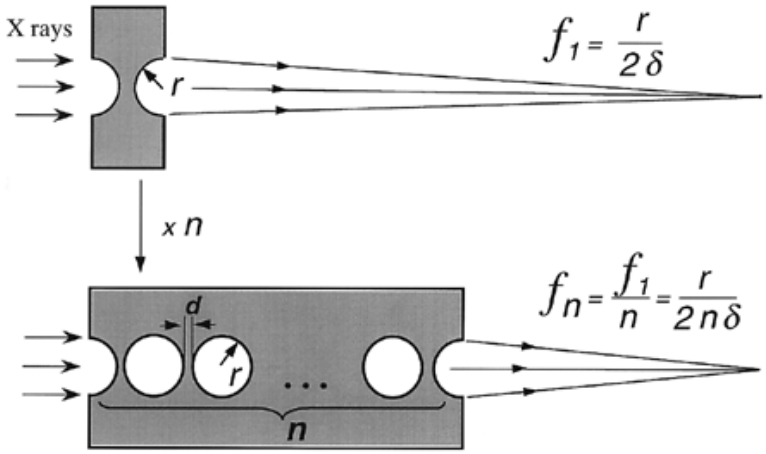

Figure 1.30: Schematic diagram shows the principles of X-ray focusing by a compound refractive lens (CRL). (Reprint from [42]).

A single lens has a focal lens $f_1 = \frac{r}{2\delta}$, where r is the radius of the hole, the index decrement δ is the difference of the refractive index to one. Then for a compound lens with n holes, it has a focal length $f_n = \frac{r}{2n\delta}$ which is n times smaller than the single lens focal length. This puts the focal length of a CRL for hard X-rays into an acceptable range.

Nowadays, CRL lenses are available as paraboloids of revolution (2D lenses) or as parabolic cylinders (1D lenses), focusing either in both or only in one plane, and within a wide range of focal lengths. The geometry of 2D and 1D lenses are shown in Fig.1.31 [43].

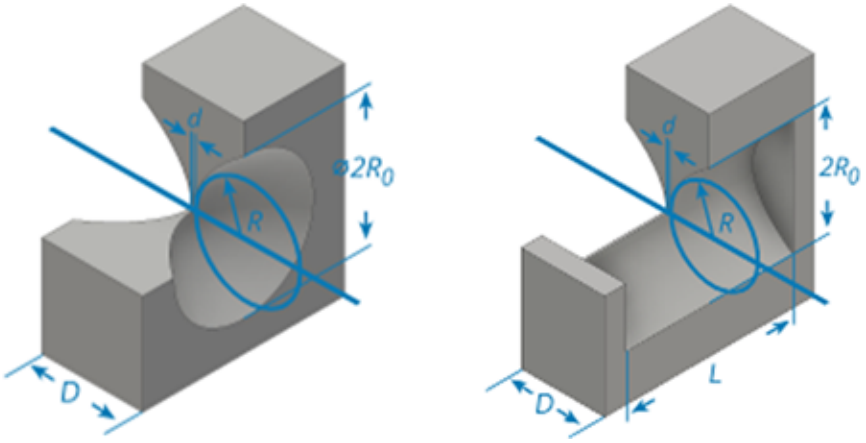

Figure 1.31: Geometry of refractive x-ray lenses: 2D lens (left) and 1D lens (right). D is lens thickness, L is lens length, d is apex thickness, R is radius of curvature at the apex of the paraboloid, $2R_0$ is geometric aperture. (Reprint from [43]).

For lower energy X-rays, refractive lenses become inefficient because of the absorption effects and the low spatial resolution. Zone plates are developed based upon the diffractive focusing processes which offer the spatial resolutions lower than 40nm [44]. The Fresnel zone plate consists of alternating opaque and transparent rings as shown in Fig. 1.32. The destructive amplitude is absorbed in the band plate. This enlarges the intensity at the focal spot.

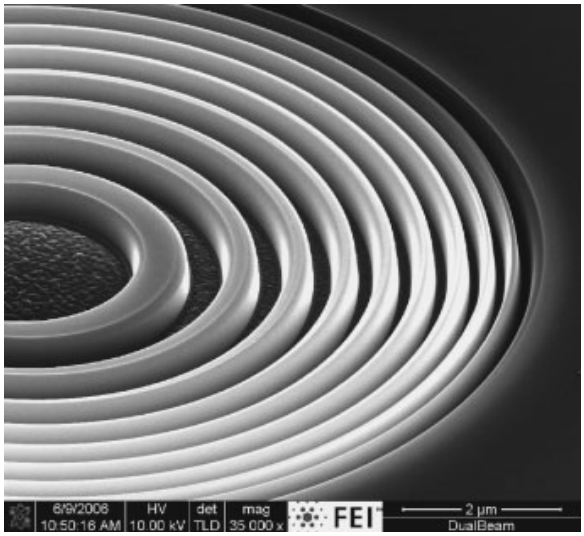

Figure 1.32: A schematic of X-ray Fresnel zone plate. (Reprint from [45])

In many respects, the zone plates behave like a circular lens to focus beam. The

main difference is a zone plate has different diffraction orders and therefore several focal spots. Other kinds of zone plates are the phase zone plate and the Bragg Fresnel lens. For the phase zone plate, the rays with a path difference of $\lambda/2$ are not absorbed but shifted in phase by $\pi/2$, which gives a theoretical efficiency four times higher than the Fresnel zone plate [46]. The Bragg-Fresnel lens works similarly to the phase zone plate. The reflected radiation is monochomatized by the Bragg condition. Therefore the Bragg-Fresnel lenses can be used in a white beam without a monochromator [47].

1.6 Motivations for this project

From the previous introduction, synchrotron light sources have been extremely successful tools enabling scientific research to respond to the global challenges in medicine, food and environment, security, engineering and technology development over the past 50 years. In recent years a new class of machines is being built or already operating (MAX IV [48], ESRF-EBS [49], Sirius [50]) promising a new generation of X-ray beams with revolutionary properties and unprecedented quality, extreme brightness and stability. Many more synchrotron sources around the world are at an advanced design stage (APS-U [51], ALS-U [52], SLS-2 [53], Diamond II [27], SOLEIL-U [54]) and are aiming at building the next generation of diffraction limited synchrotron light sources based on ultra-low emittance accelerator lattice designs. Such light sources promise to deliver extremely high brightness radiation, highly coherent, with an exquisite control of the photons phase space. These projects are underpinned by a large R&D effort in many of the technological components to meet the technological challenges associated with the production of such high quality X-rays.

One of the key challenges in the design of such accelerators is in the optimisation of the electron optics, combined with the photon optics of the beamlines to take full advantage from the reduced electron beam emittance, the increased brightness and

coherence of the radiation. In order to understand the trade-offs and to find the best compromise between beamline performance parameters and machine parameters, an integrated approach to the problem of the optimisation of the electron and photon dynamics is demanded. Therefore, a complete simulation from the electrons generating the synchrotron radiation to the final sample plane will be a valuable tool for a general optimisation of the system. To achieve this, the project entails the definition and optimisation of the electron and photon beam optics using state of the art computing codes and advanced numerical techniques.

Such optimisation techniques will be applied to the existing 3 GeV storage ring at the Diamond Light Source and to the Diamond II design.

1.7 Thesis layout

This thesis begins from presenting an overview of the background material and dynamics of synchrotron radiation. Since the work is based on the Diamond Light Source and its upgrade, a brief introduction for the facility has also been provided. Beamline optics play a key role in improving the beamline performance, thus some commonly used optics in beamlines are introduced. The motivation for this research project has been described at the end of the first chapter.

The rest of the thesis is structured as follows. A numerical integrated approach is introduced with the codes environment and some applications in Chapter 2. Chapters 3 and 4 present the optimisation of the undulator and wiggler beamlines in Diamond and Diamond II. Both the wavefront method and ray tracing method are used. The evaluation of the feasibility of some photon sources for Diamond II beamlines is included in Chapter 4. Conclusions and future work are discussed in chapter 5.

Chapter 2

Development of numerical techniques and codes for the integrated approach E2S

As described in the first chapter motivation part, this project aims at investigating and developing novel designs for the electron optics in the storage ring and of the photon optics in the beamline in order to take full profit from the ultra-low emittance of the electron beam and the coherence properties of the X-ray radiation generated by the bending magnets and the insertion devices. To achieve this goal we developed a code, wrapping up the main simulation packages commonly used in the Accelerator Physics and in the Synchrotron Radiation and Optics communities [55]. The genetic optimisation of beamline design is also included in this code which could provide a better configuration for efficient beamline design.

In this chapter, we show the structure and theory of this code. Some typical examples of the computation and a case study based on this code will be presented.

2.1 Code environment

The code we developed is called Electron to Sample (E2S). It is written in Python. The code starts from Elegant [56] which extract the Twiss parameters at the photon source position, linked to the Synchrotron Radiation Workshop (SRW) [57] for the emission and propagation of photons.

The program starts with a call to Elegant, which performs a calculation of the Twiss parameters at a selected source point. These parameters are then translated into beam moments and passed to the photon code SRW. In SRW, first the emission of the synchrotron radiation is calculated, then the photon beam will propagate through a beamline as designed. Fig. 2.1 shows the structure of E2S.

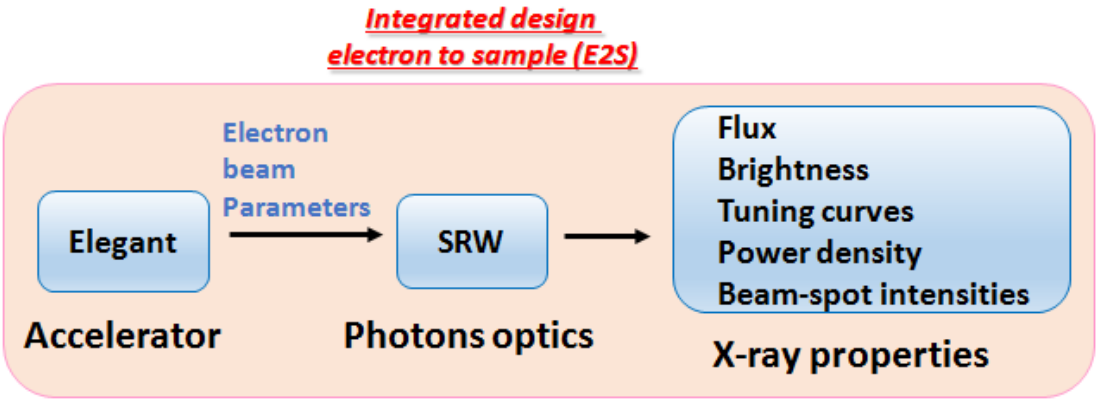

Figure 2.1: A schematic of the E2S code structure.

The information on the source position in the storage ring and the parameters characterizing the ID need to be implemented in an input file where we can also specify the lattice and propagation mode. Beamline information is listed in a Python file where we can define the optics parameters clearly.

The beamline optimiser is developed to optimise the key performance parameters of a beamline. Here the Non-Dominated Sorting Genetic Algorithm II (NGSA II) [58] is linked either to the SRW which propagates photons according to a wavefront

model or to the geometrical ray-tracing code SHADOW [59]. The structure of the optimiser is shown in Fig. 2.2.

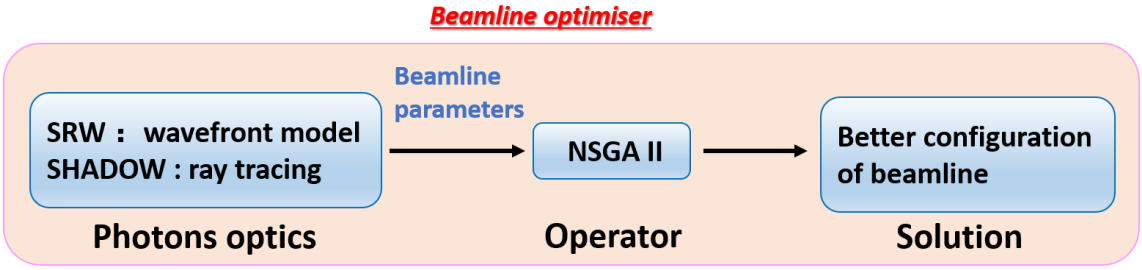

Figure 2.2: A schematic of the optimiser code structure.

2.1.1 Elegant

Elegant (ELEctron Generation ANd Tracking) is an accelerator simulation code which can track the electron beam by using matrices, canonical integration, and numerical integration [56]. In Elegant, standard beamline elements and coherent synchrotron radiation, wakefields, RF elements, kickers, apertures and scattering are supported. In addition to tracking with and without errors, Elegant performs optimisation of tracked properties, as well as computation and optimisation of Twiss parameters, radiation integrals, matrices, and floor coordinates [56]. Elegant is written entirely in the C programming language [60], and uses a variant of the MAD [61] input format to describe accelerators, which may be either transport lines, circular machines, or a combination thereof [56]. The code is fully compliant with the Self Describing Data Sets [62] (SDDS) file protocol, and SDDS Toolkit is used for pre- and post-processing. Hence users can run the code in a flexible and automated fashion by preparing their own scripts.

E2S starts from Elegant. Lattice information has been saved in a lattice file (file.lte), it is a linear sequence of elements that specifies the elements with the description of element type, parameters and the order. Elegant is executed by a namelist

format commands. A command file (file.ele) provides Elegant with setup and action command [63]. Setup commands includes run-setup to specify global parameters and the input/output files. Action commands can compute and output Twiss parameters, and track particle coordinates for beam distributions. In the E2S input file, it is allowed to specify the lattice and also define machine parameters.

After the calculation of Elegant, Twiss parameters combined with other ID information and beamline information will make up a new input file for the next step calculations.

2.1.2 SRW

Synchrotron Radiation Workshop (SRW) is a code which uses rapid numerical algorithms for different radiation sources including bending-magnet radiation (from central parts and edges), and undulator and wiggler radiation. SRW consists of two parts, one is the computation of the near-field SR emitted by an electron beam in a magnetic field of nearly arbitrary configuration, the other is the simulation of the propagation of the near-field SR through optical elements (lenses, focusing mirrors, apertures) and drift spaces [57].

2.1.2.1 Emission of synchrotron radiation

The importance of near-field computation of undulator radiation has been discussed in [64]. In this section, the computation methods of the near-field SR emission in SRW are presented.

The computation for the near-field SR emission by a single electron in frequency domain is based on an approach where retarded potentials are applied [65]. It starts from Fourier transformations of the retarded scalar and vector potentials. The electric field of radiation emitted by a relativistic electron in a Gaussian system is obtained in Eq. 2.1.

$$\vec{E} = iek \int_{-\infty}^{+\infty} [\vec{\beta} - \vec{n}[1 + i(kR)^{-1}]]R^{-1} \exp[ik(c\tau + R)]d\tau \tag{2.1}$$

where k is a wave number, $\vec{\beta} = \vec{\beta}(\tau)$ is the instant relative velocity of electron, $\vec{n} = \vec{n}(\tau)$ is the unit vector directed from the instantaneous electron position to an observation point, $R = R(\tau)$ is the distance from the electron to the observation point, c is the speed of light and e is the electron charge.

The electric field computed in the code is directly derived from Eq. 2.1, after a proper phase expansion that allows avoiding loss of precision in the phase [65]. To ensure fast convergence of the integral, a semi-analytical treatment of its outer parts is performed according to the following asymptotic expansion [66]:

$$\begin{aligned} &\int_{-\infty}^{\infty} F \exp(i\phi)ds = \int_{s_1}^{s_2} F \exp(i\phi)ds + \int_{-\infty}^{s_1} F \exp(i\phi)ds + \int_{s_2}^{\infty} F \exp(i\phi)ds \\ &\int_{-\infty}^{s_1} F \exp(i\phi)ds + \int_{s_2}^{\infty} F \exp(i\phi)ds \approx \left[(\frac{F}{i\phi'} + \frac{F'\phi' - F\phi''}{\phi'^3}) \exp(i\phi) \right]_{s_2}^{s_1} \end{aligned} \tag{2.2}$$

where F is a function of phase space. This allows one to compute numerically only the integral between some values of the longitudinal position s_1 and s_2. These values are chosen in such a way that the interval [s_1,s_2] is as small as possible yet still satisfies the requirement that the second term of the asymptotic expansion is essentially smaller than the first one [67].

For a non-zero frequency, this method is analytically equivalent to the more widely used method which treats separately the acceleration and the velocity fields [68]. From a numerical point of view, this method is more efficient than the computation made by summing up the acceleration and velocity field contributions [57].

At present, the code does not treat the radiation electric and magnetic fields separately. It only takes transverse components of the electric field into account. Such a consideration is valid only if the electron trajectory passes at a distance from the

observation point considerably larger than the wavelength of the observed radiation and it is easily satisfied in most of the high energy storage rings.

After computing the SR electric field in a transverse plane located at some distance from the source, the next step is to propagate the electric field through a set of optical elements.

2.1.2.2 Synchrotron radiation propagation

The SR wavefront propagation is implemented by using a CPU-efficient method of Fourier Optics. The electric field of synchrotron radiation at the aperture can be calculated by means of the Huygens-Fresnel principle [69]. The transverse component of the electric field of diffracted synchrotron radiation $\vec{E}_{\perp 2}$ can be computed from the electric field $\vec{E}_{\perp 1}$.

$$\vec{E}_{\perp 2} = -ik(2\pi)^{-1} \int\int_{\Sigma} \vec{E}_{\perp 1} S^{-1} \exp(ikS) d\Sigma \tag{2.3}$$

where k is a wave number, Σ is a surface within the diffracting aperture, S is a distance from a point on this surface to an observation point. If Σ is a plane normal to the optical axis, then,

$$\begin{aligned} d\Sigma &= dx_1 dz_1 \\ S &= [(x_2 - x_1)^2 + (y_2 - y_1)^2 + (z_2 - z_1)^2]^{1/2} \end{aligned} \tag{2.4}$$

where (x_1, y_1, z_1) and (x_2, y_2, z_2) are the coordinates of a point on the Σ plane and on the observation plane respectively. Eq. 2.3 is a convolution type integral, which can be quickly computed by applying the convolution theorem and the 2D fast Fourier transforms [57]. This gives a CPU-efficient method of propagation of all wavefront through a drift of any length at once.

The propagation of the transverse electric field through a perfect thin lens is described well by a multiplication of the field by a function of transverse coordinates [19]. For more complicated elements, one can apply physical considerations or analytical methods to derive the proper transformation of the electric field [57].

The main advantage of this wavefront propagation method is speed. A 2D wavefront can be propagated from several seconds to a minute. This allows one to perform computations with several optical elements at once.

2.1.2.3 Non-zero Emittance Electron Beam treatments

In the previous paragraph, we considered the SR as emitted by a single electron. Now we consider the effects of a non-zero emittance beam.

The SR intensity distribution for radiation from a non-zero emittance electron beam is computed by making a convolution over the horizontal and vertical coordinates of the single electron intensity distribution with a 2D Gaussian. The RMS of this Gaussian is given by the electron beam sizes propagated to the observation plane, using the rules of the second-order moment propagation [57].

Let the ϵ_x and δE be the horizontal emittance and relative energy spread of the electron beam. Then the second order moments of the particle distribution in the beam can be computed at any longitudinal position by using the lattice functions at that position [67],

$$
\begin{aligned}
&< (x - < x >)^2 >= \sigma_x^2 = \epsilon_x \beta_x + \delta E^2 \eta_x^2 \\
&< (x - < x >)(x' - < x' >) >= -\epsilon_x \alpha_x + \delta E^2 \eta_x \eta_x' \\
&< (x' - < x' >)^2 >= \sigma_{x'}^2 = \epsilon_x (1 + \alpha_x^2)/\beta_x + \delta E^2 \eta_x'^2
\end{aligned}
\tag{2.5}
$$

Assume **T** is a 3×3 matrix describing the transformation of the horizontal second order moments from the source point to the observation plane in a beamline. The

RMS of the Gaussian used in the convolution with the single electron intensity $< (x - < x >)^2 >_p$ is obtained from the relation [67]

$$\begin{bmatrix} < (x - < x >)^2 >_p \\ < (x - < x >)(x' - < x' >) >_p \\ < (x' - < x' >)^2 >_p \end{bmatrix} = \mathbf{T} \begin{bmatrix} < (x - < x >)^2 > \\ < (x - < x >)(x' - < x' >) > \\ < (x' - < x' >)^2 > \end{bmatrix} \tag{2.6}$$

The vertical moments are treated similarly, except that the vertical dispersion is neglected.

2.1.3 SHADOW

The ray-tracing technique has been widely used for decades to simulate synchrotron beamlines. The effects limiting the performances of X-ray optical elements such as source emittance, aberrations and the errors in the optical surfaces can be efficiently modelled by ray tracing.

SHADOW [59] is a popular code to simulate the optical systems, especially in the synchrotron radiation domain. It is based on geometrical ray-tracing and also traces field amplitude with a phase difference, which is capable of including the reflectivity and transmittance of optical elements calculated by models of physical optics.

The source in SHADOW is described by collecting rays from a certain spatial area; by rays we define a straight line that starts at a point and travels until it intersects a surface or optical element [70]. The combination of rays constitutes a photon beam. The source is three dimensional, the distribution of the photon beam in the spatial area intuitively defines the characteristic of the source [71]. SHADOW works in the Cartesian coordinate reference frame. The physical model of the source is formed by the probability distribution densities (pdf) that describe the ray distribution in space and in angle. Thus the source in SHADOW is a collection of a number of rays described by their starting position, direction, energy and phase [72]. The boundary

of the source specifies the spatial area in which rays are generated and may have different shapes.

After successfully building the source, the next step is propagating the rays by setting up the optical system (OS) and executing the ray-tracing of the source through the system [72]. The optical system consists of a series of optical elements (OE); elements are specified independently and ray traced separately. Most of the elements are defined by a reflecting or refracting surface. Therefore each optical element is delimited by continuation planes, the source plane (object plane: OP) and the image plane (IP). The concept of a continuation plane (CP) is used to link the elements together. The continuation plane is an imaginary point in space between consecutive elements where the output of one element becomes the input of the next element [72]. For each optical element, a local reference frame will be defined, normally coincident with the mirror centre or pole. The programme keeps track of the position of each mirror relative to the laboratory reference frame, as this is later used in some of the utilities.

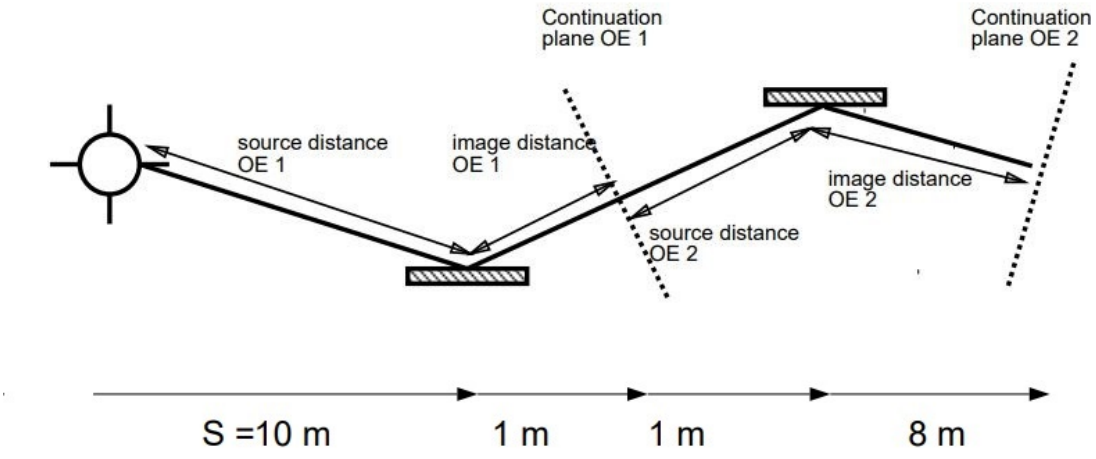

Figure 2.3: Example layout with source and optical system in SHADOW [72].

To have a better understanding of the optical system in SHADOW, Fig. 2.3

shows an example layout of a 20m optical system. The first mirror (OE1) at 10m from source, the second mirror (OE2) at 2m after OE1, the final image at 8m after OE2. Thus the source distance of OE1 is 10m and the image distance is 1m; OE2 has a source distance of 1m and an image distance of 8m (along the optical axis). Although the continuation plane may have no optical value, it is the position that SHADOW passes the ray information from one element to the next.

In this project, SHADOW is used to have a quick check of the beam spot information. Some benchmarks on the SHADOW and SRW simulations will be shown in the next chapter.

2.1.4 Fully coherent and partially coherent beam simulation

Over the past decade, experimental techniques relying on X-ray coherence have emerged. Evidently, the simulations of fully- and partially-coherent SR through optical elements of a beamline are needed.

As discussed in the last section, SHADOW is based on the geometrical ray-tracing method. To simulate a coherent Gaussian beam, it needs special consideration of the source parameters. Since it accepts any beam size and divergence, existing physical constraints must be imposed. In particular, the relation between the RMS source size σ_r and divergence σ'_r of a coherent Gaussian radiation beam, $\sigma_r\sigma'_r = \lambda/4\pi$, where λ is the radiation wavelength, will be taken into account to define a Gaussian beam source for ray tracing simulations. Once this condition is met, in principle ray tracing methods known to retain the phase space volume of the propagating beam can be used to simulate the propagation of the coherent beam, at least for the simulations without apertures where diffraction may occur [73].

For the wavefront propagation simulation method in SRW, the electric field components at a distance from the electron depend on the coordinates of the observa-

tion point x_0, y_0, the radiation frequency ω, as well as on the initial "coordinates" of electrons in 6D phase space (initial horizontal and vertical positions and angles x_e, y_e, x'_e, y'_e, relative energy γ_e and initial longitudinal position z_e) [74]. The electric field propagation in free space or through an optical element of a beamline can be described by a "propagator" which can be represented by [74]

$$\begin{aligned}&\vec{E}_{\perp j}(x_j, y_j, \omega, x_e, y_e, x'_e, y'_e, \gamma_e, z_e)\\&= \iint \mathbf{K}_j(x_j, y_j, x_{j-1}, y_{j-1}, \omega)\vec{E}_{\perp j-1}(x_{j-1}, y_{j-1}, \omega, x_e, y_e, x'_e, y'_e, \gamma_e, z_e)dx_{j-1}dy_{j-1}\end{aligned} \tag{2.7}$$

where $\mathbf{K}_j(x_j, y_j, x_{j-1}, y_{j-1}, \omega)$ is a kernel specific to $j-th$ optical element (j = 1, 2, ...). In general it is a matrix that depends on the frequency and transverse coordinates in a plane before (x_{j-1}, y_{j-1}) and after (x_j, y_j) the optical element. $\vec{E}_{\perp j-1}$ and $\vec{E}_{\perp j}$ are the transverse electric fields in the planes before and after the optical element.

In SRW, a beamline comprises the application of a sequence of "propagators", corresponding to the optical elements and drift spaces. The intensity of the radiation by the entire electron beam after propagation through the $j-th$ optical element of a beamline can be described by

$$\left(\frac{dN_p h}{d\Sigma d\omega/\omega}\right)_j = \frac{c^2\alpha I_e}{4\pi^2 e^3}\left(I_{ISRj} + I_{CSRj}\right) \tag{2.8}$$

where I_e is the electron beam current and α is the fine structure constant. I_{ISRj} and I_{CSRj} are the contributions of "temporally incoherent" and coherent synchrotron radiation respectively. The contribution of the incoherent beam can be written

$$\begin{aligned}&I_{ISRj}(x_j, y_j, \omega)\\&= \int \left|\vec{E}_{\perp j-1}(x_{j-1}, y_{j-1}, \omega, x_e, y_e, x'_e, y'_e, \gamma_e, z_e)\right|^2 f(x_e, y_e, x'_e, y'_e, \gamma_e, z_e)dx_e dy_e dx'_e dy'_e d\gamma_e dz_e\end{aligned} \tag{2.9}$$

In Eq. 2.9, f is a function describing the particle density distribution in 6D phase space, normalized to 1. The coherent synchrotron radiation contribution is

$$I_{CSRj}(x_j, y_j, \omega) = \int \left| \vec{E}_{\perp j-1}(x_{j-1}, y_{j-1}, \omega, x_e, y_e, x'_e, y'_e, \gamma_e, z_e) f(x_e, y_e, x'_e, y'_e, \gamma_e, z_e) dx_e dy_e dx'_e dy'_e d\gamma_e dz_e \right|^2 \tag{2.10}$$

Three simulation modes are available in SRW: "fully coherent", "partially coherent" and "multi-electron" modes. The fully coherent simulation is calculated from single-electron radiation. The partially coherent simulation is obtained by setting macro-electrons with different coordinates in the 6D phase-space, then by propagating the wavefronts produced by these electrons separately through the beamline optics and finally by summing up the electric fields of these wavefronts. The so-called multi-electron mode performs the calculation from a thick (non-zero emittance) beam which was been discussed in section 2.1.2.3.

Compare the ray-tracing model and wavefront model in simulating the beamline performances, some optical effects should be better described by a geometrical ray-tracing model (SHADOW), like aberrations, errors in the optical surfaces. Whereas others, like interference and diffraction, should be better explained using a wavefront model (SRW). Some benchmarks for the fully, partially and low coherent beam simulations by ray-tracing model and wavefront model have been conducted at the National Synchrotron Light Source [73], the Advanced Photon Source and the European Synchrotron Radiation Facility [75]. The result shows that for optical simulations with fully coherent radiation beams, the wavefront propagation method is not only more accurate but also numerically efficient. While the ray-tracing method is more suitable for simulating incoherent beams. These results provide very useful references to the studies in Chapter 3 and 4.

2.1.5 Non-dominated sorting genetic algorithm

A Genetic Algorithm (GA) implements the principles of biological evolution to optimise a multidimensional nonlinear problem. Independent variables can be assimilated to genes, and a sequence of genes (genotype) constitutes an individual. For each individual, the expression of its genes (phenotype) is the solution of the objective function values the algorithm will try to optimise.

Fig. 2.4 shows the flow chart of multidimensional objective genetic algorithms. A group of individuals form the first population, then the operator will evaluate the objective and assign the fitness value for the individuals in the first generation. After the selection, a new generation is formed. As in multidimensional optimisations, genetic algorithms produce new variables based on the characteristics of past individuals.

Fitness is a fundamental concept in GA optimisations, that is used to evaluate how well the problem is solved by the solution. It is used to measure how well an individual meets the optimisation goals. In its simplest form, for a single-objective optimisation, an individual's fitness is its objective function value. In that case, an evolution toward the fittest individual is equivalent to the search for the optimal solution.

For multi-objective optimisations, the fitness function definition should be able to accurately characterize the optimality of each objective value. To achieve this, the concept of dominance is introduced. For a general optimisation problem, all objectives are required to be optimised. If one or more objective values for an individual A is better than the corresponding values for B, and any remaining objective values are equal to B's, we could consider that individual A dominates individual B, in other words, A is non-dominated by B [76].

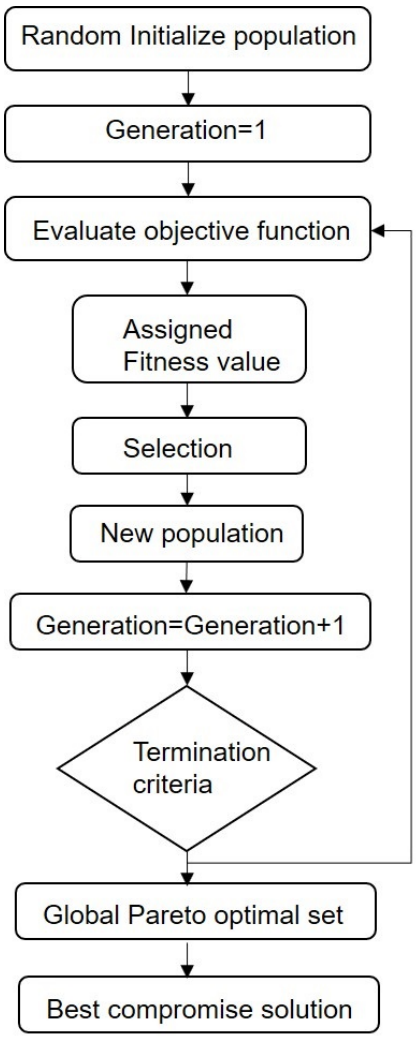

Figure 2.4: Flow chart of NSGA.

The best population is identified as the dominated solution is zero, the solutions in this population is known as non-dominated solutions [58]. Then the dominated solutions are identified from the remaining population. When objectives conflict, the optimisation will have more than one best solution, which form a Pareto-optimal front in search space. Each solution on this front is equally valid, non-dominated by the other solutions on the front, and dominates at least one individual in the search space [58]. This process is conducted repeatedly until all of the populations are sorted. This principle is at the core of the Non-Dominated Sorting Genetic Algorithm (NSGA), described in further detail in [58].

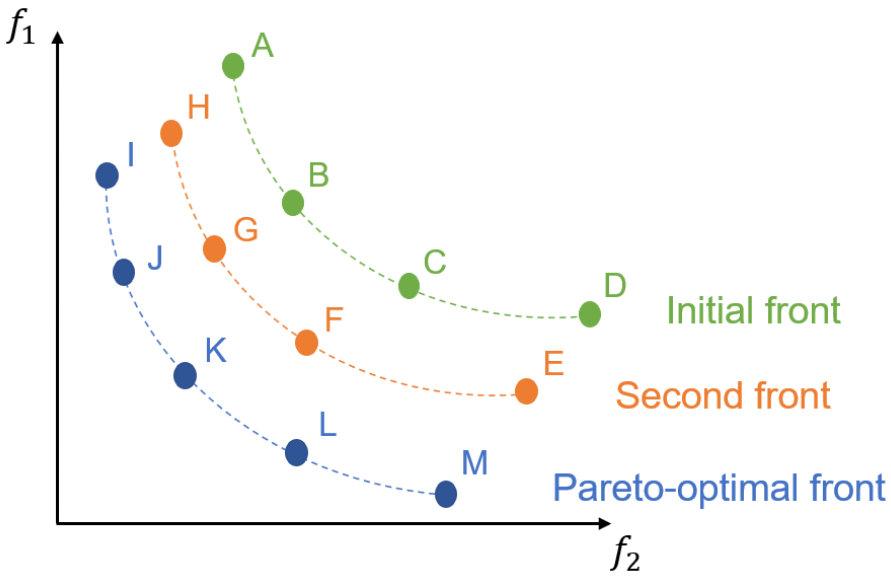

Figure 2.5: Diagram of non-dominated sorting. f_1 and f_2 are two objectives, the goal of this optimisation is to minimise the f_1 and f_2.

Fig. 2.5 shows that points A–D constitute the initial population. Points E–H are then sorted to confirm the population domination and were defined as the second front. All the solutions from A-H are dominated by the solutions I-M in the Pareto-optimal front.

For a complex system like a synchrotron light source involving an electron storage ring and many beamlines, many specifications and physical quantities need to be taken into account. The main goal for accelerator physics design is to achieve an efficient interplay between these quantities, thereby optimising their performances [76]. In order to achieve this, an optimiser based on multi-objective genetic algorithms was developed, aiming to be an efficient tool for the design and optimisation of the system.

2.2 Applications of E2S

At present, E2S can calculate flux, brightness, power density and beam intensity at a downstream point along the beamline. Beamline optics can also be defined for a realistic description of the problem. In this section, some applications and studies

based on E2S will be presented.

2.2.1 Beamline I13

Beamline I13, 250m long, is the longest beamline in Diamond. It comprises two branches, the Coherence and Imaging branch. The two beamlines are operating simultaneously and independently. The I13 long straight section was modified with the "mini-beta" design as shown in Fig. 2.6, obtained by splitting the straight into two shorter sections thanks to the insertion of a defocusing-focusing quadrupole doublet in the middle. The vertical electron beam size is reduced in proportion to the square root of the beta function [77]. This design improves the brilliance by more than one order of magnitude and even more at higher energies compared to the original layout [78]. A setting of large β_x and a positive α_x at centre of an ID is achieved to create a virtual focussing (virtual source point) in the horizontal plane [78]. For the coherence branch, this virtual source point is located at the front-end of the branchline where slit is implemented at this location so that the horizontal source size can be adjusted to the experimental needs [77].

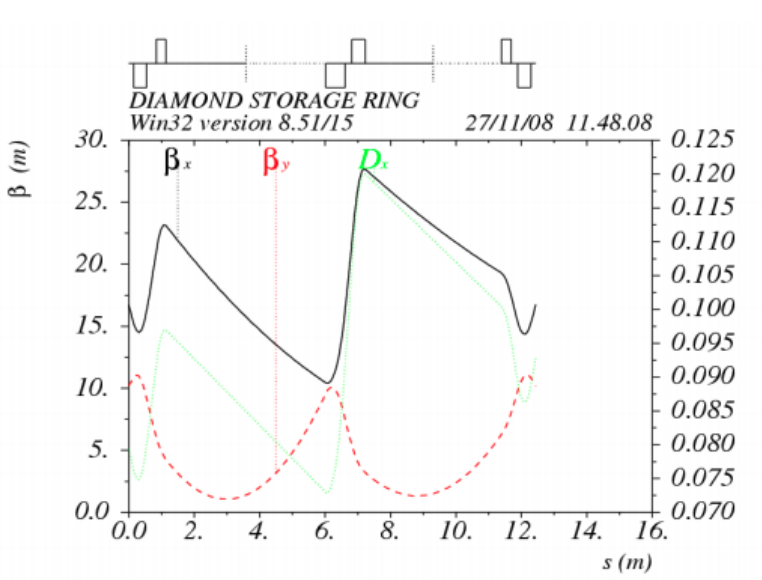

Figure 2.6: The optical functions in the I13 straight section. The insertion devices are set in the two minimum β_y points. (Reprint from [78]).

Coherent diffraction imaging methods require highly coherent X-rays which can not be conducted with conventional laboratory sources. The I13 coherence beamline is built to provide highly coherent X-ray sources [24].

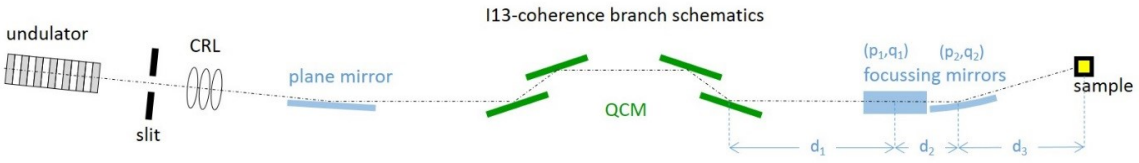

Figure 2.7: A schematic top view of DLS beamline I13 coherence branch model used in this study.

Fig.2.7 presents a schematic of the I13 coherence branch. The coherent fraction of the radiation is selected by the slit at the beginning of the beamline. A compound refractive lens (CRL) is used to collimate the beam so that the flux through the monochromator is maximised. The longitudinal coherence length is adapted with the four-bounce monochromator, consists of a set of Si(111) crystals. A set of KB mirrors is used to focus the beam in two planes. The source utilized for the calculations is an ideal undulator with a period of 25mm, a length of 2.7m and is set to operate at the peak of the 9th harmonic (11.209keV). Table.2.1 shows some of the machine parameters used in the following simulations of the I13 coherence branch in Diamond and its upgrade.

	D_x from waist (m)	D_y from waist (m)	β_x(m)	β_y(m)	α_x	α_y	η_x(m)	δE(%)
DI	1.78	-1.11	26.2	2.4	1.08	0.71	0.14	0.096
DII	1.99	1.99	7.7	4.3	-0.24	-0.53	-0.0035	0.078

Table 2.1: Twiss parameters and the location of the electron beam waist in each plane (D_x means in the horizontal plane, D_y means in the vertical plane) with respect to the ID source point of the I13 coherence branch.

2.2.2 Flux and brightness

In chapter 1.2.2, we described the spectrum of a filament electron beam produced by a planar undulator. It is constituted by a series of harmonic peaks at frequencies that

are multiples of the fundamental frequency ω_r, given by

$$\omega_r = \frac{2c\gamma^2}{\lambda_u(1 + K^2/2 + \gamma^2\theta_x^2 + \gamma^2\theta_z^2)} \tag{2.11}$$

where (θ_x, θ_z) are the horizontal and vertical angles between the electron and the observation point. The width of the peaks is equal to $\frac{1}{nN}$ where n is the harmonic number and N is the number of undulator periods [7]. Therefore the extremely narrow peak (Fig. 1.6) is only visible when observed from a many period undulator on a high harmonic number. In real situations, for a thick electron beam, all the electrons do not have the same resonant frequency ω_r. This occurs because the angular divergence of the electron beam will spread both the horizontal and vertical angle of observation θ_x, θ_z which gives a spread of resonant frequency. On the other hand, ω_r is proportional to the square of the electron energy, therefore a spread of the electron energy will cause a spread of frequency.

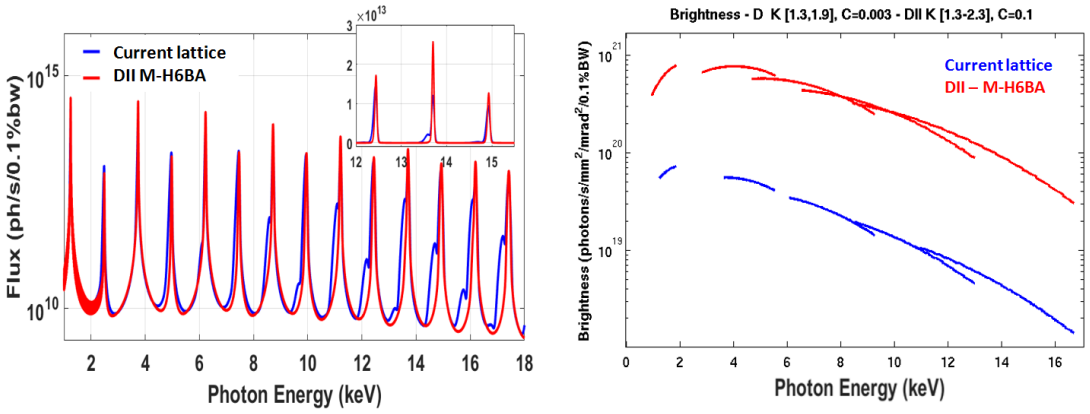

Figure 2.8: Partial flux (left) and brightness (right) at I13-coherence with the current Diamond (blue) Twiss parameters at straight 13 and Diamond II (red) with the new ones for the M-H6BA case design for Diamond-II. The K value for the spectrum calculation is 1.87. For the brightness calculation, the scanning range of K for Diamond is 1.3 to 1.9, for Diamond II is 1.3 to 2.3.

Normally, the observer will collect the flux from a finite aperture, and the value of ω_r varies from different points inside the aperture. In E2S, the spectral flux within

a finite aperture calculation in SRW is obtained. The aperture position and size are defined in the E2S input file. Fig. 2.8 (left) shows a comparison of the photon flux generated by the current and M-H6BA lattices in straight 13 for a typical front end aperture of $(300\mu m, 120\mu m)$. While the total flux is virtually unchanged, the partial flux at the front-end is marginally increased thanks to the emittance reduction in the new machine (2700pm to 160pm).

The brightness simulation in E2S is calculated in Elegant. The scanning range of K and the number of harmonics can be defined in the E2S input file. The brightness data will be saved in columns for requested harmonics which make it easier during post-processing. Fig. 2.8 (right) shows the increase in brightness for Diamond II compared with Diamond in the straight 13. From the description of brightness in 1.2.2, the source size and divergence are two important factors that determine the brightness. Thus, the roughly 20 times reduction in emittance for Diamond II gives a clear improvement in brightness.

2.2.3 Intensity and Power density simulation

In E2S, the intensity of the photon beams at certain photon energy can be calculated. Intensity is calculated from the flux, and describes a flux per unit area at a (distant) plane where radiation is collected (e.g. at the sample point or at the detector).

Fig. 2.9 is an example of beam intensity distributions at the sample position calculated with this code. The photon energy chosen is close to the flux peak corresponding to the 9th harmonic.

SPECTRA [79] is an application software used to calculate the optical properties of synchrotron radiation. From the past studies, we found SRW can propagate the radiation through the optics of a beamline only for a single wavelength and in SPECTRA the propagation through a beamline is not available. Therefore, with

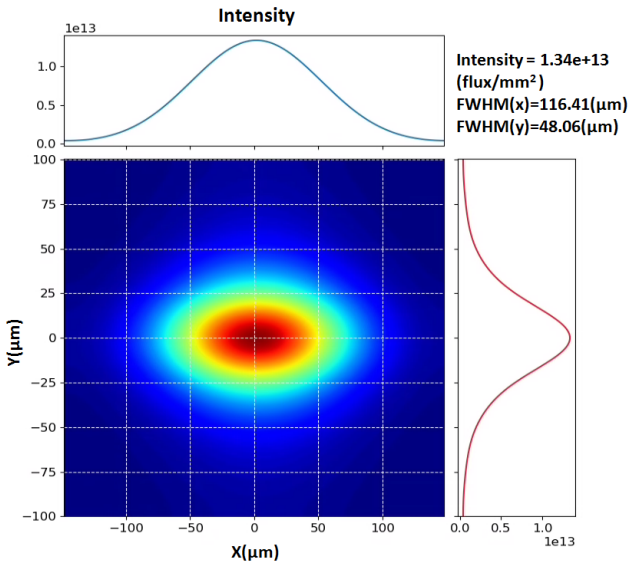

Figure 2.9: Beam intensity distribution at the sample position in beamline I13 coherence branch.

both codes a generic power density distribution can only be simulated in free space propagation. A method has been implemented to overcome such limitations allowing the propagation of radiation with a generic power spectral density.

To simulate a generic power density distribution, the power density distributions in a sequence of energy bins are calculated, then all the distributions are summed together. The first test is done with the beamline I13 coherence branch. To benchmark our method we first consider propagation in free space from the source point to the entry slit. Fig. 2.11 (right) represents the power density calculated by SRW, from which it appears that a window of 8×8 mm^2 is sufficient to capture 99.9% of the deposited power.

Fig. 2.10 shows the photon flux corresponding to the chosen aperture, where it appears that the number of photons is very low for energy $>$ 30keV. This justifies the choice of limiting the intensity distribution between 1eV and 30KeV, in bins of 1eV. Therefore, 30K intensity distributions are simulated. Since the total number of pixels in all intensity distributions has been set equal, it would be possible to sum the

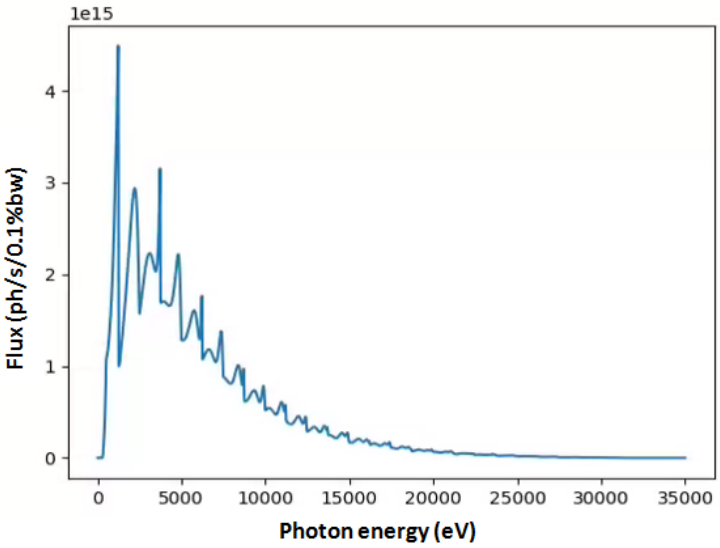

Figure 2.10: Photon flux through an $8 \times 8mm^2$ aperture

intensities for all energies for each pixel. Fig. 2.11 left presents the result of the sum of the intensities. Then a 2D integration can be applied to calculate the total power in a summed distribution. The comparison of the power density calculated with this procedure and the standard SRW free drift propagation simulation shows a good agreement and confirms the feasibility of the method. The total power calculated from SRW is 2795W, while the value calculated with our integration approach in the horizontal and vertical planes is 2745W.

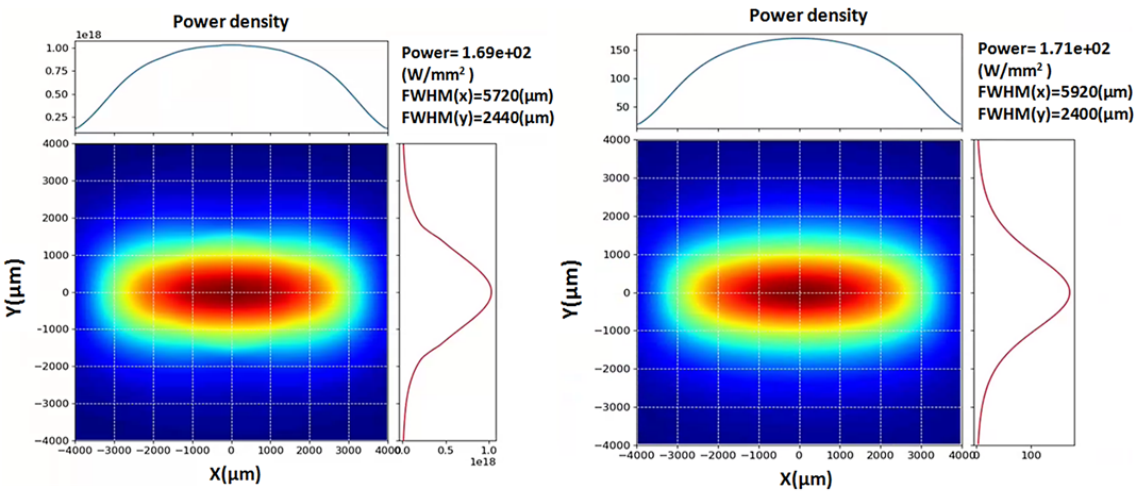

Figure 2.11: Left: Power density distribution at slit position approximated from intensities of beam energy 1eV to 30KeV. Right: Power density distribution at the slit position simulated from SRW.

The advantage of this binning procedure is that it allows one to calculate the power density distribution at any arbitrary position down the beamline. The same procedure was repeated to simulate the power density distribution after the first aperture and at the sample (Fig. 2.12).

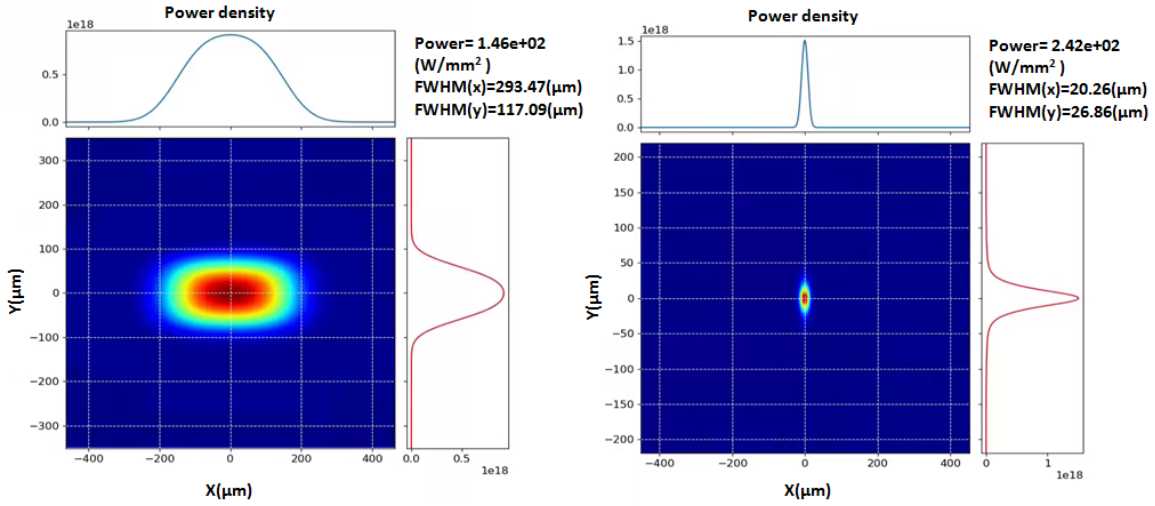

Figure 2.12: Left: Approximation of power density distribution after first slit: the effect of the aperture size (300μm$\times 120\mu$m) is evident. Right: Approximation of power density distribution at the sample, where the SR radiation is focused.

2.2.4 Orbit correction study in the I13 coherence beamline

One important aspect when operating a beamline is understanding the effects of variations in the electron beam orbit in the region where the insertion device is located. Changes in the transverse position and angles (Fig. 2.13) can propagate through the beamline up to the sample. The source point position and angle are controlled by the Beam Position Monitors (BPM) at the upstream and downstream ends of the insertion device (ID). However due to the imperfect nature of the correction, some residual shifts or angles may be present.

Figure 2.13: Source shift (left) in the horizontal plane with distance δ_x and tilt (right) in the horizontal plane with angle δ_x'.

All these effects can eventually degrade the properties of the transmitted radiation, either moving the position of the beam-spot at the sample plane or reducing its intensity or both. E2S is suited to reproduce these effects of orbit change in the storage ring. In this section, a study of the effect of orbit variation in I13 coherence branch is presented.

The elements used in the SRW simulation are shown in Fig. 2.7. The source for this beamline is modelled as an ideal 2.7m long undulator, with a period of 25mm and $K = 1.87$. The relevant elements of the beamline are a compound refractive lens (CRL) located at 21.55m from the source, a plane mirror at 26.25m, a four crystal horizontal monochromator (209m), a Kirkpatrick-Baez system [33] (at about 220.4m) and the sample (located at 228m). Before delving into the study of the beamline,

some steps to characterize and benchmark the behaviour of a few key elements of the system are considered.

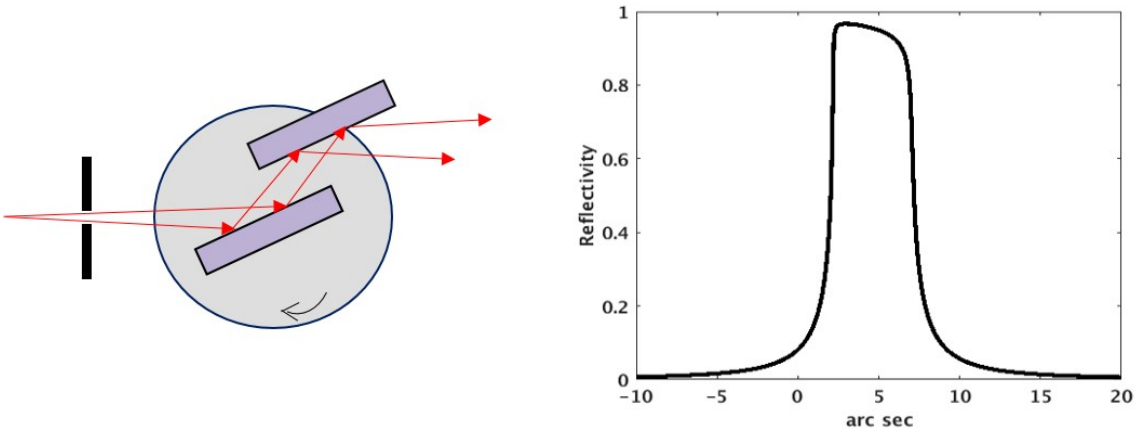

Figure 2.14: (Left) A schematic of the apparatus used to measure a rocking curve. (Right) Single crystal rocking curve for Si(111) at 11.209keV. The horizontal axis is the rotation angle of the crystal when measure the rocking curve.

As the first benchmark, the effect of the Si(111) crystal quad-monochromator (QCM) in I13-coherence is verified. Crystal reflectivity can be described by means of a rocking curve [80]. Fig. 2.14 (left) shows the set up used to measure the rocking curve of a double crystal monochromator. When the monochromator rotates, the incident angle will change correspondingly. Fig. 2.14 (right) is the rocking curve for single Si(111) crystal at 11.209keV [81].

The incident photon beam angle does not need to be identical to the Bragg angle but must in the range of angles from the Darwin width (or rocking curve width) of the crystal typically several arc seconds. For I13 coherence branch, with 11.209kev photon beam, the Bragg angle is 0.1773 rad for the first order of diffraction. The incoming photon beam within around $\pm$ 23.58μrad corresponding to the wavelength 1.106e-10 m is selected by the QCM.

In the general case, the photon beam from an insertion device has a natural divergence, which will affect the selection of the photon beam as described in 1.5.2. In the I13 coherence branch, the natural photon beam divergence is 17.2μrad. Fig. 2.15 illustrates the rocking curves of Si(111) crystal with different beam divergences, 17.2 μrad (blue), 4 μrad (red) and 1 μrad (green). This simulation is done by tilting the photon source while keeping the monochromator fixed in space, resulting in a curve with opposite symmetry with respect to the reference curve shown in Fig. 2.14.

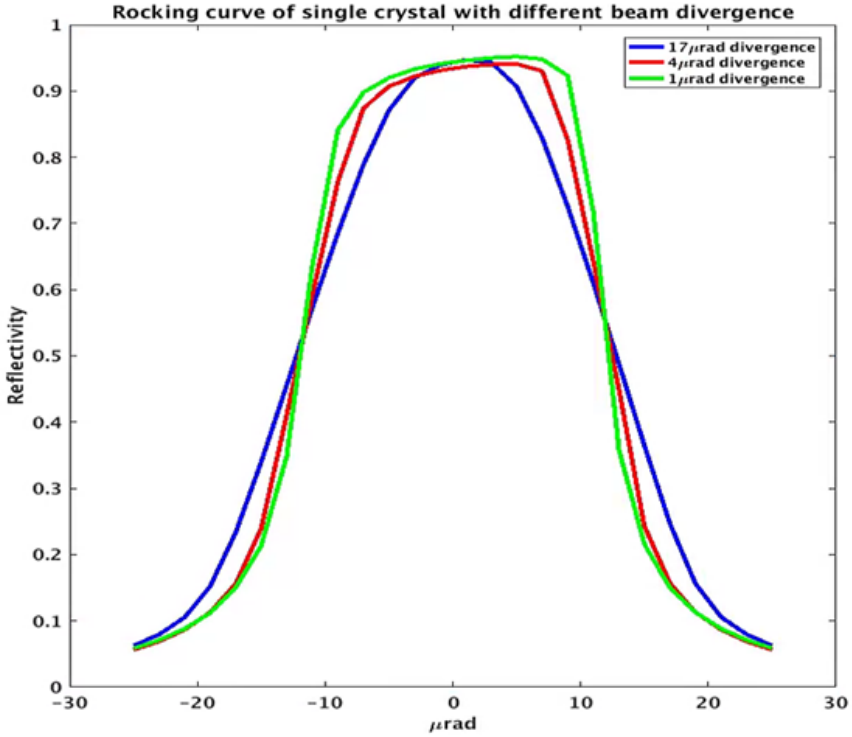

Figure 2.15: The rocking curve produced with beam divergence of 17.2μrad, 4μrad and 1 μrad

It is well known that monochromators are used to select a specific photon energy for a beamline; if the monochromator is tuned to transport a given energy, then the beam is fully transmitted only within a narrow band. After minimizing the effect of energy resolution, an ideal pencil beam case was simulated to pass the crystals. First, the reflectivity curve for a single Si(111) crystal is evaluated for a photon energy

scan. Then the curve is compared to the same calculation using an angular tilt of the photon source scan to illustrate the equivalence of the two methods. The photon source angular tilt is generated by means of the CRL, by shifting the electron beam horizontally which will be described in detail in par. 2.2.4.2.

Fig. 2.16 summarizes simulation results of the two methods and shows a comparison with a typical rocking curve as found in Fig. 2.14 (right).

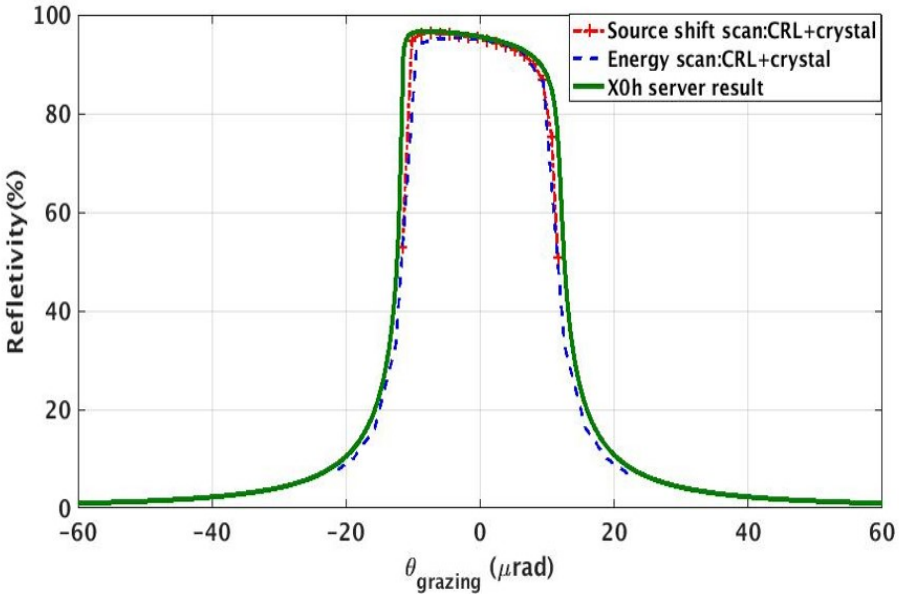

Figure 2.16: Reflectivity curve obtained by scanning the energy of a beam through a single Si(111) crystal (blue dashed curve), and by tilting and collimating the incoming beam by means of a CRL lens (red dashed curve). This is consistent with the theoretical result as found in [81] (green curve).

2.2.4.1 Orbit angular tilt

As discussed in the previous paragraph, one key optical element of this beamline is given by the CRL lens, which is used to collimate the beam. In order to simulate the effect of a horizontal tilt of the source equal to $\delta x'$ we have considered a simplified system made of a drift D_1 followed by a CRL with focal length f. The system can be parametrized by:

$$\begin{pmatrix} 1 & 0 \\ \frac{-1}{f} & 1 \end{pmatrix} \begin{pmatrix} 1 & D_1 \\ 0 & 1 \end{pmatrix} \begin{pmatrix} 0 \\ \delta x' \end{pmatrix} = \begin{pmatrix} \delta x' D_1 \\ (1 - \frac{D_1}{f})\delta x' \end{pmatrix} \tag{2.12}$$

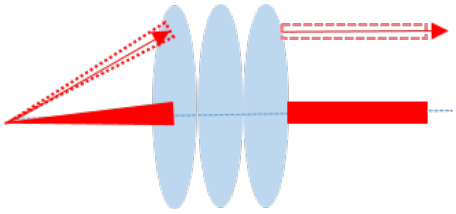

Figure 2.17: A beam with an angular tilt will be collimated by the CRL. The full red beam is a perfectly aligned case, while the dashed lines represent the beam at source with an angular tilt

In I13 coherence branch, D_1 is equal to 21.549m, and f is equal to 21.573m. The ratio of these quantities, D_1/f is very close to 1, so after the CRL, the angle becomes 0 therefore producing a collimated parallel photon beam as shown in Fig. 2.17. For this reason, the incident angle at the monochromator is basically unchanged by the angular tilt of photon source, while the photon beam spot after the lens is shifted by a quantity equal to $\delta x' D_1$.

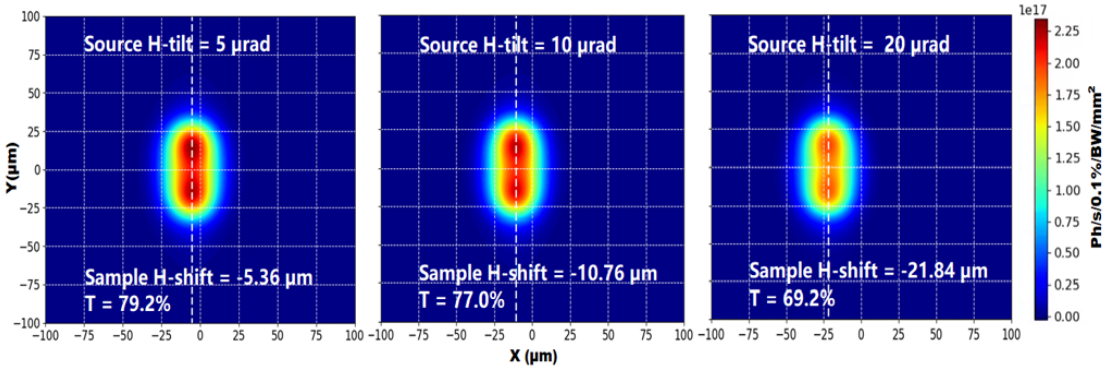

Figure 2.18: Effect of orbit angular tilts in the horizontal plane at the centre of the ID, for three different angular tilts at the source: (left) 5 μrad, (centre) 10 μrad and (right) 20μrad.

The transmission of the whole beamline as a function of the angular offset at the sample plane is shown in Fig. 2.18, where the photon beam position is observed as a function of the angular tilt of the electron beam. It can be seen that the reduction

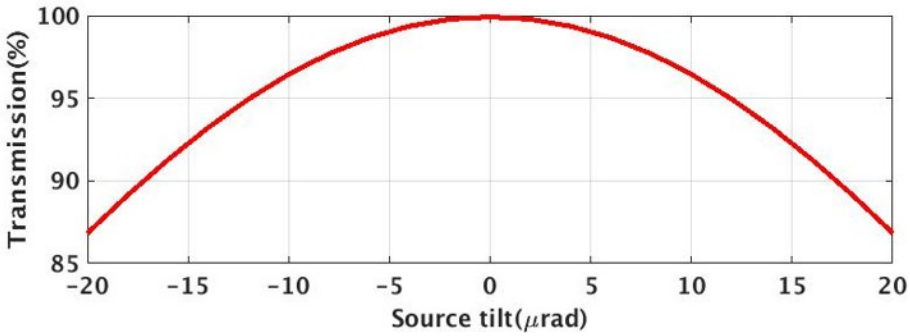

Figure 2.19: Transmission curve of CRL corresponding to angular tilts of the source from -20 to +20 μrad.

in transmission is mainly due to the absorption in the beryllium crossed at the CRL, as graphically summarized by Fig. 2.19.

2.2.4.2 Orbit shifts

When the beam is shifted horizontally, the CRL will introduce an angular change of -$\frac{\delta x}{f}$, as can be inferred from equation 2.13. This angular effect is shown in Fig. 2.20.

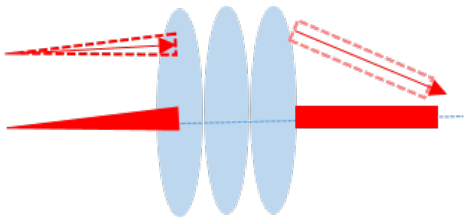

Figure 2.20: A beam with a shift in horizontal plane will be tilted after CRL. The solid red beam represents the nominal case, the dashed line is the beam at source with a horizontal shift.

$$\begin{pmatrix} 1 & 0 \\ \frac{-1}{f} & 1 \end{pmatrix} \begin{pmatrix} 1 & D_1 \\ 0 & 1 \end{pmatrix} \begin{pmatrix} \delta x \\ 0 \end{pmatrix} = \begin{pmatrix} \delta x \\ -\frac{\delta x}{f} \end{pmatrix} \tag{2.13}$$

Since the monochromator is set to transmit a well defined energy corresponding to the Bragg condition, any angular tilt will result in a reduction in transmission, which is clearly captured in Fig. 2.21.

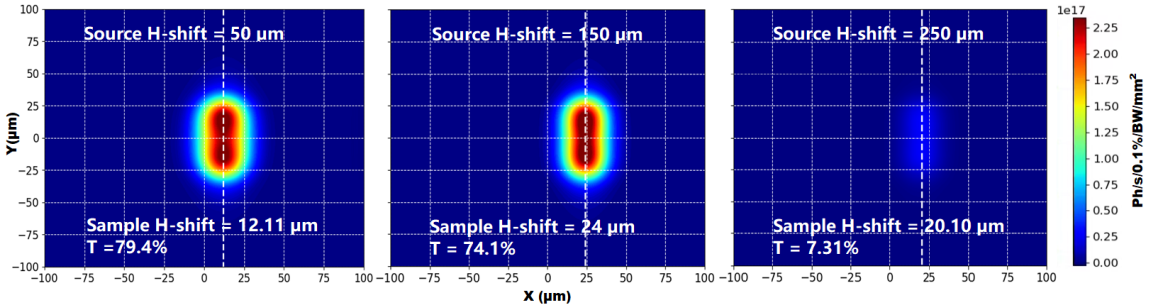

Figure 2.21: Orbit side shift in the horizontal plane at the centre of the ID, for three different displacements at the source: (left) 50 μm, (centre) 150 μm and (right) 250 μm. The sharp decrease in intensity (right most picture) corresponds to an angular change of about 11.6μrad, falling out of the energy bandwidth for our monochromator.

2.2.4.3 Transmission through the beamline with orbit variation

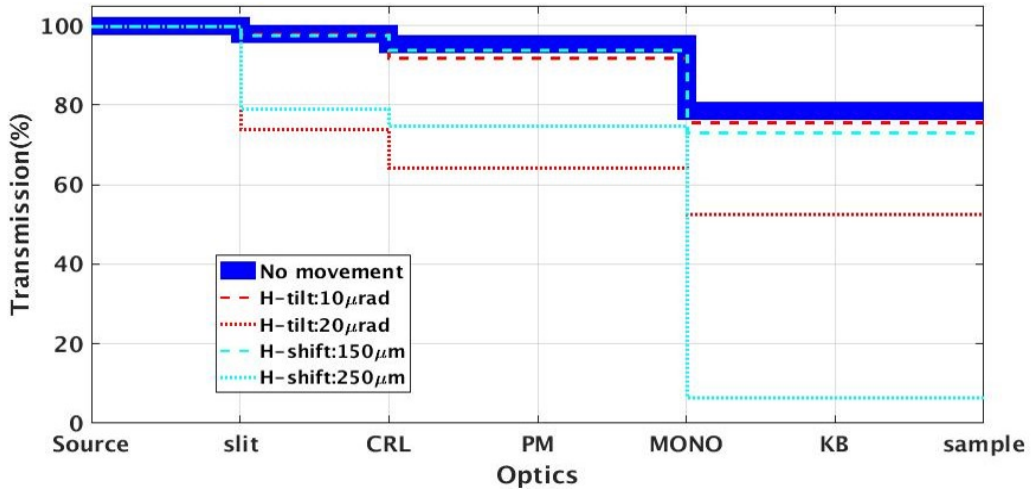

Figure 2.22: Transmission change along the whole beamline corresponding to source movements. In this case we adopted a slit of 600×240 μm^2 whose effect is clearly visible at large shifts and tilts.

The overall transmission, shown in Fig. 2.22 for different shifts and tilts of the source, summarizes our understanding of the main processes happening during the propagation of the wave-front through I13-coherence. CRL and monochromator are both equally important in presence of a photon beam tilt, while the monochromator becomes the dominating element for large shifts due to the bandwidth considerations

given in section 2.2.4.2.

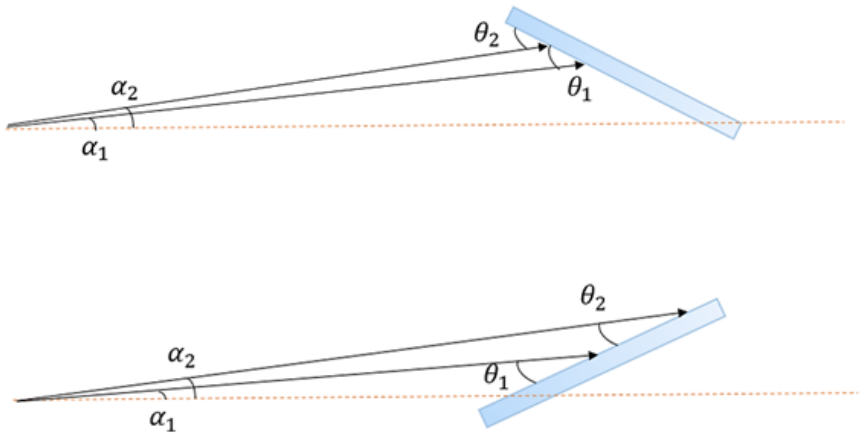

Figure 2.23: A setup to measure rocking curve of crystals with diffraction plane angle $\pi/2$ (top) and $\pi+\ \pi/2$ (bottom). When the photon beam source is tilted from α_1 to α_2, the incident angle θ changes from θ_1 to θ_2.

For the I13 QCM, every pair of crystals is set with diffraction plane angle $\pi/2$ and $\pi+\ \pi/2$ as shown in Fig. 2.23. When the beam source is tilted from α_1 to α_2, the grazing angle of a crystal with diffraction plane angle $\pi/2$ (top figure) is increasing ($\theta_2 > \theta_1$), on the contrary, the grazing angle of crystal with diffraction plane angle $\pi+\ \pi/2$ (bottom figure) is decreasing ($\theta_2 < \theta_1$). This causes the rocking curve flip (Fig. 2.24).

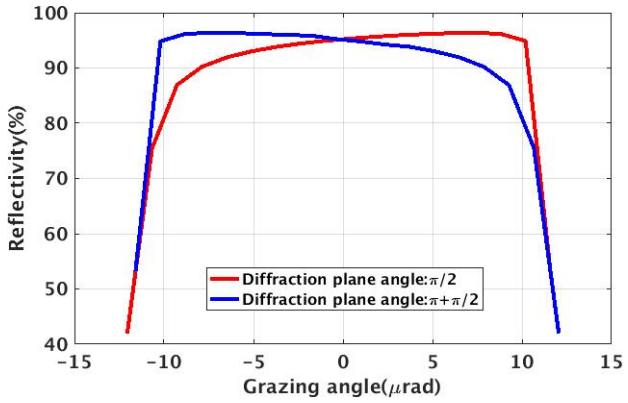

Figure 2.24: Measured rocking curve of crystals with diffraction plane angle $\pi/2$ (red) and $\pi+\ \pi/2$(blue).

Fig. 2.25 shows the transmission curve of the four-bounce monochromator as a function of the grazing angle -$\frac{\delta x}{f}$ due to a shift scan, compared to an energy scan curve.

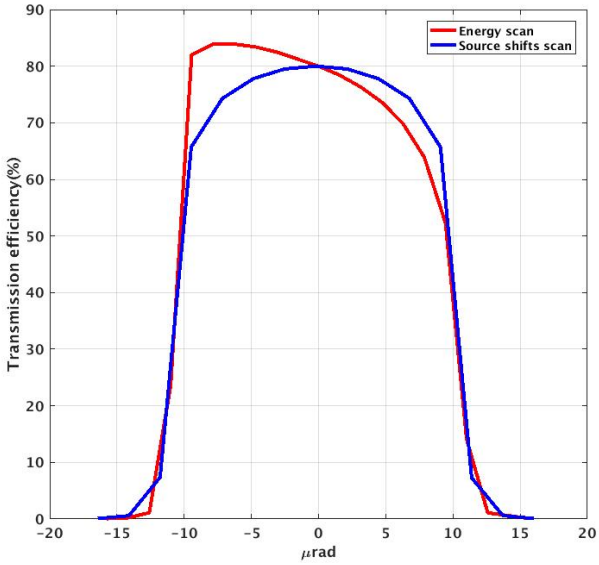

Figure 2.25: Transmission curve for the Si(111) crystal monochromator from energy (red) and source shifts (blue) scan as computed by SRW in E2S. The energy dependence is translated into its Bragg angle by Bragg condition refer to formula 1.82, shifts scan curve is plotted agains an angle defined by the CRL focussing formula -$\frac{\delta x}{f}$.

The typical asymmetry observed as in Fig. 2.16 vanishes when using a series of crystals with alternated orientation, as in the QCM used for this study. The main reason for this behaviour is due to the ($\pi/2$, $\pi/2+\pi$, $\pi/2+\pi$, $\pi/2$) orientation of the crystals as described.

A summary of the effect of electron beam orbit variations at the source point is presented in Table 2.2.

Shifts/Tilt	total photons	$\sigma_x(\mu\text{m})$	$\sigma_y(\mu\text{m})$	x-center (μm)
0	3.99×10^{14}	10.35	20.88	-0.06
50(μm)	3.97×10^{14}	10.79	20.90	12.11
150(μm)	3.70×10^{14}	9.76	20.97	24.00
250(μm)	3.65×10^{13}	10.70	21.69	20.10
5(μrad)	3.96×10^{14}	11.05	20.89	-5.35
10(μrad)	3.85×10^{14}	11.16	20.90	-10.78
20(μrad)	3.46×10^{14}	11.86	21.10	-21.84

Table 2.2: Effect of orbit variations at an ID due to local shifts and tilts in the horizontal plane. The total number of photons, beam size and beam spot position at the sample plane are shown.

2.3 Summary of this chapter

To realize the full simulation from electrons generating the synchrotron radiation to the final sample plane, a wrapper code package called E2S was developed. A beamline optimiser based on the NSGA II has been implemented in E2S. The code environment and simulation theory have been introduced in this chapter.

Some typical examples of the applications of E2S for X-ray property simulations were presented. A method based on E2S was proposed to overcome the problem of propagating the power density distribution along the beamline. The study of orbit corrections in the I13 coherence branch gives a better understanding of the propagation of the wavefront through the beamline with orbit variations. The selection property of the monochromator was also verified in this study which shows good agreement with the theory.

Chapter 3

Optimisation of beamlines based on wavefront model

As described in chapter 2, two well-known synchrotron radiation simulation methods have been implemented in the E2S optimiser. One of them is based on the SRW wavefront method, hence the name E2S-SRW optimiser. In this chapter, the optimisation of two beamline configurations by using the E2S-SRW optimiser will be shown. The photon sources of the two beamlines are an undulator and a wiggler respectively. Having covered two types of insertion devices, it will be straightforward to extrapolate the conclusions of these two types of beamline to other situations.

3.1 Undulator beamline optimisation

The undulator beamline used for our first optimisation test is the I13 coherence branch. The beamline configuration has been introduced in section 2.2.1, the photon source utilized for the calculations is an ideal undulator with a period of 25 mm and a length of 2.7 m. The Twiss parameters used in the simulations are shown in Table. 2.1. This beamline is built to conduct the experiments which require highly coherent X-rays, hence the goal of this beamline design is to maximise the coherent flux: mirrors and the monochromator are used to eliminate vibrations in the highly coherent vertical direction, the horizontal coherence length is adaptable with slits installed at the front-end and the longitudinal coherence length is adapted with the four-bounce monochromator [77]. In order to keep the current coherent fraction of this beamline, the parameters chosen for the following optimisations are from the focussing system (the KB mirrors) to minimize the beamsize and increase the intensity of beam spot at the sample position.

This optimisation has been carried out in four steps:

- First, the beamline has been optimised with a subset of the beamline variables only. The parameter spaces change from 2 dimensional (2D) to 7 dimensional (7D) to show the effect of extending the parameter space on beamline optimisation. At this stage, the source parameters (moments and Twiss parameters) and the remaining beamline parameters are supposed to be fixed.

- In a realistic case, the beamline can start with either a well-designed state or uncertain state. Thus in the second stage, the optimisation of a non-optimised beamline will be shown (called ′Random beamline′). This optimisation is also focused on the beamline variables only.

- Then in the next step, source parameters have been taken into account to

optimise the beamline. We will show the effect of Twiss parameters on beamline optimisation.

- All of the optimisations mentioned above are investigated under a multi-electron simulation in SRW (the calculation theory of three simulation modes have been introduced in Chapter 2). To explore if the optimised beamline can still work as we expect in a partially coherent mode, the simulations in partially coherent mode in SRW have been repeated.

3.1.1 2D and 7D Beamline optimisation

The optics of the accelerator lattice is known and imposed by the geometry of the design, the beamline optimisation runs here solely on a subset of the beamline itself. The objective of this optimisation is beam size, characterized by the two variables σ_x and σ_y, the standard deviations of the horizontal and vertical size of the beam as imaged at the sample plane. The first optimisation is executed with a two dimensional parameter space, defined by the last two drifts of the baseline (d_2 and d_3 in Fig. 2.7).

Fig. 3.1 demonstrates that the iteration fronts for this 2D-constrained dynamics converge towards an envelope close to the Pareto front previously introduced. Two distinct regions can be noticed in the top-left and bottom-right. With the improvement of beam size in one plane, the beam size in another plane will be sacrificed. This is the feature of this 2D optimisation study, only one of the objectives in beam size can be reduced significantly. Due to the small number of parameters and the constraints of d_2 and d_3, the optimisation is mainly acting on the horizontally focusing mirror of the KB system which causes the limited effect and two distinct regions in the final front.

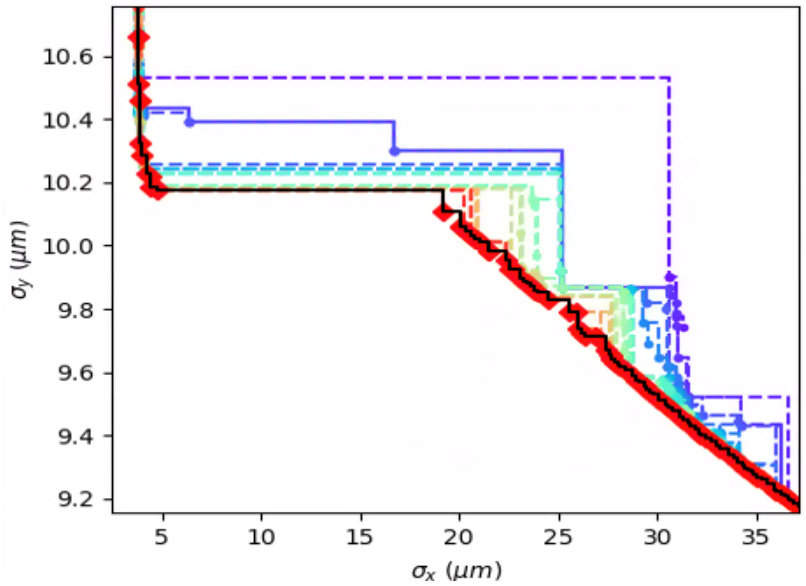

Figure 3.1: Pareto front of the 2D optimisation. Different colours and line types (dashed line and solid line) represent different fronts, the dots on the fronts correspond to the solutions. The black line with red dots is the last generation.

A particular solution is extracted from the Pareto front. It shows that in the process, the beam size can be reduced from $(\sigma_x, \sigma_y) = (17.94, 10.27)\mu$m to $(\sigma_x, \sigma_y) = (4.50, 10.20)\mu$m, with an almost negligible improvement in the vertical size.

Table. 3.1 shows that the optimisation is obtained for a set of parameters that is experimentally realistic.

	d_2(m)	d_3(m)	(σ_x,σ_y) (μm,μm)
baseline	2.20	5.50	(17.94, 10.27)
optimised	1.32	5.92	(4.50, 10.20)

Table 3.1: 2D-Optimisation of Beam Size

The next step is to see if the above results can be improved by extending the parameter space. To achieve this, five new parameters have been added. Referring to Fig. 2.7, these parameters are: the focal distances of each elliptical mirror of the KB system (p_1, q_1, p_2, q_2) and the drift from the last elliptical mirror to the sample (d_1). This sets up the multi-objective problem in a 7-dimensional parameter space. The computation of the genetic algorithm runs on a population of 100 individuals

and over 50 generations.

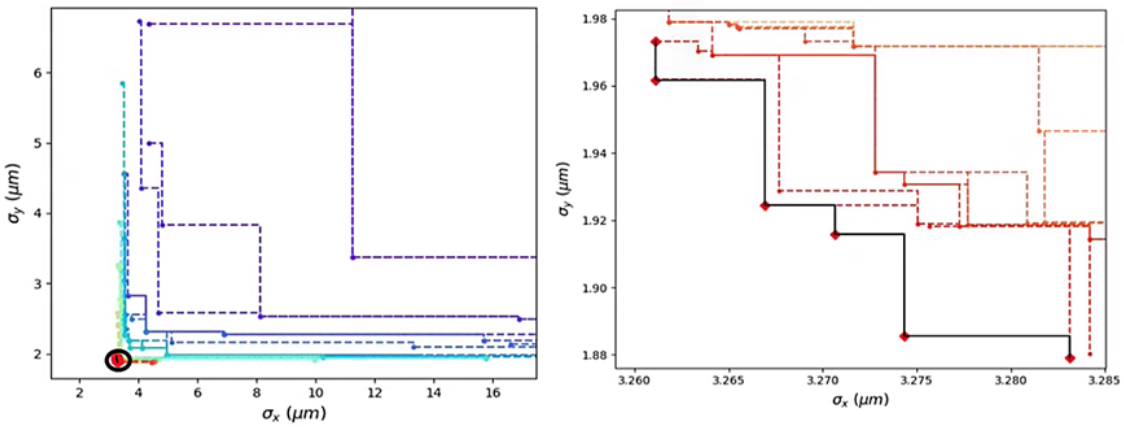

Figure 3.2: Left: Optimisation fronts of beamline I13 coherence branch. Right: zoom-in of dark circle part. Different colours and line types (dashed line and solid line) represent different fronts, the dots on the fronts correspond to the solutions. The black line with red dots is the last generation.

Fig. 3.2 (left) shows that the objectives converge towards a smooth envelope. More and more solutions coalesce around the dark circle which is expanded in Fig. 3.2 (right). This zoomed-in plot illustrates how the best set of configurations for this optimisation has been achieved.

	d_1(m)	d_2(m)	d_3(m)	p_1(m)	q_1(m)	p_2(m)	q_2(m)	σ_x(μm)	σ_y(μm)	I(flux/mm^2)
baseline	10.00	2.20	5.50	30.90	9.10	33.10	6.90	17.94	10.27	2.68e+17
Generation 8	9.00	1.87	5.06	31.13	8.99	32.33	6.02	8.11	2.53	3.11e+18
Generation 38	11.11	1.50	5.00	34.31	7.96	31.69	5.76	3.44	1.91	9.54e+18
Generation 50	11.09	1.33	5.00	30.65	7.93	32.50	5.74	3.27	1.88	1.04e+19

Table 3.2: Parameters used for the 7D optimisation, together with the objectives during several phases of NSGA evolution towards a beamline with a very small image at the sample plane.

Table. 3.2 records the improvement as the program progresses. We can clearly see that as the number of computed generations increases, the horizontal and vertical beam sizes become more confined at the sample position. The optimisation is quite efficient in that after eight generations we already have seen a significant improvement. After 40 generations, the improvement is only marginal suggesting the Pareto front has been reached for this problem. The last column in this table reports the increase

of the beam spot maximal intensity, which, albeit not an objective in our optimisation, is directly linked to the formation of a smaller image.

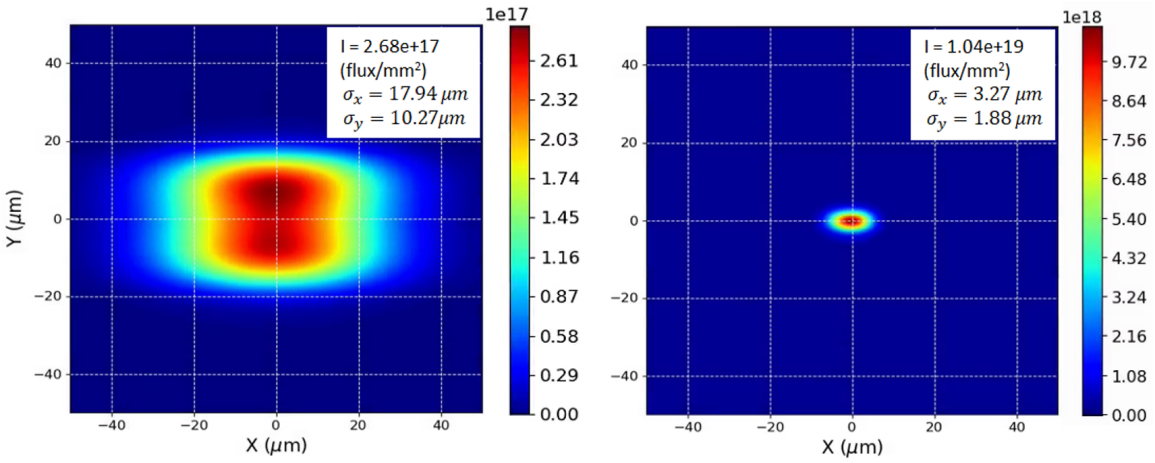

Figure 3.3: Left: initial beam spot at sample with the baseline configuration of I13 coherence branch. Right: optimised beam spot at sample.

A comparison of the beam spot before and after optimisations at sample position is shown in Fig. 3.3. Compared with the 2D optimisation, a 7D optimisation gives a comprehensive improvement in both objectives. This suggests that the solution to the multi-objective optimisation of beamline depends on the parameter space that defines the geometry of the problem [82].

3.1.2 Optimisation of an initially poorly designed beamline: the "random" beamline

Typically, a beamline is designed according to specific criteria, meant to maximize the intensity at the sample, reduce the size at the sample plane or the divergence of the beam itself, to quote some typical goals. The experience of the designer plays indeed a key role in this initial phase. The optimisation technique hereby studied can represent an important complement to a purely human intervention. What we are interested in is whether we would converge towards the same previously found solution from a non-optimised beamline, which initially produces a beam spot significantly larger

than the current beam size. To explore this situation, a random configuration of the current beamline has been built. Seven parameters (p_1, q_1, p_2, q_2, d_1, d_2, d_3) are set (Table 3.3) the second line which initially yields a beam spot at the sample with size $\sigma_x = 58.66\mu m, \sigma_y = 74.82\mu m$ as shown in the left figure of Fig. 3.4. The optimisation algorithm has been run this time starting from this random configuration.

	d_1(m)	d_2(m)	d_3(m)	p_1(m)	q_1(m)	p_2(m)	q_2(m)	$\sigma_x(\mu$m)	$\sigma_y(\mu$m)	I(flux/mm^2)
Initial	9.88	3.40	6.87	29.13	7.97	29.60	6.81	58.66	74.82	1.28e+16
Optimised	12.98	1.68	5.38	31.94	9.00	34.24	6.20	3.49	2.08	9.04e+18

Table 3.3: BL optimisation of I13d start with a random beamline.

Table 3.3 shows that the algorithm converges towards values of the objective functions that are essentially the same as the previous optimisation case presented in Table. 3.2, which means the initial values of beamline parameters do not affect the results of the optimisation. We note that the parameters for these two optimisations are different, the reason is the optimisation range for each parameter is artificially constrained, so different beamline parameter settings can produce equivalent results.

Fig. 3.4 shows the beam spot before and after this optimisation.

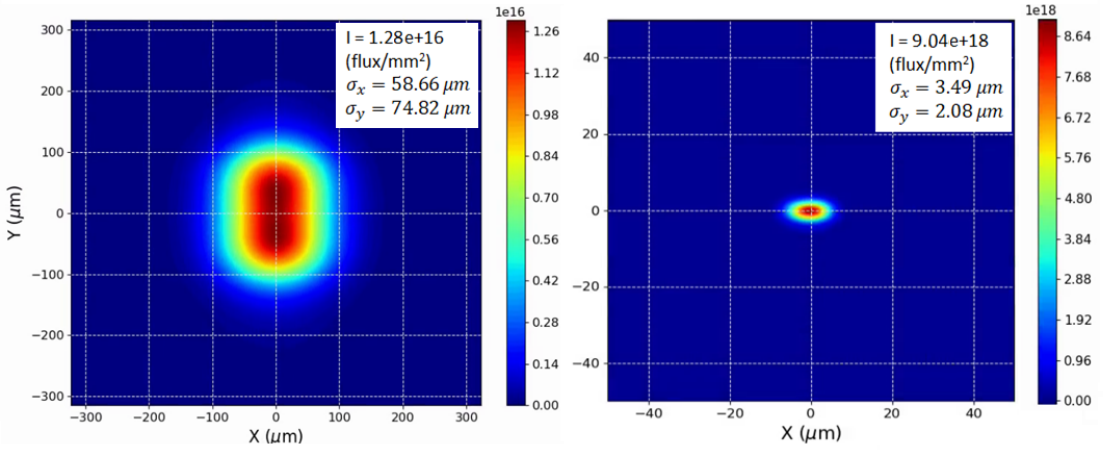

Figure 3.4: Left: initial beam spot at the sample with a random machine set of I13 coherence branch. Right: optimised beam spot at the sample.

Fig. 3.5 shows the phenomenon of "front transition", which happened in our optimisations. In the algorithm, the solutions in the algorithm converge to a front and will gradually densely populate. However at some point, the algorithm will "jump" to another front which will provide a better optimisation of the objectives, and then populate this second front. This mechanism happens because the first front corresponds to a local minimum that can be escaped when a sufficient number of parameters have been explored, and is a feature of genetic optimisation. It should be remarked that it is not possible to predict whether more fronts would appear if the algorithm were to run for a sufficiently large number of iterations.

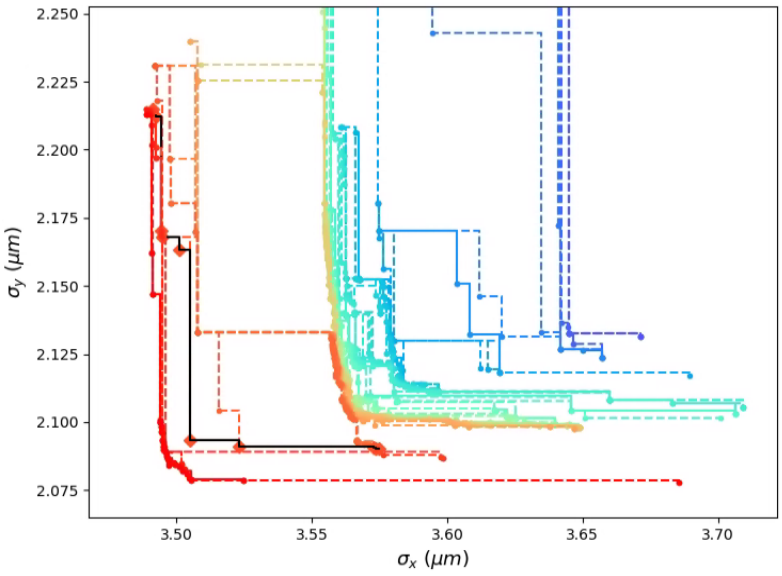

Figure 3.5: Convergence fronts produced by optimising the random beamline. Different colours and line types (dashed line and solid line) represent different fronts, the dots on the fronts correspond to the solutions. The red solid line is the last generation.

In our simulations, this effect will not matter much, because the goal is to reduce the beam size significantly compared to the beam size from the baseline configuration. In reality, the desired beam size is not as small as possible, the optimisation is successful as long as it reaches the target beam size.

3.1.3 Beamline optimisation with source parameters

Next, we study the effect of accelerator optics on the beam spot at the sample position. The accelerator optics are characterized by the Twiss parameters β_x, β_y, α_x, α_y, η_x and η'_x at the centre of the insertion device where usually the beta functions present a waist in the middle of the straight section. However, in the specific case of the I13 coherence branch, the undulator has an offset Δs from the centre of the straight section. We have decided to optimise the β_x, β_y at the waist(s_w) and calculate the Twiss parameters at the insertion device position according to:

$$\begin{aligned} \beta_{x,y}(s_w + \Delta s) &= \beta_{x,y}(s_w) + \frac{\Delta s^2}{\beta_x(s_w)} \\ \alpha_{x,y}(s_w + \Delta s) &= -\frac{\Delta s}{\beta_{x,y}(s_w)} \end{aligned} \tag{3.1}$$

The first study is to show the effect of accelerator optics only on the beam spot at the sample. Assume the beamline parameters are set to the baseline values, to see how variations of the optics will translate into variations on the beam spot from the baseline beamline. Fig. 3.6 shows the fronts of this optimisation. The fronts gradually densely populate to the Pareto front, while the spot size reduces by just 1μm in the horizontal plane, and by 0.1μm in the vertical plane. Table. 3.4 lists the comparison of Twiss parameters and beam size before and after optimisation, which suggests the impact of Twiss variation in the I13 coherence branch is marginal.

	β_{xw}(m)	β_{yw}(m)	η_x	η'_x	$\sigma_x(\mu$m)	$\sigma_y(\mu$m)
Baseline	8.36	4.40	0.00	0.00	17.94	10.27
Optimised	7.00	4.00	0.00	0.00	16.44	10.22

Table 3.4: Effect of Twiss variation on the baseline beamline.

For the above study, to show the effect of the Twiss parameters on the beam spot, we have defined a selectable range of variables under appropriate circumstances. In a realistic case, the choice of Twiss parameters is strictly constrained by the particle

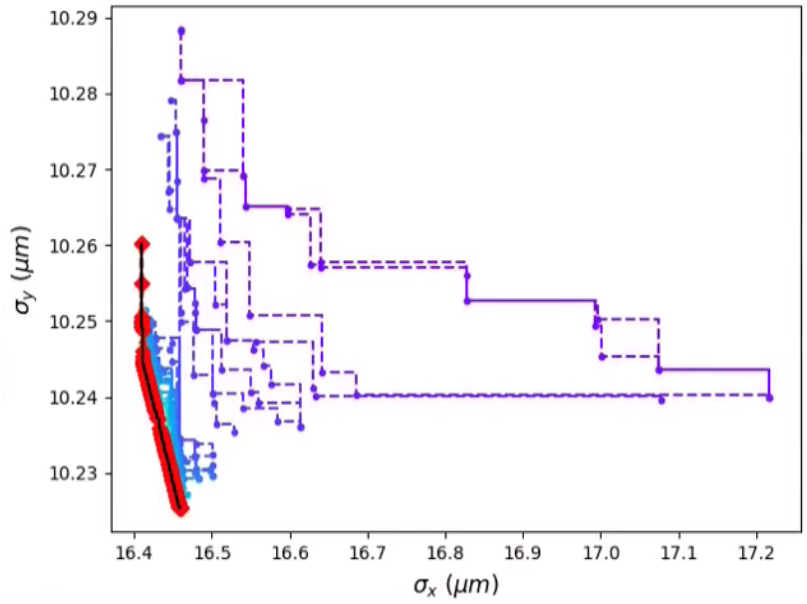

Figure 3.6: I13 Twiss optimisation from the baseline system. Different colours and line types (dashed line and solid line) represent different fronts, the dots on the fronts correspond to the solutions. The black line with red dots is the last generation.

accelerator lattice and crucially affects the non-linear dynamics. This will be explored in future work.

Now we consider a case where both the accelerator optics and the beamline parameters are allowed to be optimised. In previous section, we studied two cases: the first case considered an empirically designed beamline as a starting set-up, another case took an altered configuration of the beamline, producing a significantly inadequate beam spot at the sample (the so called "random" beamline). For the following study in this section, we will take these two cases into account.

	d_1(m)	d_2(m)	d_3(m)	p_1(m)	q_1(m)	p_2(m)	q_2(m)	β_{xw}	β_{yw}	η_{xw}	η'_{xw}	$\sigma_x(\mu m)$	$\sigma_y(\mu m)$
Start	10.00	2.20	5.50	30.90	9.10	33.10	6.90	8.36	4.40	0.00	0.00	17.94	10.27
End	12.99	1.24	5.41	29.37	8.56	31.68	6.33	8.99	4.00	0.00	0.00	3.46	1.96

Table 3.5: Optimisation of a full system starting from the baseline.

Tables 3.5 and 3.6 illustrate the results of the genetic algorithm in the two cases. Fig. 3.7 and Fig. 3.8 show the fronts converging to a smooth envelope in two cases respectively. The right figures show the beam spot picked from one of the solutions in

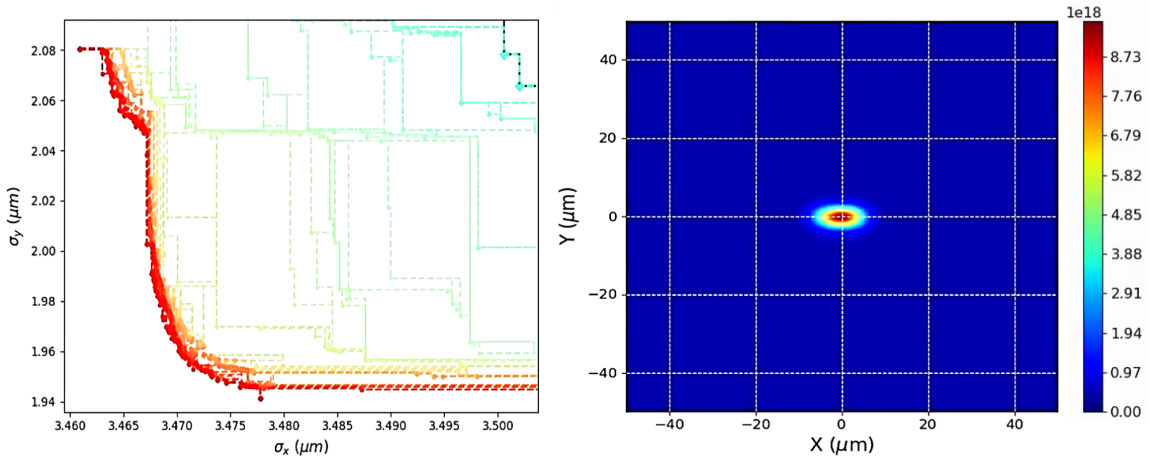

Figure 3.7: I13 Twiss and beamline optimisation from the baseline system. Different colours and line types (dashed line and solid line) represent different fronts, the dots on the fronts correspond to the solutions.

the Pareto front. It can be noted that the objective functions σ_x and σ_y converge to values that are essentially similar in both cases, (3.46, 1.96) μm and (3.57, 2.04) μm respectively. More interestingly, the behaviour of the Twiss components remarkably show that they converge towards the same waist values of the betatron function, that is (β_{xw}, β_{yw})= (8.99, 4.00)m. In the above optimisations with Twiss parameters, the optimisation range for β_{yw} are all constrained from 4m to 6m, which might be the reason that three optimisations all converge to the same β_{yw}. More explorations with wider boundaries are worth to test in future.

	d1	d2	d3	p1	q1	p2	q2	β_{xw}	β_{yw}	η_{xw}	η'_{xw}	$\sigma_x(\mu\text{m})$	$\sigma_y(\mu\text{m})$
Start	11.87	1.62	6.17	29.05	6.05	31.00	10.52	7.67	5.24	0.00	0.00	65.91	65.88
End	12.97	1.37	5.57	30.62	8.94	32.86	6.50	8.99	4.00	0.00	0.00	3.57	2.04

Table 3.6: Optimisation of a full system starting from a random system.

Similarly, the Pareto-values obtained for the beamline-components of the parameter space converge to values that are very close to each other, although not completely identical. This type of convergence to neighbouring values is common in many iterative optimisation methods used in X-ray image reconstruction.

Now, comparing the final parameters, we see that, for the baseline and random

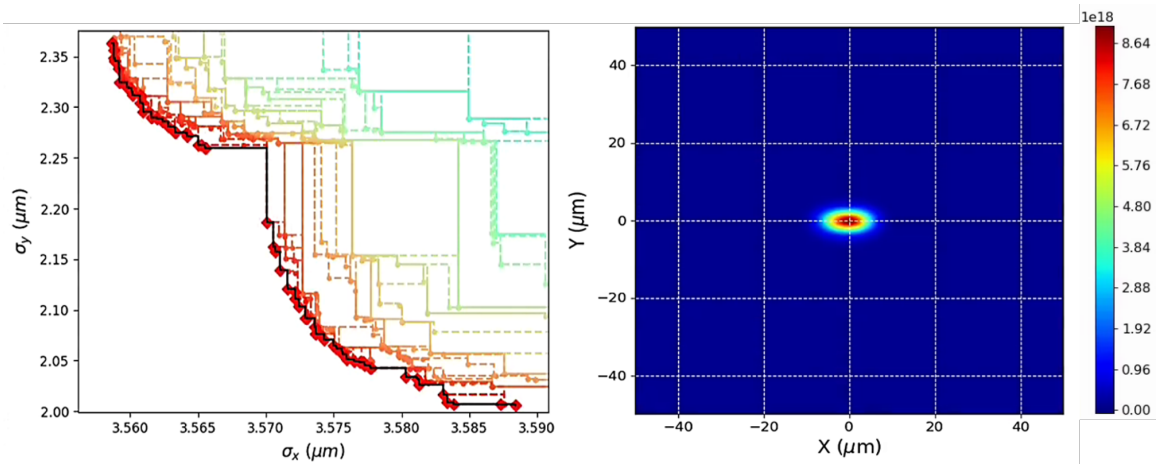

Figure 3.8: I13 Twiss and beamline optimisation from the "random" configuration. Different colours and line types (dashed line and solid line) represent different fronts, the dots on the fronts correspond to the solutions. The black line with red dots is the last generation.

cases, d_1 converges to 12.99 and 12.97, to 1.24 and 1.37, and d_2 to 5.41 and 5.57. This gives an overall length of 19.64 and 19.91. One should bear in mind that the original length for $d_1 + d_2 + d_3$ was 17.7, which means that both optimisations require an increase of the overall length by about two. This could imply practical restrictions: if the optimisation is explored on an already-built system, space could be limited; if however the optimisation is carried at the design stage, it is easier to take the desired additional space into consideration.

3.1.4 Partially coherent simulation of I13

In the current 3rd and 4th generation SR sources, due to the low emittance, partially or nearly fully coherent X-ray beamlines are designed [73]. As described at the beginning of section 2.2.1 the I13 coherence branch is designed to utilize a highly coherent beam, and with the significant reduction in emittance foreseen at Diamond II, partially-coherent wavefront propagation calculations will be needed during the design of such beamlines [74].

This type of simulation is based on the framework of classical electrodynamics and

emission by relativistic electrons as described in Section 2.1.4. To have an accurate description of the radiation, more characteristics are needed, in particular the initial horizontal, vertical, longitudinal coordinates, horizontal and vertical angles and energy. In SRW, this works by setting "macro-electrons" with different locations in the 6D phase-space, then propagating the wavefronts produced by these electrons separately through the beamline optics and eventually summing together the wavefront fields [83]. More details can be found in Chapter 2.1.

In order to extend the optimisation tools to partially coherent simulations, partially coherent synchrotron emission has been implemented in E2S. Parallel processing calculation is available in SRW to simulate the emission and propagation of electric fields from individual macro-electrons. Fig .3.9 shows the partially coherent simulation for the I13 coherence branch with $1K$ macro electrons (left), $5K$ macro electrons (middle) and $10K$ macro electrons (right) respectively. In the left figure, we can roughly see the beam intensity distribution and outline of the beam spot, however the edges are uneven. With an increased number of macro electrons, the distribution gets clearer and the spot becomes smoother.

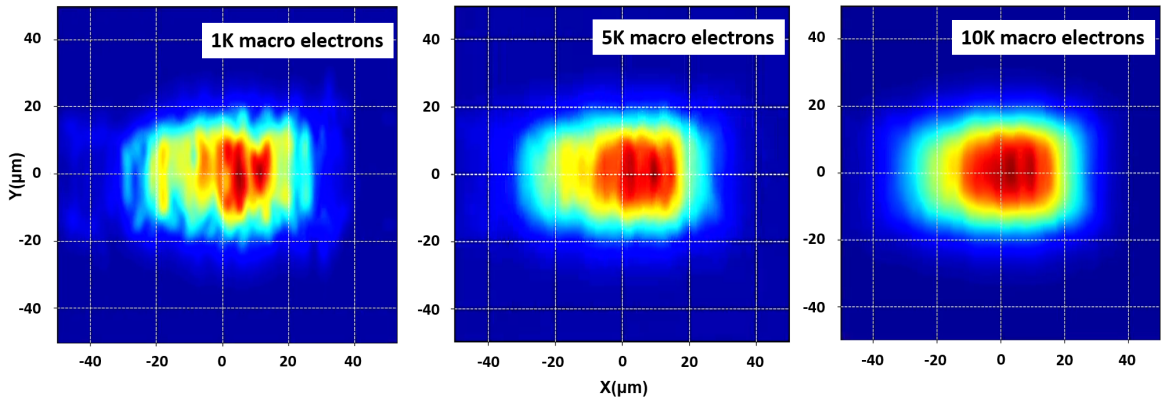

Figure 3.9: Partially coherent simulation with $1k$ macro electrons (left), $5k$ macro electrons (middle) and $10k$ macro electrons (right).

In Fig. 3.10 we compare the $10k$ macro electrons partially coherent simulation with multi-electron simulation in SRW. It is clear to see that the two photon beam sizes and shapes are roughly the same (σ_x= 17.94 μm, σ_y= 10.27 μm for multi-electron simulation, σ_x= 17.42 μm, σ_y= 11.68 μm for partially coherent simulation).

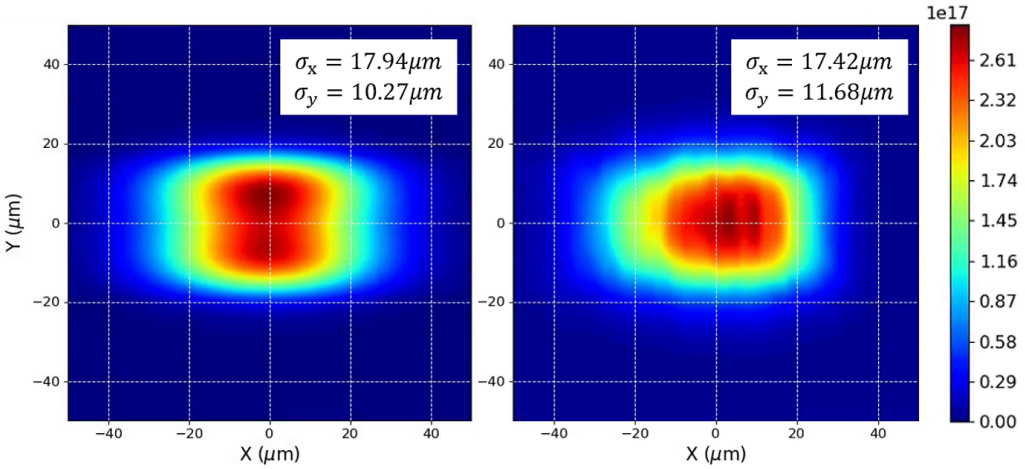

Figure 3.10: Multi-electron simulation (left) and partially coherent simulation (right) of the I13 coherence branch at sample position.

In section 3.1.1 the optimisation of the I13 coherence branch in 2D and 7D was shown. Now, the optimised beamline configuration is used to check if this optimisation could work on the partially coherent simulation. Fig. 3.11 shows the comparison of the multi-electron and partially coherent simulations of the optimised I13 coherence branch at the sample position. The photon beam size of the partially coherent simulation (σ_x= 4.58 μm, σ_y= 3.88 μm) is obviously larger than multi-electron simulation (σ_x= 3.27 μm, σ_y= 1.88 μm). Nevertheless, it is clear that the size of the photon beam is significantly reduced (from σ_x= 17.42 μm, σ_y= 11.68 μm to σ_x= 4.58 μm, σ_y= 3.88 μm) based on the optimised configuration, which means that one can perform a fast optimisation on a multi-electron case, then apply the result to the partially coherent system.

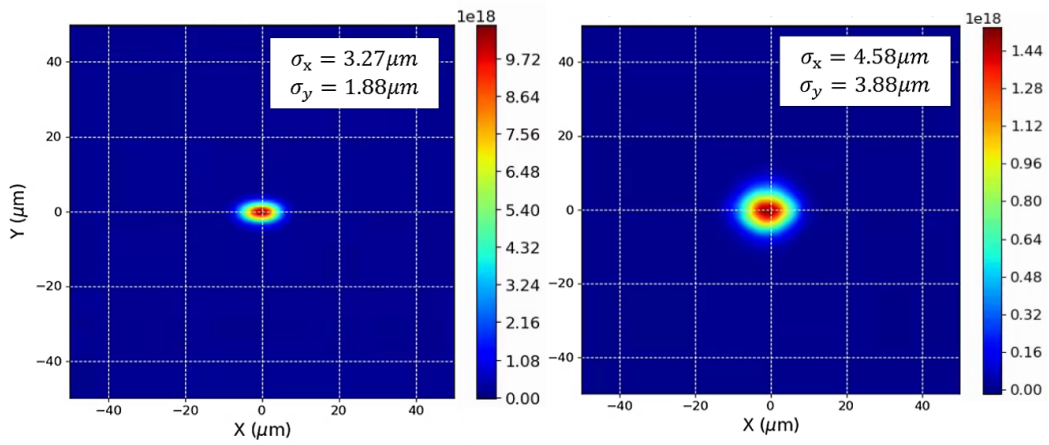

Figure 3.11: Multi-electron simlation (left) and partially coherent coherent simulation (right) of the optimised I13 coherence branch at sample position.

3.2 Wiggler beamline optimisation

Another beamline we are going to optimise is the I20 Scanning branch [84], which is based on a wiggler source. This optimisation is achieved by the following steps: (1) the Response Matrix [85] method is used in E2S to see if we can optimise the beamline in a linear way. (2) We are going to optimise the beamline in two cases, one is optimising with a subset of the beamline variables only, another one is extending the parameter space with source parameters. (3) After the optimisation, we will identify the feasibility of the optimised solution.

3.2.1 Beamline I20

Beamline I20 in Diamond is equipped with two wigglers in the same straight section, one is for the scanning branch (I20-Scanning), and the other is for the dispersive branch (I20-EDE). The two beamlines are operated independently and simultaneously. The scanning branch offers monochromatic X-rays with high flux and high spectral purity in energy resolution [86]. We did this study with the scanning branch, whose layout is shown in Fig. 3.12. The insertion device for the I20 scanning branch is a 1.95m hybrid wiggler with 83mm period. Table. 3.7 shows the Twiss parameter

we will use for the simulation.

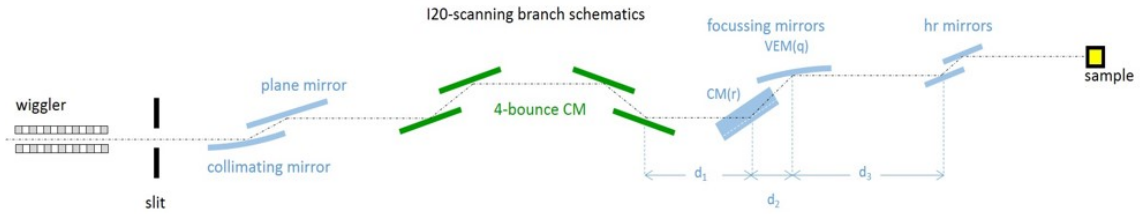

Figure 3.12: A schematic top view of the DLS beamline I20 scanning branch model used in this study.

β_x(m)	β_y(m)	α_x	α_y	η_x(m)	$\delta E'(\%)$
4.97	1.49	-0.24	0.00	0.07	0.0959

Table 3.7: Twiss parameters of the I20 scanning branch

The beamline starts from a primary slit ($14mm \times 2.1mm$), which defines the size of the beam to be used. Then a pair of vertical deflecting mirrors operate at 2.3 mrad incident angle to collimate the vertical beam plane [86]. Since the beam from the wiggler source has large divergence, this design can maximise the flux through the monochromator. Next is the heart of this beamline, a four bounce monochromator [87]. The monochromator consists of two pairs of counter-rotating crystals which provide a truly fixed exit for the monochromatic radiation by countering the rotation of two primary rotation axes [86]. A particular advantage of this monochromator is that the energy resolution is independent of the incident beam divergence. This is important for the absorption measurements made on inhomogeneous samples [86]. After the monochromator, a spherical mirror and an elliptical mirror are used to focus the horizontal and vertical plane respectively. The last optical element in this beamline is a pair of harmonic rejection mirrors located about 4m before the sample.

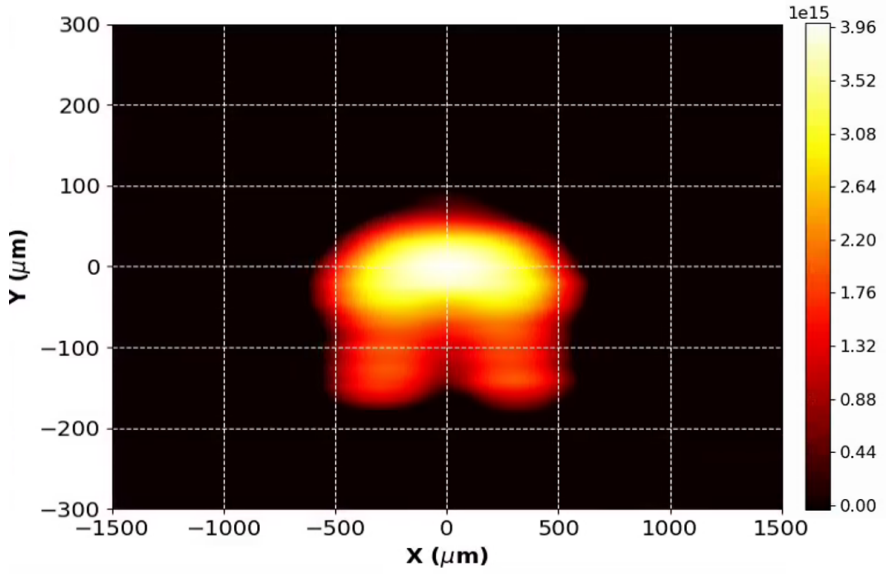

Figure 3.13: Beam spot at the sample of the I20 scanning branch from E2S. Two winged lobes are observed due to the spherical mirror aberration.

A particular challenge of the photon behaviour of this beamline at the sample position is that spherical aberrations are observed because of the concave spherical mirror (CM(r) in Fig. 3.12) [88]. It exhibits two tails as shown in Fig. 3.13, which is not not desirable. This complicates considerably the post-processing of results and data analysis.

To optimise the beam spot, two studies were conducted to explore the effect of the modification of beamline parameters on the beam spot characterizing the system.

3.2.2 Response Matrix to optimise the I20 scanning branch

Response Matrices are commonly used in accelerator physics to optimise the machine optics [89]. In a similar way, this method was applied to see if the performance of a beamline could be improved. In doing this we make the implicit assumption that the system is linear, at least within a certain domain around a defined working point. Small modifications of the parameters defining the beamline allow the calculation of a Beamline Response Matrix (BRM) which can then be used to improve the perfor-

mance of the beamline itself.

The BRM technique was studied for the beamline I20 scanning branch where the used parameters were the five elements following the last crystal in the monochromators along the beamline, i.e. the first drift afterward (d_1), the sagittal radius of the following spherical mirror (CM(r)), the length of the drift after it (d_2), the focal length of the vertically deflecting mirror (q) and the subsequent drift (d_3). Starting from the baseline configuration we recorded the beam size variations corresponding to a 1% change in the parameters, thus building the BRM for I20. A pseudo-inverted matrix is then obtained by standard singular value decomposition (SVD) [90] which can be used to infer the parameter variations needed to produce the requested variations of the objectives.

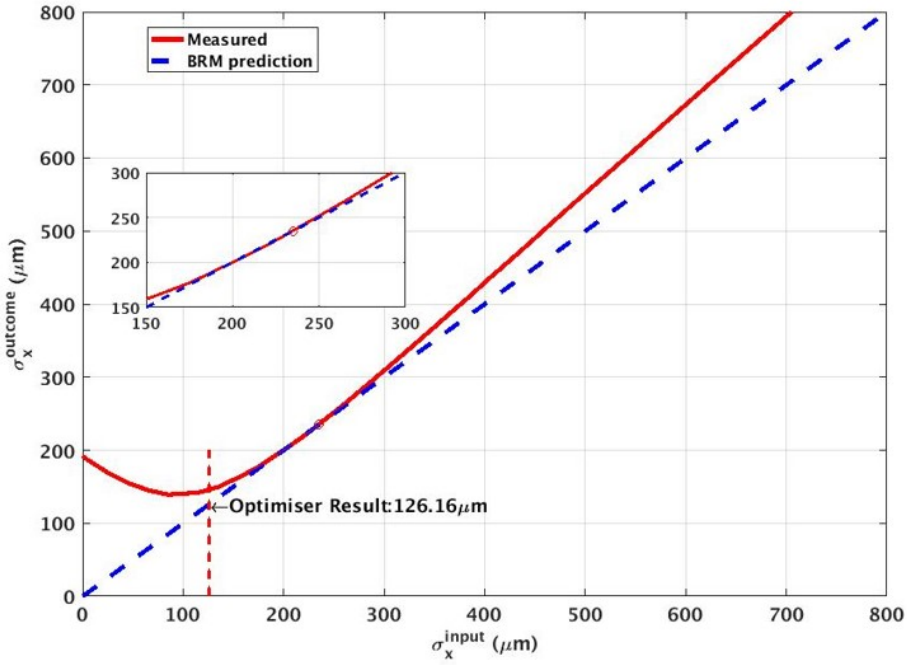

Figure 3.14: Response matrix optimisation results for present I20 beamline. The red line represents the measured beam size with respect to the requested beam size. The dashed blue line is a linear prediction. The red dot is positioned at the initial beam size $\sigma_x = 245$um.

Fig. 3.14 illustrates the real variations with respect to a baseline configuration

seen in the beamline for a requested change in a parameter (red line). The starting point is from the initial beam size $\sigma_x = 245\mu m$. This result can be compared with the simple linear prediction (dashed blue line). It is apparent how the linear response of the system is satisfied only for a close region around the working point (see inset of Fig. 3.14). For large requested variations linearity is broken, in particularly a negative change may conflict with the focusing nature of the system (beam size is positive defined), as clearly seen in Fig. 3.14 where a quadratic behaviour appears around a minimum.

This discrepancy is exacerbated if starting from an initially bad beamline configuration. Considering a deliberately random beamline, we tried to reduce an initial beam spot at the sample with $\sigma_x = 10.4$mm by using a BRM computed around this working point. The non-linearity case is even stronger, as seen in Fig. 3.15, and we cannot get a spot smaller than 3mm at the sample.

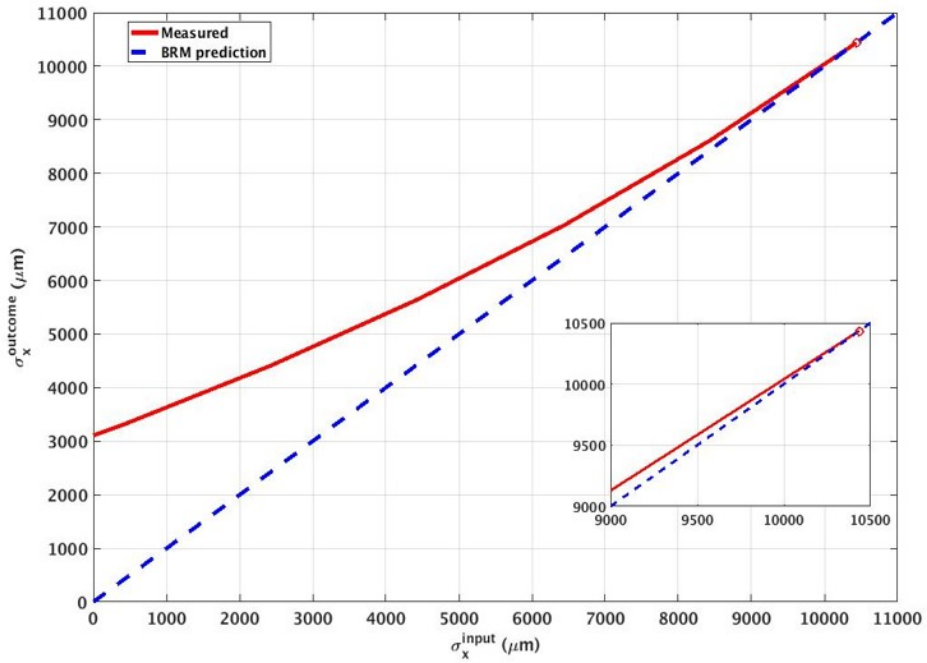

Figure 3.15: Response matrix optimisation for a spoiled configuration of I20 where σ_x was inflated to 10.4mm.

From this study we see that a response matrix based approach is very fast, but is required to be fairly close to the best solution. If this is not the case, the often intrinsic non-linearity of the problem may lead to bad or even non-physical solutions.

3.2.3 E2S optimiser applied to I20 scanning branch

Section 3.1 showed that the E2S optimiser could work well on the undulator beamline I13 coherence branch to improve the beamline performance. From the last section, we see there are limitations to optimise the I20 scanning branch by means of a Beamline Response Matrix. Therefore, in order to have a more reliable optimisation, the E2S optimiser will be applied to the I20 scanning branch.

3.2.3.1 Beamline optimisation

As in the studies done so far we focused on reducing the size of the beam at the sample. Thus the objectives are σ_x and σ_y. The parameters used were the five elements mentioned in the BRM method: d_1, CM(r), d_2, q, d_3 (Fig. 3.12).

The optimisation was running for 30 generations each having a population of 100 individuals calculated in parallel on a cluster. This beamline configuration is computationally much more intensive due to the time required in SRW to calculate the initial wave-front from a wiggler. To speed up the simulation, we record the wavefront at the entrance of beamline as the initial wavefront. Therefore in the optimisation, the initial wavefront will be extracted directly then propagated through the beamline. By separating the initial front production from its propagation we can speed up the simulation by about a factor of ten.

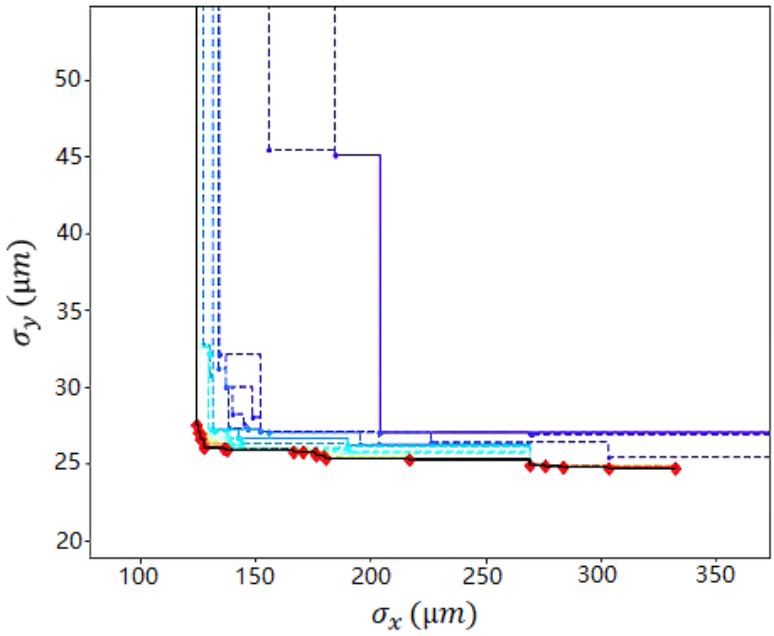

Figure 3.16: Optimisation fronts of beamline I20 scanning branch. Different colours and line types (dashed line and solid line) represent different fronts, the dots on the fronts correspond to the solutions. The black line with red dots is the last generation.

Table. 3.8 shows that as the number of computed generations increases, the horizontal and vertical beam sizes become more confined at the sample position. After 30 generations, the fronts converge to a smooth envelope, and the final configuration is picked from the Pareto front shown in Fig. 3.16.

	d_1(m)	Radius(m)	d_2(m)	VEM-q(m)	d_3(m)	σ_x(μm)	σ_y(μm)	I(flux/mm^2)
Baseline	2.70	0.087	4.50	23.00	19.50	235.50	44.26	3.97e+15
Generation 25	2.32	0.084	5.23	21.32	18.11	173.17	32.34	7.52e+15
Generation 30	3.75	0.084	4.05	21.01	18.14	147.51	26.46	8.43e+15

Table 3.8: Optimisation of I20 scanning branch beamline parameters.

The Fig. 3.17 shows the baseline configuration (left) and the optimised one (right) respectively. As can be seen by comparing the two beam-spots, the two tails have been removed successfully, the resulting beam size is nearly halved and therefore the intensity is increased by more than a factor of two.

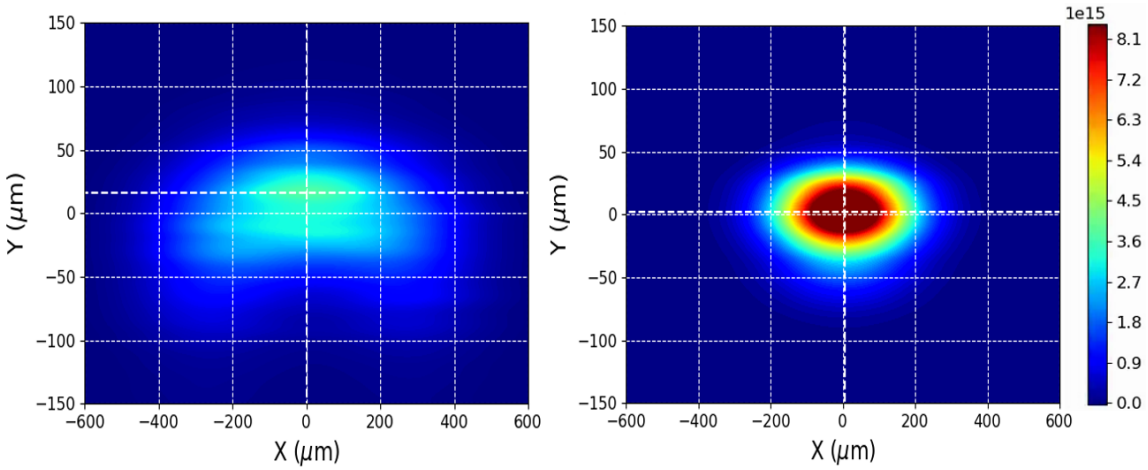

Figure 3.17: (Left) beamspot at sample for beamline I20-scanning branch for the baseline configuration of the system. (Right) image at sample after 30 generations of the genetic optimiser. To visualise the effect of intensity, we have fixed the colorbar range with the peak intensity of the optimised beam.

3.2.3.2 Beamline optimisation with source parameters

In section 3.1.3 we illustrated that the contribution of Twiss parameters in the optimisation of the I13 coherence branch is marginal. While for the I20 scanning branch, the main optimisation target is to eliminate the aberration from the spherical mirror, this effect is highly depending on the incident beam angle and position. Therefore we studied the optimisation of the beamline with the effect of the Twiss parameters to see if we can improve the beam performance of the I20 scanning branch.

In the case of I20, the wiggler has an offset Δs of 0.054m from the center of the straight section. The same method is used as in Section 3.1.3 to optimise β_x, β_y at the waist(s_w) and calculate the Twiss parameters at the source position according to Eq. 3.1. This time the generation of SR cannot be separated from its propagation because of the Twiss parameters, hence the source definition is a part of the optimisation process. Considering the CPU time consumption in simulation with the wiggler source, the optimisation starts from the initial beamline configuration and the optimised beamline in the beamline parameters optimisation. This time the optimiser

runs for 50 generations and 100 populations.

	d_1(m)	Radius(m)	d_2(m)	VEM-q(m)	d_3(m)	β_{xw}(m)	β_{yw}(m)	η_x	η'_x	σ_x (μm)	σ_y (μm)	I(flux/mm^2)
Baseline	2.70	0.087	4.50	23.00	19.50	4.97	1.49	0.07	0.00	235.50	44.26	3.97e+15
BL	3.75	0.084	4.05	21.01	18.14	4.97	1.49	0.07	0.00	147.51	21.46	8.43e+15
Twiss+BL	3.81	0.084	4.55	20.18	17.35	2.18	1.82	0.00	0.00	73.03	25.70	1.85e+16

Table 3.9: Optimisation of the I20 scanning branch full system (Twiss+beamline).

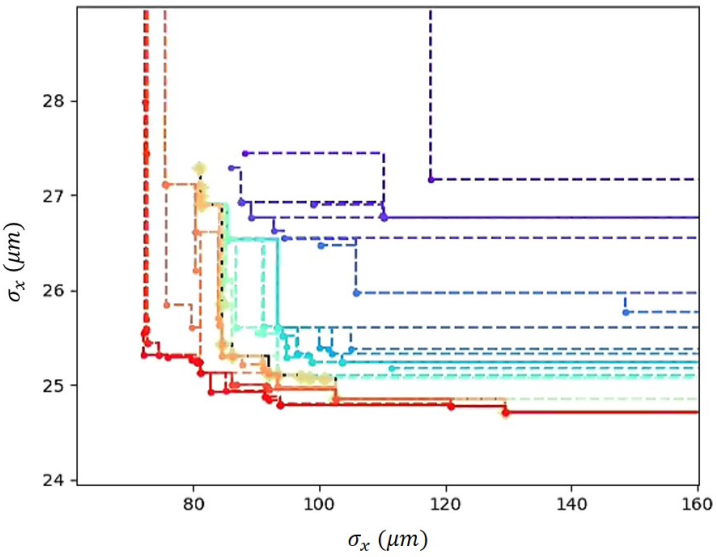

Figure 3.18: Twiss and beamline optimisation fronts. Different colours and line types (dashed line and solid line) represent different fronts, the dots on the fronts correspond to the solutions. The red solid line is the last generation.

Table.3.9 illustrates the results of the genetic algorithm in the beamline optimisation in two cases. Fig. 3.18 shows a part of the fronts map where most of the fronts are located. We can see that the vertical beam size σ_y did not improve too much, in the range from 28 μm to 24.7 μm, which implies that the setting of the Twiss and beamline parameters has already helped the system find a local minimum of σ_y. On the other hand, the horizontal beam size shows the potential for further optimisation, from 275 μm to 73 μm. This illustrates one of the advantages of NSGA optimisation, even though the two objectives are dependent, it is still possible to fix one objective then optimise the second.

Fig. 3.19 (left) shows the beam spot in the baseline configuration which is the same

as Fig. 3.13. Fig. 3.19 (centre) is the beam spot after beamline (BL) optimisation and (right) after Twiss+BL optimisation respectively. We see that the beam size shrank significantly, and as a result, the peak intensity quadrupled after the Twiss +BL optimisation.

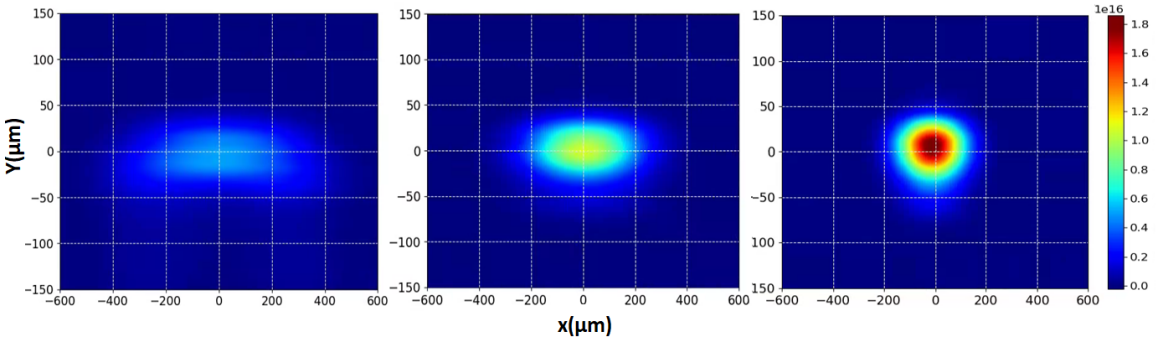

Figure 3.19: Beam spot at the sample of the I20 scanning branch with baseline configuration as Fig. 3.13 (left), BL optimisation result (centre), Twiss + BL optimisation result (right).

Compared to the optimised beamline configurations of the two optimisations (see Table 3.9), d_1 converges to 3.75m and 3.81m, d_2 changes to 4.05m and 4.55m, and d_3 reduces to 18.14m and 17.35m. This gives overall lengths for $d_1 + d_2 + d_3$ equal to 25.94m and 25.71m in the two cases. The radius of the spherical mirror, which is the most sensitive parameter in these two optimisations to determine the beam shape, reaches the same value. The original length for $d_1 + d_2 + d_3$ is 26.70 m, which means for both optimisation, no matter how the source changes, the total length reduces by 1m and keep the spherical radius at 8.40cm is the best configuration for this beamline.

3.3 Summary of this chapter

In this chapter, the optimisations of an undulator beamline (Diamond I13 coherence branch) and a wiggler beamline (Diamond I20 scanning branch) with the E2S-SRW optimiser were presented. The optimisations were mainly executed in two steps: first,

the beamline was optimised with a subset of beamline variables only. We also showed the effect of extending the parameter space on beamline optimisation. Then in the second step, the photon source parameters were taken into account to optimise a beamline (Twiss+BL optimisation).

The study of using a beamline response matrix to optimise a beamline shows that the E2S optimiser is a better choice to give a more reliable beamline optimisation. The E2S-SRW optimiser worked well for both beamlines. The photon beam size at the sample of the optimised beamline was smaller than the baseline configuration by a factor of two, therefore the greater intensity was gained at the sample. The weird photon beam shape of the I20 scanning branch was also eliminated.

A simulation benchmark for the multi-electron mode and partially coherent mode was done to show that we can perform a fast optimisation on a multi-electron case then apply the result to a partially coherent system.

Chapter 4

Ray tracing based optimisation of beamlines

Geometrical ray-tracing codes have been commonly used by the synchrotron radiation facilities for X-ray optics design and beamline optimisations [75]. SHADOW is one of the most popular ray-tracing tools developed for this purpose. The simulation theory of SHADOW has been described in Chapter 2. E2S-SHADOW optimiser is developed based on the SHADOW3 [91] and NSGA II to optimise a beamline where photons are assumed to propagate through the optical elements according to a ray-tracing model. In this chapter, we present the optimisations of beamline I13 coherence branch and I20 scanning branch in Diamond by using E2S-SHADOW optimiser. A comparison of E2S-SRW optimiser and E2S-SHADOW optimiser will be discussed. Some SHADOW simulations for Diamond II wiggler sources will also be presented.

4.1 Beamline optimisations by using ray-tracing based optimiser

4.1.1 Undulator beamline optimisation

The undulator beamline we have optimised is the I13 coherence branch in Diamond. A detailed description of this beamline can be found in 2.2.1. The source in this simulation is an undulator with period 25mm and K is 1.87, Table. 4.1 shows the source parameters used to define the I13 coherence branch photon source in SHADOW.

Size RMS H(μm)	Size RMS V(μm)	Divergence RMS H(μrad)	Divergence RMS V(μrad)
31.97	5.58	3.72	1.15
Undulator length(m)	Undulator energy(eV)	Number of rays	Delta energy(eV)
2.71	11209	100000	1

Table 4.1: Source parameters for I13 coherence branch simulation in SHADOW. The source is defined by the horizontal (H) and vertical (V) Root Mean Square (RMS) sizes, divergences and undulator parameters.

The beam spots at the sample position for the baseline beamline setup calculated by SHADOW and SRW are shown in Fig. 4.1. The beam size calculated from SHADOW is $(\sigma_x, \sigma_y) = (17.83\mu m, 9.42\mu m)$ which shows good agreement with the beam size calculated by SRW $(\sigma_x, \sigma_y) = (17.94\mu m, 10.27\mu m)$.

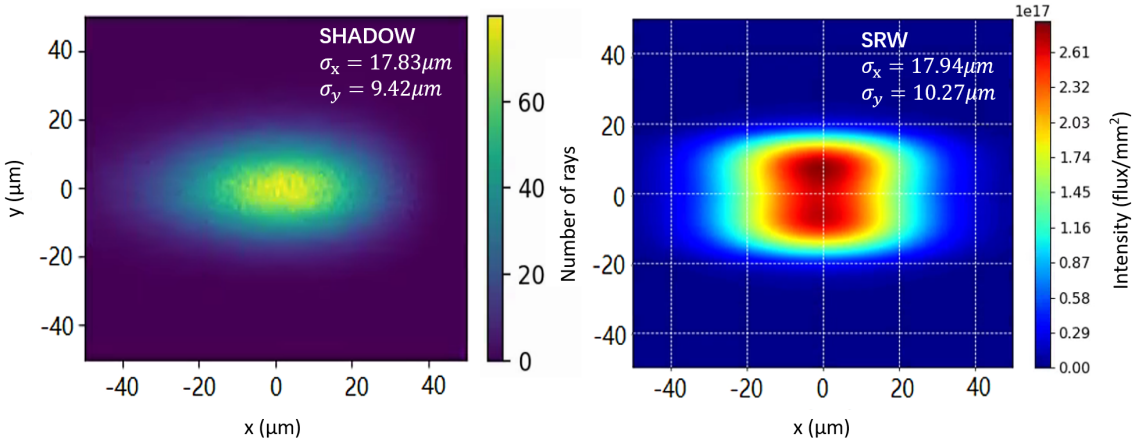

Figure 4.1: Beam spot at sample of I13 coherence branch with baseline configuration calculated by SHADOW (left) and SRW (right).

We notice that the two beam spots in Fig. 4.1 look different in the vertical plane, so the Full Width at Half Maximum for beam spots in the vertical plane are calculated: 22.18μm for the SHADOW result, 27.54μm for the beam spot calculated from SRW. This 5.4μm discrepancy cause the visual difference. In our SRW simulations, the beam size is calculated from the standard deviation σ [92]. While in SHADOW, the beam is treated as Gaussian distribution, so the beam size is evaluated by Full Width at Half Maximum directly. Therefore, for the following SHADOW optimisations, the objectives will be the Full Width at Half Maximum in two planes.

After modelling the beamline in SHADOW, we optimise the beamline with the E2S-SHADOW optimiser. A subset of the beamline variables is selected for the optimisation; these are the same parameters used in the 7D optimisation with E2S-SRW optimiser: the drift between the last crystal monochromator and the first elliptical mirror (d_1), the drift between the last two elliptical mirrors of the KB system (d_2), the drift from the last elliptical mirror to the sample (d_3) and the two focal distances of each elliptical mirror of the KB system (p_1, q_1, p_2, q_2). The objectives of this optimisation are the Full Width at Half Maximum of the horizontal (fwhmx) and vertical (fwhmy) beam sizes. This sets up the multi-objective problem in a 7-dimensional parameter space. The computation of the genetic algorithm runs on a population of 100 individuals and over 50 generations. Fig. 4.2 shows the convergence of fronts produced by the E2S-SHADOW optimisation.

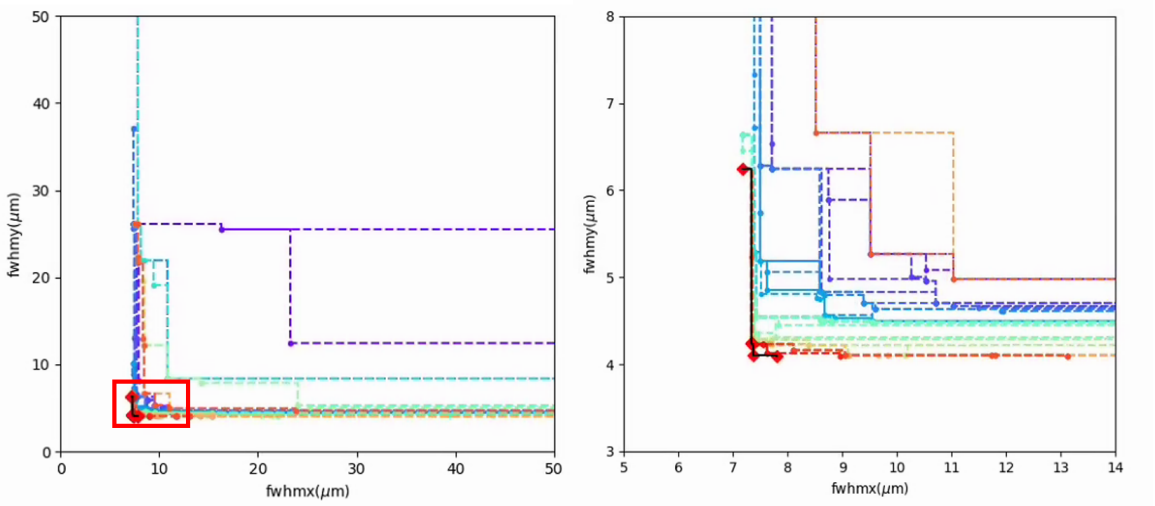

Figure 4.2: Left: Optimisation fronts of beamline I13 coherence branch calculated with the E2S-SHADOW optimiser. Right: zoom-in of red rectangle part in the left figure. Different colours and line types (dashed line and solid line) represent different fronts, the dots on the fronts correspond to the solutions. The black line with red dots is the last generation.

The results presented in Table. 4.2 illustrate the working process of the optimiser. The horizontal and vertical beam sizes become localised to the sample position as the number of computed generations increases. After eight generations, we can already see the improvement in both planes. Fig. 4.2 (right) gives a zoom-in of the Pareto front close to the solutions of interest. It is clear that even though the vertical beam size has been almost fixed in this area, the horizontal beam size can still be optimised.

	d_1(m)	d_2(m)	d_3(m)	p_1(m)	q_1(m)	p_2(m)	q_2(m)	$\sigma_x(\mu$m)	$\sigma_y(\mu$m)
baseline	10.00	2.20	5.50	30.90	9.10	33.10	6.90	17.83	9.42
Generation 8	5.71	1.59	5.11	34.23	9.26	28.02	5.79	4.67	2.12
Generation 38	12.11	1.62	5.56	33.25	9.07	28.47	6.47	3.73	1.91
Generation 50	13.18	1.56	5.19	25.37	9.06	34.04	5.93	3.31	1.74

Table 4.2: Parameters used for the 7D genetic optimisation with E2S-SHADOW optimiser and the values reached by the objectives during the NGSA evolution.

The next step is to compare the result of this optimisation with the previous E2S-SRW 7D optimisation. Fig. 4.3 presents the beam spots after the E2S-SHADOW optimisation (left) and E2S-SRW optimisation (right) respectively.

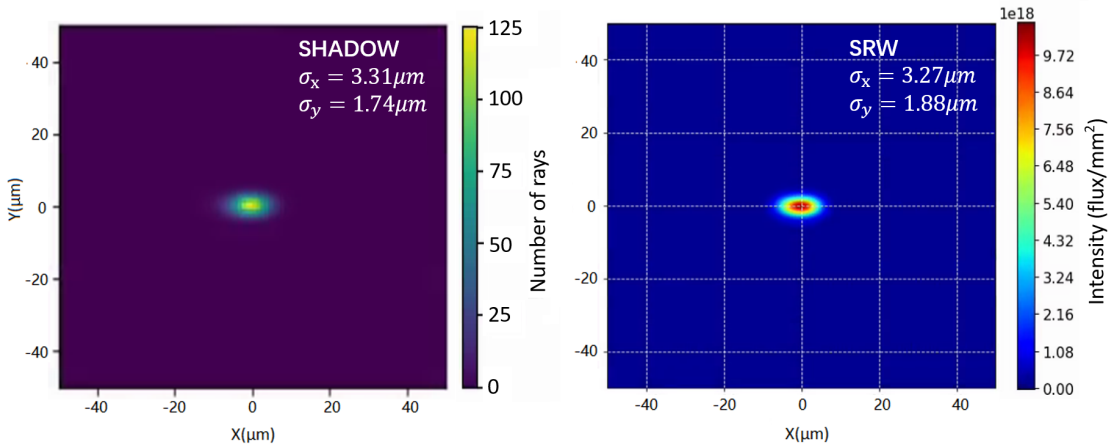

Figure 4.3: Beam spot at the sample position after E2S-SHADOW optimisation (left) and E2S-SRW optimisation (right).

Table. 4.3 lists the variables of the optimal solution and the corresponding beam size for the two optimisations. The beam spot sizes at the sample after the two optimisations are very close to each other, $(\sigma_x, \sigma_y) = (3.31\mu m, 1.74\mu m)$ for the E2S-SHADOW optimisation, $(\sigma_x, \sigma_y) = (3.27\mu m, 1.88\mu m)$ for the E2S-SRW optimisation.

	d_1(m)	d_2(m)	d_3(m)	p_1(m)	q_1(m)	p_2(m)	q_2(m)	$\sigma_x(\mu m)$	$\sigma_y(\mu m)$
E2S-SHADOW	13.18	1.56	5.19	25.37	9.06	34.04	5.93	3.31	1.74
E2S-SRW	11.09	1.33	5.00	30.65	7.93	32.50	5.74	3.27	1.88

Table 4.3: Beamline optimisation results with the E2S-SHADOW and E2S-SRW optimisers.

Therefore, for the I13 coherence branch, both optimisers can work in a pretty equivalent way improving the beam spot to the finest size $\sigma_x \approx 3.30\mu m, \sigma_y \approx 1.80\mu m$ at the sample position. No significant differences were observed between SRW and SHADOW in the I13 coherent branch simulations.

4.1.2 Wiggler beamline optimisation

As an example of optimisation of a wiggler source, we considered the I20 scanning branch. Fig. 4.4 shows the beam spot at sample simulated by SHADOW before any optimisation, the photon beam energy used is 8700 eV. The wiggler source parameters

used in this simulation are presented in Table. 4.4.

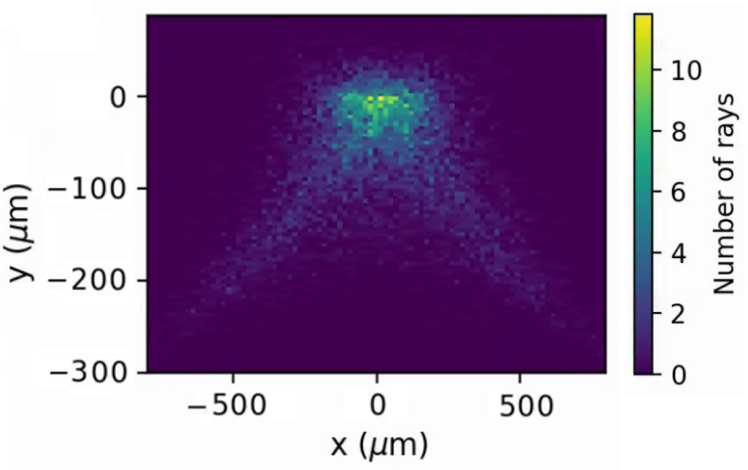

Figure 4.4: Beam spot at the sample position simulated by SHADOW

$\sigma_x(\mu m)$	$\sigma_y(\mu m)$	ϵ_x (rad.m)	ϵ_y(rad.m)
121.62	3.56	2.7e-9	8e-12
Number of periods	K value	ID period (m)	Number of rays
24	9.303	0.083	100000

Table 4.4: Source parameters for the I20 scanning branch simulation in SHADOW. The source is defined by the horizontal (x) and vertical (y) electron beam size and emittance together with wiggler parameters.

The aforementioned ′two tails′ seen in the previous chapter become apparently more pronounced in this simulation. An optimisation was set up with five beamline variables: the first drift afterwards (d_1), the sagittal radius of the spherical that follows it (CM(r)), the length of the drift after (d_2), the focal length of the vertically deflecting mirror (q) and the drift that follows (d_3) in Fig. 3.12. Due to the special shape of the beam spot, the objectives in this optimisation are the range of the photon beam distribution in the horizontal and vertical planes. The ′full size′ refers to a measure of spread, it is the coordinate overall extent of the intensity distribution from top to bottom of the region of interest. The E2S-SHADOW optimiser runs for 100 generations with a population of 50 individuals for this optimisation.

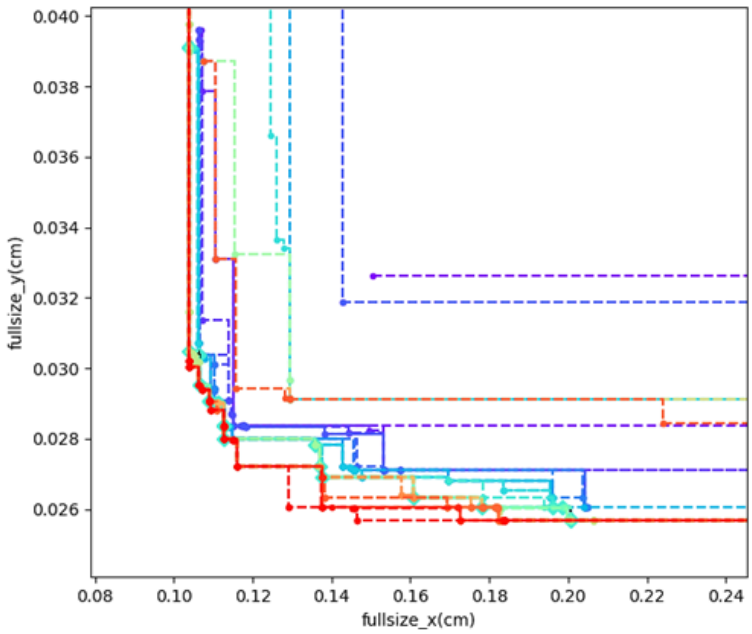

Figure 4.5: I20 scanning branch optimisation fronts simulated with the E2S-SHADOW optimiser. Different colours and line types (dashed line and solid line) represent different fronts, the dots on the fronts correspond to the solutions.

Fig. 4.5 shows the convergence of the fronts during the optimisation. The initial beam size in the horizontal and vertical planes are 1500μm and 330μm respectively. After the optimisation, we choose one of the optimal solutions at the Pareto front, the beam size in two planes are 1126μm and 279μm respectively. Table. 4.5 presents the results of the genetic algorithm in the beamline optimisation.

	d_1	Radius	d_2	VEM-q	d_3	$fullsize_x(\mu\text{m})$	$fullsize_y(\mu\text{m})$
Baseline	2.70	0.087	4.50	23.00	19.50	1500	330
Optimised	3.32	0.091	5.72	22.76	19.33	1126	279

Table 4.5: E2S-SHADOW optimisation of I20 scanning branch beamline parameters.

The improvement of beam size is marginal compared with the optimisation by the E2S-SRW optimiser. Now we check if this optimisation could eliminate the two tails.

Fig. 4.6 shows the beam spot at the sample of the I20 scanning branch with baseline configuration (left) and optimised beamline (right). The yellow dashed line

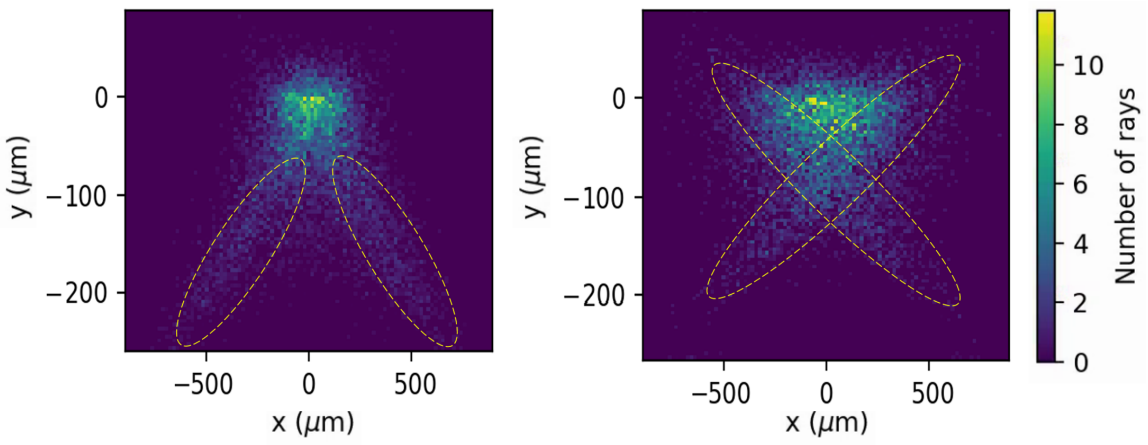

Figure 4.6: Beam spot at I20 scanning branch sample position before optimisation (left) and after optimisation by E2S-SHADOW optimiser (right). Dashed yellow lines are used to mark the two 'tails'.

is used to guide the eye around the position of the two tails. If we compare the two images in Fig. 4.6, the two tails move up and gradually cross through the centre spot during the optimisation. Therefore after optimisation, more photons concentrate in the centre but the effect of aberration (tails) still appears. A few more optimisations were done by using the E2S-SHADOW optimiser to improve the beam spot shape of the I20 scanning branch such as using more beamline parameters, increasing the population and generations. However, the aberration effect is unavoidable in all the optimisations we have tried with the E2S-SHADOW optimiser.

Another attempt was performed to optimise the beam spot at the sample of I20 scanning branch by interfacing a Python optimisation script to E2S [55]. This is a study completed by the Accelerator Physics group in Diamond [55]. A Nelder-Mead simplex optimisation [93] was used and a better set of values was found for the radius of the spherical mirror and the drift length before the sample. Two penalty functions were used to evaluate the initial photon distribution at the sample: a uniform function and a parabolic function, both zeroed outside a [-200,+200]μm interval [55]. Fig. 4.7 summarises the results.

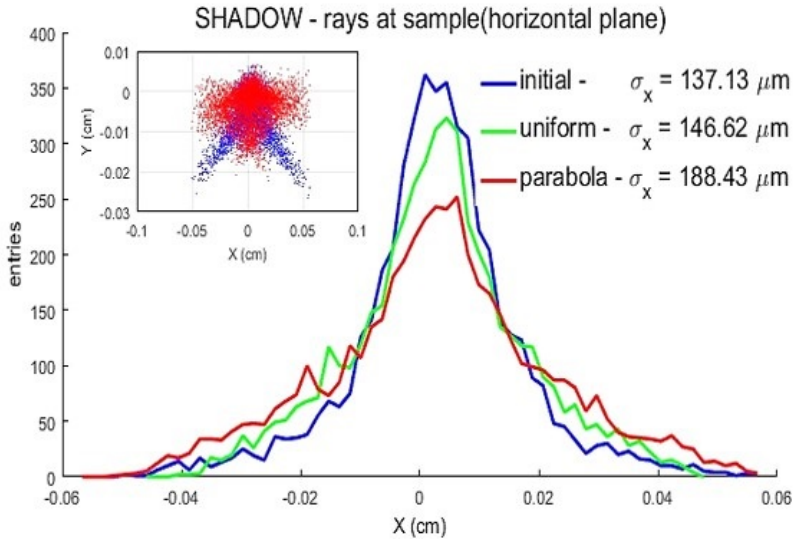

Figure 4.7: Beam spot at the sample from SHADOW ray tracing calculation for the I20-scanning branch. (Blue) initial distribution, beamline optimisation with a flat (green) and with a quadratic (red) penalty function (see text). Inset: (X, Y) beamspot at the sample for baseline configuration and chosen solution.[55]

The optimisation results show that the quality of the photon pattern related to the parabolic penalty function is improved. This improvement comes with a reduction in the photon flux inside the [-200, +200] μm window.

For both the E2S-SHADOW and Python simplex optimisations, we can still see the cross structure of tails after optimisations. This is the main difference found between SRW and SHADOW simulations; the aberration effect is more significant in the SHADOW simulations. While more extensive numerical simulations will be needed, we believe this is a first example that show how a fully numerical code can be used to improve a system rule by a complex nonlinear propagation laws of its rays, to tailor the requirement of the beamline directly at the sample.

4.2 ′Double source′ effect in Diamond II

Another example where a complicated, non Gaussian, intensity distribution appears to spoil significantly the beamline performance was found in the optimisation of the

wiggler beamlines (I12-I15-I20) for Diamond II. The properties of wiggler sources can be strongly affected by the relatively large acceptance angles and the electron trajectory. The so-called ′double source′ effect happens when the electron oscillation amplitude in the wiggler is sufficiently large compared with the electron beam size. Two separate sources can be seen at source position with transverse separation of $\pm a$ [7], where a is the wiggler amplitude defined as,

$$a = \frac{K\lambda_u}{2\pi\gamma} \tag{4.1}$$

as usual K is the deflection parameter of the insertion device, λ_u is the wiggler periodic length, γ is the Lorentz factor. The photon source size Σ_x is the convolution of several contributions which are taken into account in simulations [7]:

$$\Sigma_x^2 = \sigma_x^2 + a^2 + \frac{L^2}{12}\sigma_{x'}^2 + \frac{L^2}{36}\Theta_x^2 \tag{4.2}$$

σ_x and $\sigma_{x'}$ are the electron source size and divergence in the transverse plane, L is the wiggler length, Θ_x is the acceptance as defined in chapter 1. The effective source size of the wiggler is considered as a Gaussian, when the effect of the double source is not present. Therefore we sum the electron beam, beamline angular acceptance and the wiggler amplitude in quadrature, this approach is used in numerical simulations as well as to derive analytical approximated expressions for describing the wiggler source [94].

The electron trajectories in the current Diamond wigglers follow a sinusoidal profile with an amplitude a ≈20-30μm. In the present machine (DLS), the horizontal photon source size is dominated by the electron beam with $\sigma_x > 100\mu m$, hence the ′double source′ effect is not present. However due to the significant reduction in emittance, the ′double source′ may appear in Diamond II (D-II) wiggler beamlines. Fig. 4.8 illustrates the origin of the ′double source′.

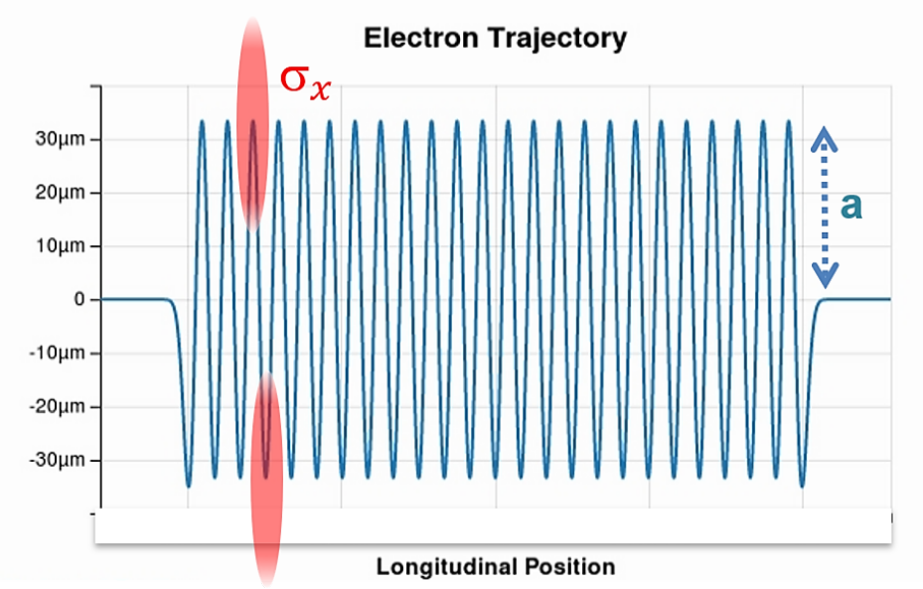

Figure 4.8: A schematic diagram to show the cause of ′double source′.

There are 4 wiggler beamlines in DLS, Table. 4.6 presents the wiggler sources information for DLS and Diamond II. The Diamond II sources are calculated with the CDR lattice where ϵ_x=160pm and the beam energy is 3.5GeV . The wiggler amplitude is decreased slightly at Diamond II due to the higher ring energy.

Beamline	Magnetic field[T]	a (DLS)[μm]	a (D-II)[μm]	σ_x (DLS)[μm]	σ_x (D-II)[μm]
I12	4.2	24.5	21.0	140.6	25.6
I15	3.5	32.0	27.0	112.5	29.9
I20-SCA	1.9	33.0	28.5	134.7	30.3
I20-EDU	1.2	21.0	18.0	140.6	31.2

Table 4.6: Wiggler sources information for DLS and Diamond II 160pm lattice. a is the wiggler amplitude.

In the Diamond-II CDR, where the case for a lattice producing an emittance of 160um was discussed, a beam size of $\sigma_x \approx 30\mu$m is foreseen at the wiggler locations, therefore, the ′double source′ effect would not present. Further candidate lattices using reverse bends [95] may reduce the emittance to less than 100pm, hence the beam size σ_x would be smaller than the wiggler amplitude in the I15 and I20-SCA beamlines. For these cases, the ′double source′ image might be observed. What

we are more concerned about is whether this ′double source′ will appear after the beamline focusing, because the irregular beam shape is undesired at the sample. In this section, we show a study of ′double source′ effect on the beamline I20 scanning branch and beamline I15, where possible solutions to avoid the effect in case of a very small emittance will also be proposed.

The beamline I20 scanning branch is designed for a large beam spot at the sample ($\sigma_x > 100\mu m$) and horizontal focusing is affected by geometrical aberrations. A calculation was done for the I20 scanning branch with Diamond II 80pm lattice. The photon beam energy is 8700eV.

Due to the reduction of the horizontal beam size, the wiggler generates two separate sources (see the left figure of Fig. 4.9). Then the beam is propagated to the current I20 scanning branch. After the beamline focusing, aberrations in the current layout effectively blur the double source image (see the right figure of Fig. 4.9) . Therefore the ′double source′ will not affect the beam accepted at the sample for the I20 scanning branch when $\epsilon_x = 80$pm.

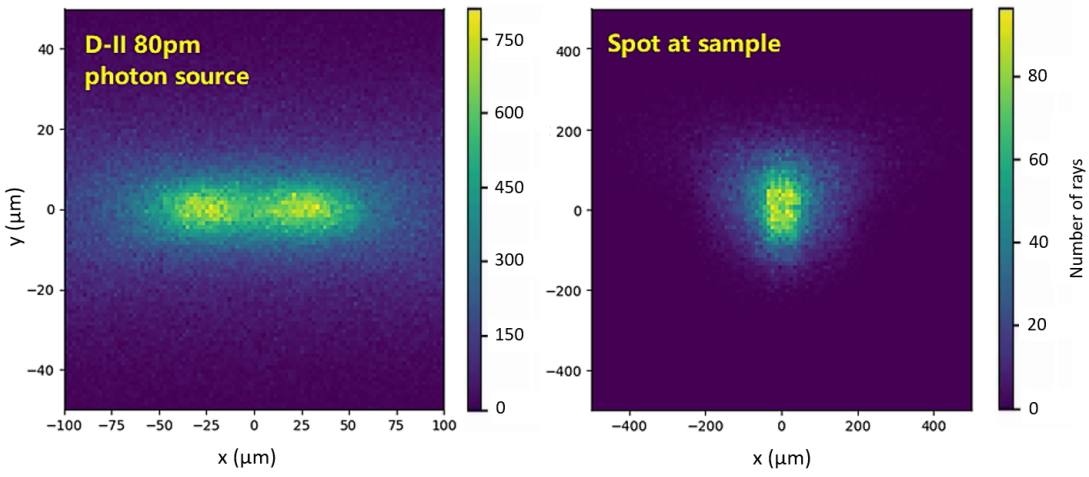

Figure 4.9: Photon source (left) of the I20 scanning branch calculated from Diamond II 80pm lattice and the beam spot after beamline focus (right).

I15 beamline in Diamond Light Source provides monochromatic high-energy X-

rays from 20 to 80 keV [24]. Si(111) double crystal monochromator and two pairs of Kirkpatrick-Baez mirrors are used to select the beam energy and focus the beam. Table. 4.7 presents the wiggler source information we used for the simulations.

Magnetic field[T]	Magnet Period (mm)	Number of Periods	Photon Energy(keV)
3.5	60	22.5	20

Table 4.7: Wiggler source of I15 beamline.

Fig. 4.10 summarizes the photon sources calculated with the Diamond II CDR lattice (left), the Diamond II reverse bends lattice (middle) and an extremely small emittance case (right). As expected the source spots become more separate when the electron beam size gets smaller.

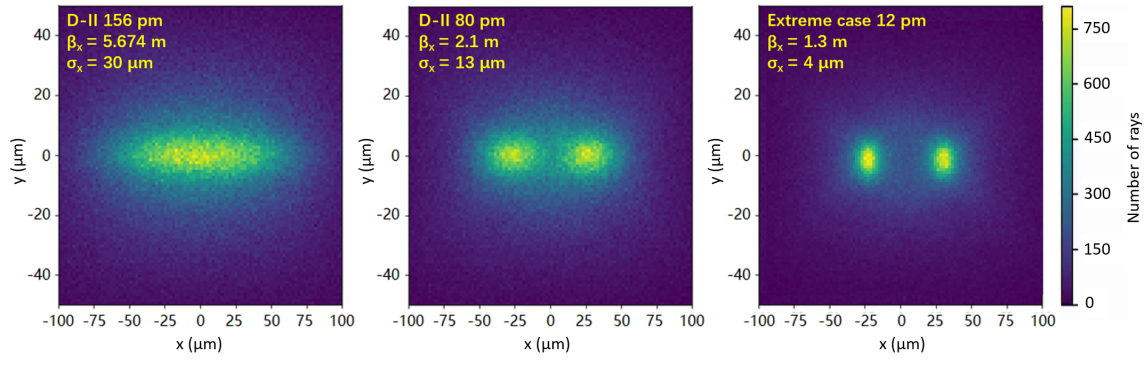

Figure 4.10: Photon source of the I15 beamline calculated with the Diamond II CDR lattice (left), Diamond II reverse bends lattice (middle) and an extreme small emittance case (right).

One of the solutions to this problem is to increase β_x at the wiggler position. For example, in the Diamond II 80pm lattice, if we increase β_x to 5.6m, the electron beam size would be $\sigma_x = 21\mu m$ and the photon source becomes a round spot as shown in Fig. 4.11.

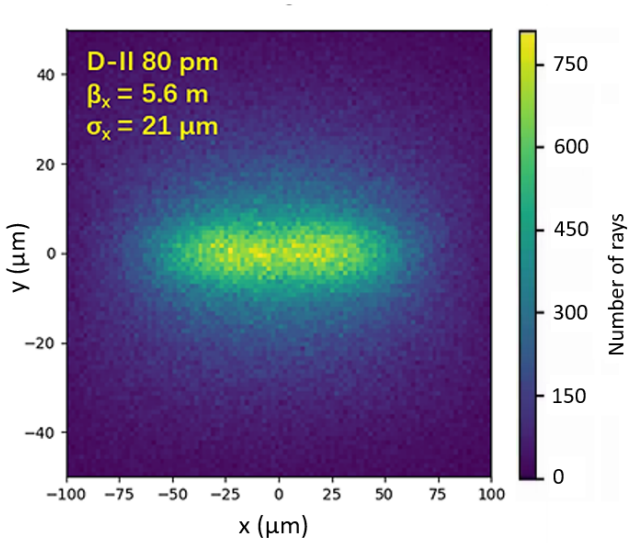

Figure 4.11: Photon source of the I15 beamline calculated with the Diamond II 80pm lattice. The wiggler is moved around 3m away from the waist.

This solution of increasing β_x could work ideally. There are two ways to increase β_x: one is to increase β_x locally in the straight section. However this is time-consuming work, because we might need to rematch the linear optics and, above all, re-optimise the non-linear beam dynamics for the new instance of the lattice [55]. Another way is to place the wiggler away from the minimum of β_x, as for I15, 2-3m distance from the waist will increase β_x to 5.6m. This solution has a limitation of space constraints since it requires a change of about 2m, an offset typically not available in straight sections of Diamond. Therefore both solutions may not be practically implementable.

Since the beamline structure has already been fixed, the only part we can change is the sample position. Hence another proposed solution is to move the sample to an off-focus point. A study was done based on this idea.

The total length of the I15 beamline is around 50m. A simple model is built with a front-end slit which makes the acceptance of the beam 0.4mrad. An ideal refractive lens is used to model the focusing property of this beamline. Fig. 4.12 shows the schematic of the simplified model of the I15 beamline.

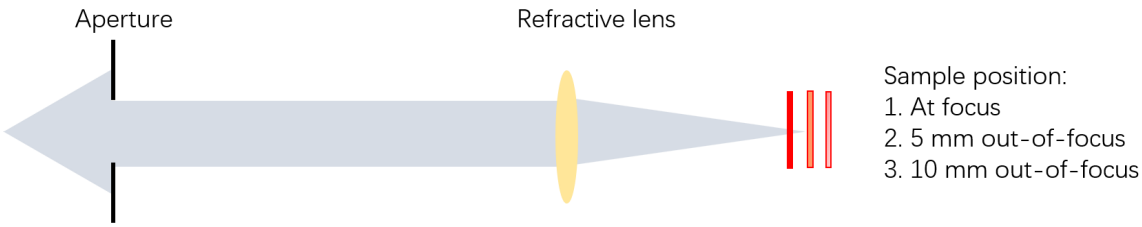

Figure 4.12: A simple model of the I15 beamline.

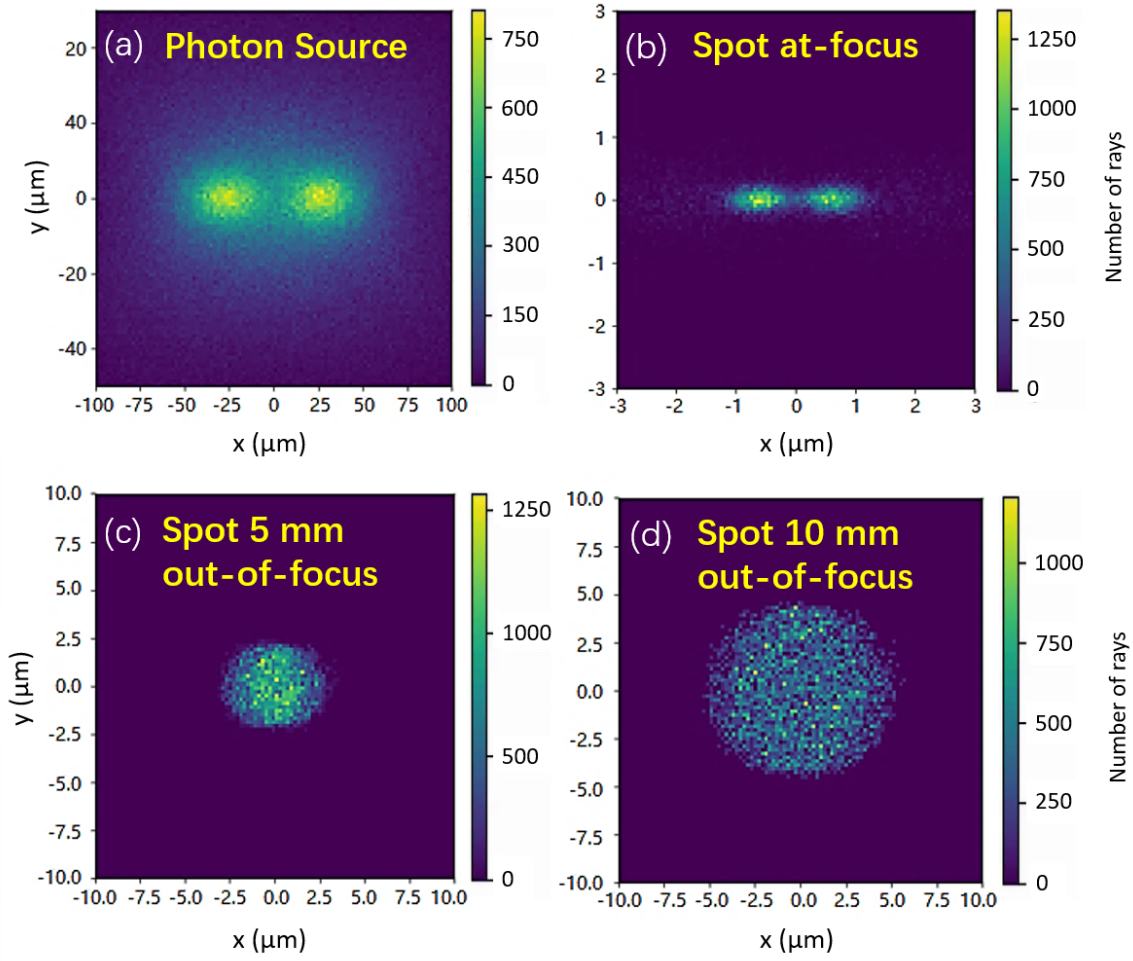

Figure 4.13: (a) Photon source of I15 beamline with Diamond II 80pm lattice. (b) Beam spot at focus point, (c) 5mm away from focus point, (d) 10mm away from focus point.

The ideal refractive lens is located at 49m and focuses the beam 1m after it. The image at the focus point is shown in Fig. 4.13 (b); two separate sources are imaged separately at the sample at an horizontal position of -1.5 μm and +1.5 μm from the optical axis. When we move the sample longitudinally 5mm away from the focus point, the two spots merge into one dense and uniform spot (Fig. 4.13 (c)). The spot is even more uniform if we put the sample 10mm away from focus point (Fig. 4.13 (d)), albeit the spot size grows larger and the intensity distribution is slightly lower.This method is practically implementable and we could adjust the sample position to satisfy the experiment sample size requirements.

Some other solutions were proposed by the Diamond Optics Group such as vibrating optics at high frequency by a piezo [96] to smear out the double source, or use an in-vacuum wiggler [97] which can reduce the wiggler amplitude. With the development of diffraction limited light sources, we are gradually producing point-like photon sources which are more likely to have such a problem. More exploratory researches can be carried out in future to mitigate the ′double source′ effect.

4.3 Three-pole wiggler beamline study

The bending magnets in the Diamond II will have a lower magnetic field (0.8T compared to 1.4 T in Diamond) and as a consequence, the critical energy will be reduced from 8.38keV to 6.52keV. The lower critical energy has important consequences on the performance of the bending magnet beamline like B18. Their operation in the Diamond II require maintaining the critical energy to 8.38keV and therefore adequate modifications to the magnetic structure should be devised. For this reason a three-pole wiggler has been investigated.

A three-pole wiggler consists of three poles as the name suggests: a main pole is used as a radiation source and two side poles for compensating the beam orbit

deflection due to the main pole field [98]. The central pole presents a high field, while the two side poles have a lower field so that the total field integral is the same [7]. The centre pole is usually operated at a higher magnetic field than the bending magnet of the ring to extend the spectrum to higher photon energies [99].

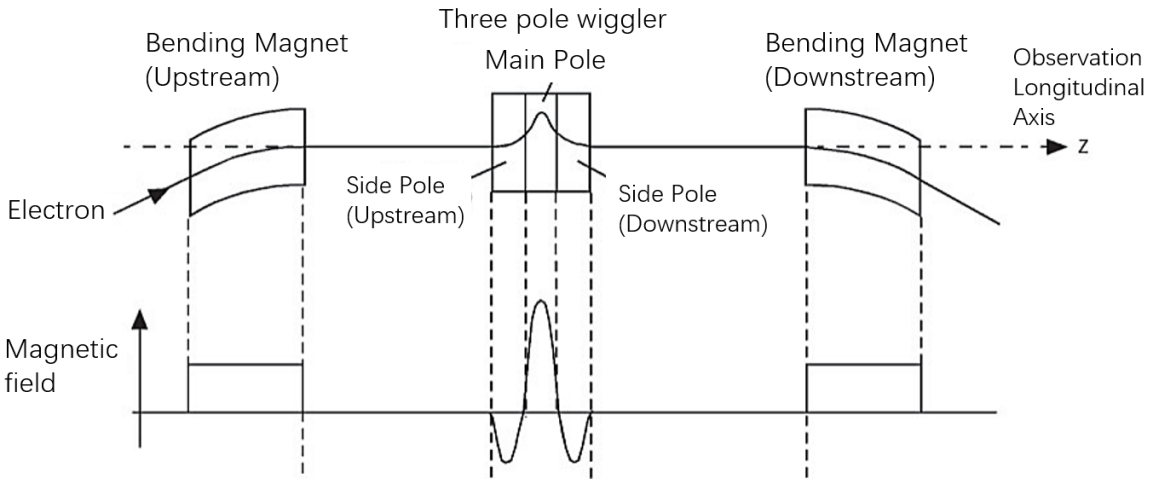

Figure 4.14: Magnet configuration and beam orbit (upper) and magnetic field on the beam orbit (lower) for the radiation model of a straight section with a three-pole wiggler [99].

The three-pole wiggler is always installed at the centre of a straight section between upstream and downstream bending magnets [99]. Hence the straight section is divided into five subsections (upstream and downstream bending magnet, upstream and downstream side or steerer poles and the main pole) as shown in Fig. 4.14. The radiation from all these five subsections will be taken into account when we model the photon source and the main goal of the optimisation is to make sure that a uniform intensity distribution is presented at the sample.

In the Diamond II design, we studied the case for four bending-magnet sources to be replaced by three-pole wigglers. In this section, we present the study of a potential three-pole wiggler beamline, beamline K18.

4.3.1 K18 beamline

The Diamond II K18 beamline is designed based on the current Diamond B18 beamline with a three-pole wiggler source instead of the bending-magnet source. A beamline schematic is shown in Fig. 4.15.

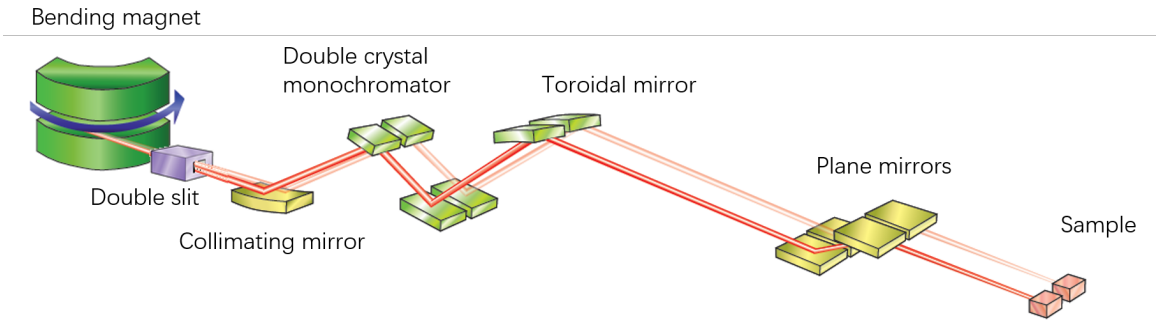

Figure 4.15: A schematic of current Diamond B18 beamline. (Reprint from [24]).

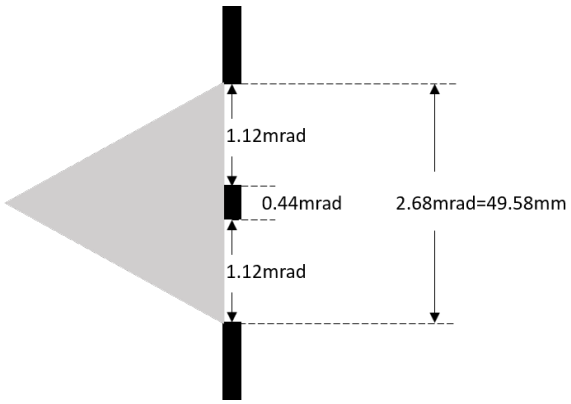

Figure 4.16: Double slit at 18.5m away from the photon source in beamline B18.

This beamline is designed for a relatively wide energy range, from 2 to 35keV. The double slit at 18.5m from the source splits the photon beam into two separate branches with acceptance 1.12mrad each as shown in Fig. 4.16. The optical elements in the two branches are identical, only the coating materials are different [100]. The first element is a vertically collimating Si mirror placed at 20 m from the source. This setup provides high energy resolution and high flux for the double crystal monochromator which selects the desired monochromatic beam. Then a toroid mirror is placed at

25m from the source to focus the beam onto the sample. Finally, a pair of plane mirrors for harmonics rejection is placed for low energy (<15keV) operations [101]. In this study, we focus on the simulation of one of the branches in K18.

4.3.2 Beamline K18 simulation

The 3PW magnetic field for K18 has a -1.45T central pole and two 0.04T side poles, each one at 0.5m from the central pole. Fig. 4.17 shows the magnetic field, electron trajectory and the angle of electron beam for the proposed 3PW and two bending magnets (DQs) for K18. This configuration was tailored to separate steerers and radiator in energy, therefore providing a nearly pure dipole source in the range 2keV-35keV [27].

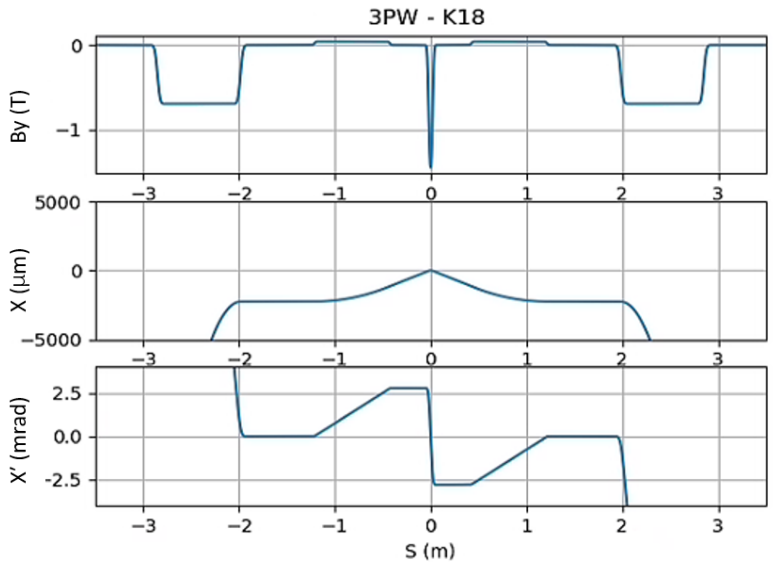

Figure 4.17: Magnetic field (top), electron trajectory (middle) and electron beam angle (bottom) of the proposed 3PW and bending magnets at the straight section of K18.

The intensity distributions calculated with SHADOW at the entrance slit position (18.5m) for DQs and 3PW are shown in Fig. 4.18. Due to the different locations of DQs, the radiation from the dipole that is closer to the entrance slit will be stronger (from -70000μm to 0 in (a)) than the farther one (from 0 to 70000μm in (a)). Compared to the intensity distribution of two energies, the effect of radiation from DQs for 35keV is not significant as for 2keV, because the critical energy for DQs are 6.52keV. After the transmission in the beamline, the beam spot at the sample for 35keV is uniform, while the undesirable radiation shape from upsteam DQ appears in the sample at 2keV.

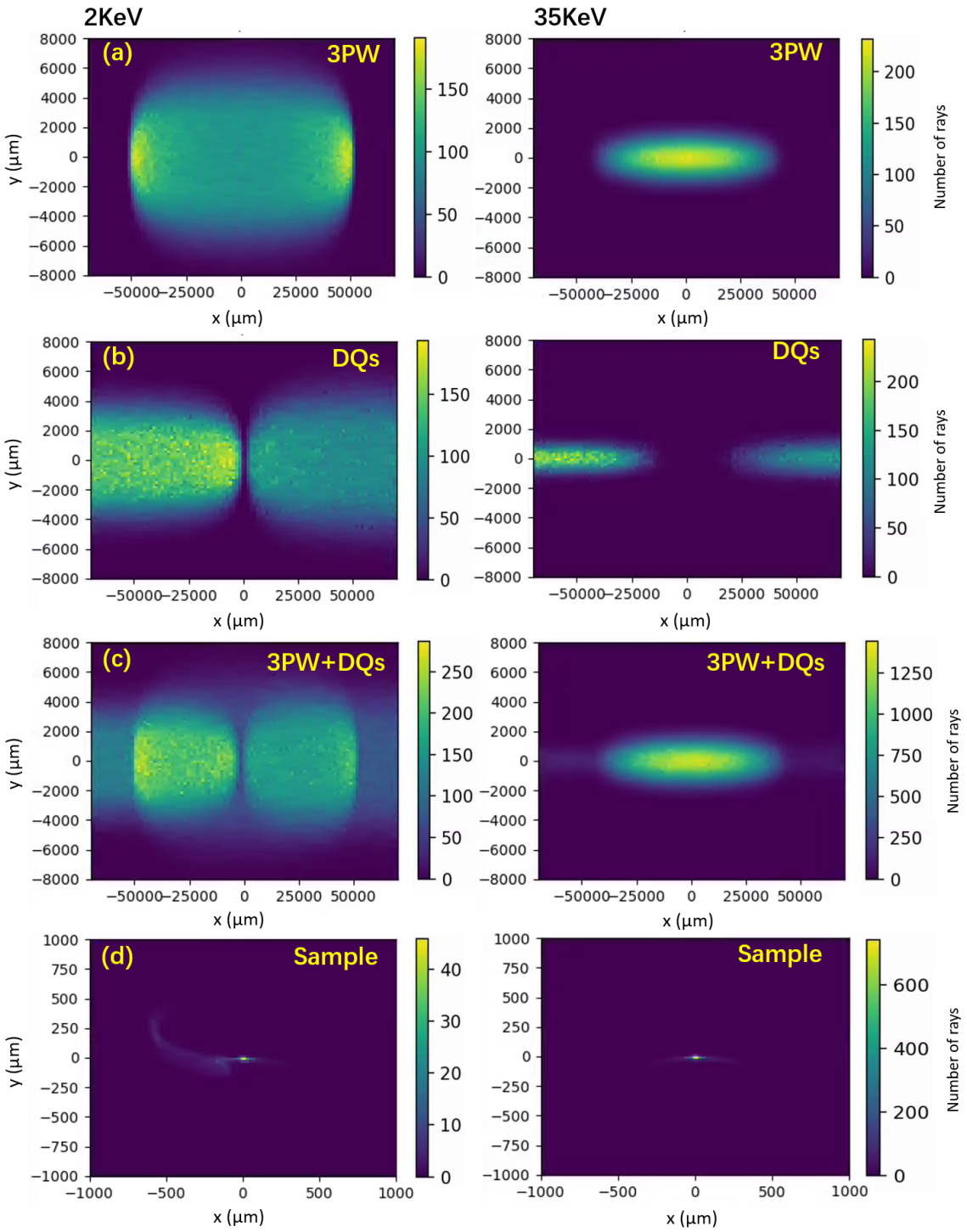

Figure 4.18: The intensity distributions for K18 3PW at 18.5m, at 2keV (left column) and 35keV (right column) calculated by SHADOW. (a) The radiation from 3PW. (b) The radiation from DQs. (c) The sum of (a) and (b) sources. (d) The intensity distributions at the sample.

4.3.3 Optimisation of Beamline K18

In order to optimise the beam spot at the sample at 2KeV, the first attempt is to improve the performance of this beamline by using the E2S-SHADOW optimiser. The selected beamline parameters are the radius of the toroid mirror and the two drifts before and after this mirror. The optimiser runs on 20 generations with a population of 50 individuals. Fig. 4.19 shows the fronts of this optimisation. The initial beam size at the sample is 0.118cm in the horizontal plane, 0.077cm in the vertical plane. After optimisation, the beam size has not improved much.

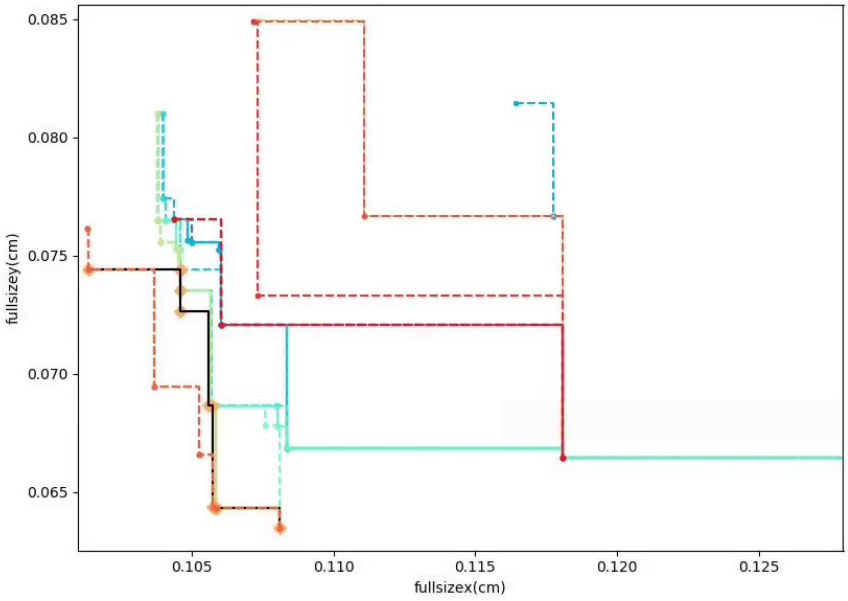

Figure 4.19: Fronts of K18 beamline optimisation calculated with E2S-SHADOW optimiser. Different colours and line types (dashed line and solid line) represent different fronts, the dots on the fronts correspond to the solutions.

Then we check the beam spot at the sample from one of the optimal configurations of the beamline. More photons concentrate to the centre of the sample after optimisation, however the curved structure is still present. Since the radiation from DQs cannot be focused well under the current beamline configuration, a better way to overcome the image problem at the sample would be by removing the radiation from DQs.

The flexibility of changing in the beamline components is limited, hence a possible design for the photon source was proposed by the Accelerator Physics group in Diamond Light Source that is bumping the beam vertically, so we can spatially separate the radiation produced by the radiator from that of the other magnets [102].

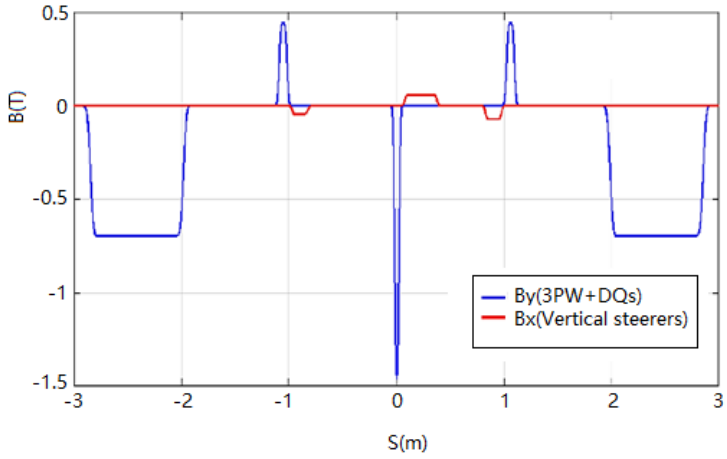

Figure 4.20: Magnetic field of K18 photon source. The magnets consist of 3PW+DQs (blue) and vertical steerers (red).

Fig. 4.20 shows the new design of the magnets. Three vertical steering poles (red line) are inserted in the 3PW (blue line) structure, which tilts the radiation of the dipoles from the beamline optical axis by +0.55mrad. At the first slit position (18.5m from the source), the radiation from the dipoles has been successfully separated (Fig. 4.21).

The entry slit is shown in Fig. 4.21 as a red box, corresponding to an acceptance of 20.57mm × 3.0525mm, so only the centre part of the radiation from the radiator will propagate to the beamline. At the sample, a uniform spot is produced (Fig. 4.22).

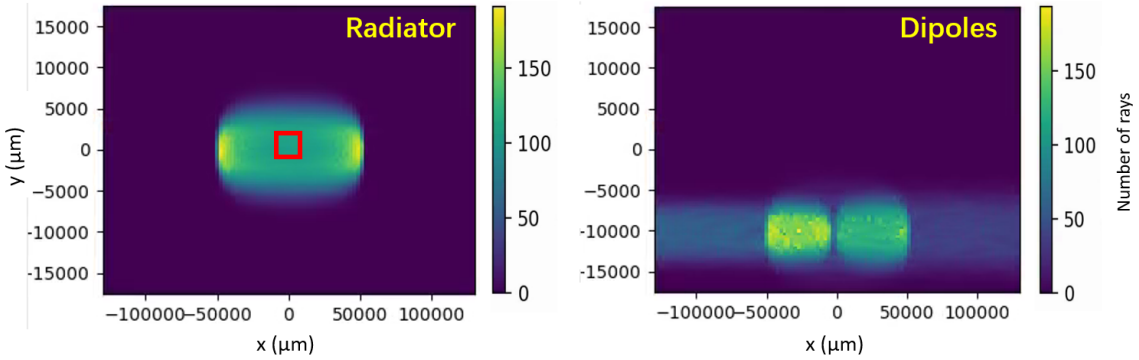

Figure 4.21: Photon beam at the entrance slit produced by radiator(left) and the other dipoles(right). The red rectangle shows the area selected by the entrance slit.

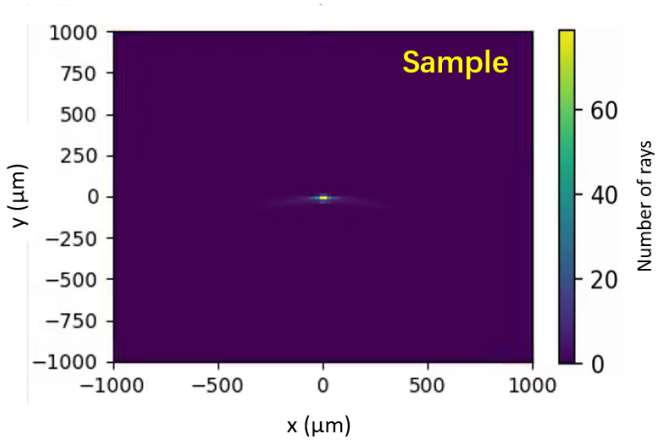

Figure 4.22: Photon beam spot at the K18 beamline sample position.

This study confirms the initial findings done by the AP group with SRW by complementing them with a full propagation of X-rays into the beamline. However, in SRW, a two-dimensional interpolation is used to re-sample the electric field on a regular mesh after local propagation, which makes the radiation from dipoles at the sample position at 2KeV is very hard to specify in the SRW simulation. Working at energies larger than 2keV makes the use of an incoherent ray tracing fully justified. From this study, we found that SHADOW tracing and propagation is hereby preferred as being simpler and faster than SRW. However SHADOW does not currently allow

one to use a magnetic field with more than one spatial component, the only way to simulate the radiation from multi-spatial magnets is by rotating the reference plane to look at the effect of the different magnets, SRW can handle this kind of source relatively easily.

4.4 Summary of this chapter

In this chapter, the work with the ray-tracing method has been presented. First, we showed the optimisations of the I13 coherence branch and the I20 scanning branch with the E2S-SHADOW optimiser. The result for the I13 coherence branch shows good agreement with the E2S-SRW optimiser result. While for the I20 scanning branch, aberration is unavoidable in relevant ray-tracing optimisations (E2S-SHADOW optimisation and Python simplex optimisation). Therefore, in future it is still necessary to study which of the two models (wavefront model and ray-tracing model) can more accurately simulate beamlines with aberrations.

A study of the ′double source′ problem for Diamond II wiggler beamlines was presented. After the assessments of four wiggler beamlines in Diamond, we selected the I20 scanning branch and beamline I15, which have the potential to show the effect of the ′double source′, for further investigation. Some possible solutions to avoid the effect in case of a small emittance were also proposed.

In the Diamond II design, three bending magnet sources will be replaced by a three-pole wiggler, hence the study of this new photon source is required. In this chapter, we showed the SHADOW simulation of a potential three-pole wiggler beamline, beamline K18. An optimisation with the E2S-SHADOW optimiser on this three-pole wiggler beamline was done to eliminate the effect of dipole radiation. The optimisation result shows it can only mitigate the effect without eliminating it completely. Another possible solution was proposed that is bumping the beam vertically. The sim-

ulation based on this idea showed the radiation useful to the beamline is successfully separated from the one generated by the other magnets and can be fully propagated to the sample without further contamination, which provided a new direction for the three-pole wiggler design.

Chapter 5

Conclusion and future work

In recent years, a new class of synchrotron radiation light sources has been established that can produce X-ray beams with revolutionary properties, unprecedented quality, extremely high brightness and stability. Many synchrotron sources around the world are at an advanced stage of design, aiming to build the next generation of diffraction-limited light sources based on ultra-low emittance accelerator lattice designs. These projects are based on substantial research and development work of many technical components to meet the technical challenges of producing such high quality X-ray beams. One of the key challenges is in the optimisation of the electron optics, combined with the photon optics of the beamlines in order to take full advantage of the reduced electron beam emittance and the increased brightness and coherence of the radiation.

The work presented in this thesis aimed at understanding the trade-offs and finding the best compromise between the beamline performance parameters and the machine parameters. The definition and optimisation of electron and photon optics are carried out by means of computer codes and advanced numerical techniques. This optimisation technique was applied to the existing Diamond Light Source (DLS) beamlines and contributed to the Diamond upgrade design.

5.1 Development of the codes

A wrapper code package called E2S (Electron to Sample) was developed to enable a complete simulation of the synchrotron radiation from the source point to the sample. The code starts used Elegant [56] for the machine parameters and beam dynamics and SRW [57] for simulating the emission and propagation of photons.

So far E2S can calculate the flux, brightness, tuning curves, intensities and power density of a beamline. Previously, the power density distribution could only be calculated in free space propagation, hence a method was developed to overcome such limitation allowing the propagation of the power density distribution at any position of a beamline.

The undulator beamline I13 coherence branch at DLS was used as an example to show the simulation products of E2S. After the model was established, a study of the electron orbit corrections to the properties of the radiation in the I13 coherence branch was carried out and gave a better understanding of the propagation of the wavefront through the beamline in presence of orbit variations. The study also verified the selection property of the monochromator, which shows good agreement with the theory.

The design of a beamline is always an extremely challenging task due to the large number of degrees of freedom in the chain of optical components, the photon properties and the electron dynamics in the machine. SRW, which propagates photons according to a wave-front model, and SHADOW, which simulates the propagation of photons by a geometrical ray-tracing method, are two commonly used codes at DLS. However, the shortcoming of these two approaches is they cannot guarantee that the final setup is the best configuration. For most of the time, the optimisation of a beamline is based upon the experience of scientists and relies on a trial-and-error approach which can be particularly time consuming. A beamline optimiser,

based on the Non-Dominated Sorting Genetic Algorithm II (NGSA II) [58] has been implemented in E2S [82]. In the optimiser, NSGA II is linked to the SRW (E2S-SRW optimiser) or the SHADOW (E2S-SHADOW optimiser). Both optimisers can help find a better beamline configuration in a more efficient way.

5.2 Optimisation of beamlines

The beamline optimisations in this work are implemented to improve the performance of current DLS beamlines and to help find the best configuration of a beamline for Diamond II at the design stage.

The E2S-SRW optimiser was applied to optimise an undulator beamline (Diamond I13 coherence branch) and a wiggler beamline (Diamond I20 scanning branch). The study starts from a well-designed beamline, beamline I13 coherence branch. A comparison of 2D and 7D beamline optimisations illustrate that a higher number of degrees of freedom can improve the optimisation. The parameter space was then extended to include machine parameters like the Twiss functions, leading to a marginal improvement in beam performance. For a beamline in an uncertain state (random beamline in design stage), the optimisations for beamline (BL) only and BL+Twiss were repeated. It was found that the optimiser can still converge towards the same optimal solution as the well-designed beamline optimisation. This suggests that the solution to the multi-objective optimisation of a beamline does not depend on the initial values of the beamline parameters. A phenomenon of "front transition" was observed in random beamline optimisation. The reason for this mechanism is that the first front corresponds to a local minimum, which can be avoided by exploring a sufficient number of parameters, which is a decisive advantage of the genetic optimsation algorithms.

The beam spot at the sample position for the I20 scanning branch shows the effect of aberration from the beamline. A first optimsation of the beamline performance was attempted using the response matrix connecting the spot size to the beamline parameters. The response matrix based approach is very fast but requires to be fairly close to the best solution. If this is not the case, the often intrinsic non-linearity of the problem may lead to poor or even non-physical solutions. Then the E2S-SRW optimiser was used to optimise the beamline with beamline parameters only and BL+Twiss parameters.

After the optimisation of the two beamlines, the photon beam performances at the sample all showed a significant increase. The solution indicated by the optimiser should be assessed in terms of their practical implementation in the beamline layout. This could imply practical restrictions: if the optimisation is carried out on an already-built system, the freedom in the optimisation space could be limited. These restrictions are obviously less severe in a green-field design of the beamline.

The ray-tracing based optimisations were performed with the E2S-SHADOW optimiser. The same beamline parameters as in the E2S-SRW optimiser were chosen to optimise the I13 coherence branch and the I20 scanning branch. The outcome of the I13 coherence branch shows a good agreement with the E2S-SRW optimiser result. For the I20 scanning branch ray-tracing simulation optimisation, two optimisation methods were implemented, one is the NSGA-II, the other is the Python simplex optimisation. Both optimisations showed that the way to uniformize the beam spot is to enlarge the centre of the beam spot to weaken the aberration effect.

Undulator and wiggler beamlines are two commonly used photon sources in current third generation light sources. Since two types of insertion devices have been addressed in the E2S optimisations presented in this thesis, we believe that our approach can be easily extended to similar beamlines in other light sources.

With the development of diffraction limited light sources, point-like photon sources are gradually being achieved. The candidate lattices of Diamond II may reduce the emittance from 2700pm to 80pm where the ′double source′ effect may occur in the wiggler beamlines. After the assessments of four wiggler beamlines in the Diamond, I20 scanning branch and beamline I15, which have the potential to show the ′double source′ effect, were selected for further investigation. Some possible solutions to avoid the effect in case of a small emittance were proposed in this study.

In the Diamond II design, some bending magnet sources will be replaced by a three-pole wiggler, hence the study of this new photon source is required. Since the radiation from the centre pole is the most needed, an optimisation was carried out with the E2S-SHADOW optimiser on a potential three-pole wiggler beamline to eliminate spurious radiation from the gradient dipoles.

The optimisation result has shown that it is only possible to weaken the effect, not completely eliminate it. Another possible solution was proposed that is bumping the beam vertically. The simulation based on this idea showed the radiation from the 3PW central radiator can be successfully separated from the other magnets, which provides a new direction for the design of three-pole wiggler photon source.

5.3 Future work

First of all, most of the work presented in this thesis is theoretical, therefore experimental benchmarking is needed to test the accuracy of the simulations. The simulations in this thesis are implemented in two well-known synchrotron radiation modelling programs (SRW and SHADOW). The two methods are complementary and can be used in combination in the design or optimisation of a beamline, which can give us more information about the performance of the beamline.

Genetic algorithms (GAs) have been used in lattice optimisations for decades

[103][76], however the application of GAs to beamline optimisation has just begun. For a beamline system, the optical element parameters and drift lengths are limited for various situations. In order to obtain a more practical optimisation, the constraints of the optical elements should therefore be supplemented to the optimiser.

The full optimisation including Twiss parameters and beamline parameters was presented in this thesis, while in a realistic case, the choice of Twiss parameters is strictly constrained by the particle accelerator lattice and crucially by effects of non-linear dynamics. For further research the result of the optimiser can be linked with Elegant to optimise also the nonlinear electron dynamics and photon dynamics together, which could form an optimisation loop to obtain a more reliable solution.

Overall, E2S builds the bridge from electron dynamics to photon dynamics. It would be a valuable tool for the design and upgrade of synchrotron radiation light sources in future.

.

Appendix A

Code structure of E2S

In order to enable readers to have a more intuitive understanding of how E2S works, the supplementary appendix is written to address the structure of the E2S code.

An E2S input file is used to launch the program. The machine parameters, ID parameters, photon energy, front-end slit position and size of a beamline and SRW calculation settings are defined in this file. Fig. A.1 shows an example of E2S input file. The position of ID will be passed to Elegant which calculates the Twiss parameters for the desired location from the lattice file. Then the Twiss parameters combined with machine parameters are used to calculate the electron beam size, divergence and moments. After the calculation from Elegant, a new SRW input file will be created. The Twiss parameters and electron beam information have been added to the new input file. Brightness and tuning curves are calculated by the two functions (sddsbrightness and sddsfluxcurve) in Elegant, these two simulations can be completed at this stage.

```
-----SR:  =
SynchRad  = SRW
-----ID:  =
IDname    = I13d
IDpos     = 282.298
IDpos_min = 0.01
IDpos_max = 0.01
Np_und    = 108.0
lam_und   = 0.025
By_und    = 0.836
Kmin      = 1.0
Kmax      = 2.0
KRangeNbPoints = 100
TCPoints      = 100
Brightness   = 1
TuningCurves = 1
harm_1st     = 1
harm_last    = 20
-----SRW-Beamline: =
slitZ     = 11.55
Ephot_ini = 1000.
Ephot_end = 25000.
slitDX    = 300.
slitDY    = 120.
-----SRW-Calculation: =
meshXsta  = -700.
meshXfin  =  700.
meshYsta  = -400.
meshYfin  =  400.
meshEsta  = 11209
meshEfin  = 11209
Nelectr   = 50
Ncores    = 10
calc_type = multie
calc_meth = 1
------SR: =
LATTICE   = M-H6BA-15-1-1
Ee        = 3.5
Ib        = 0.3
Nbunch    = 935
Cou       = 0.0507
```

Figure A.1: An example of an E2S input file.

The SRW input file is used to start the flux, intensity, partially coherent wavefront and power density for free space propagation simulations in SRW. Flux within the front-end slit and power density at a position before the front-end slit are calculated directly from SRW. Then the photon beam will propagate through a beamline. The beamline configuration is defined in a file that lists all the optical parameters and drift lengths. Three calculation modes (fully coherent, multi-electron, partially coherent) can be chosen to calculate the intensity at any position along the beamline. The

method used to simulate a generic power density distribution along the beamline as described in Chapter 2 is achieved by combining the flux and intensity calculations. Fig. A.2 summarises the code structure of the above simulations.

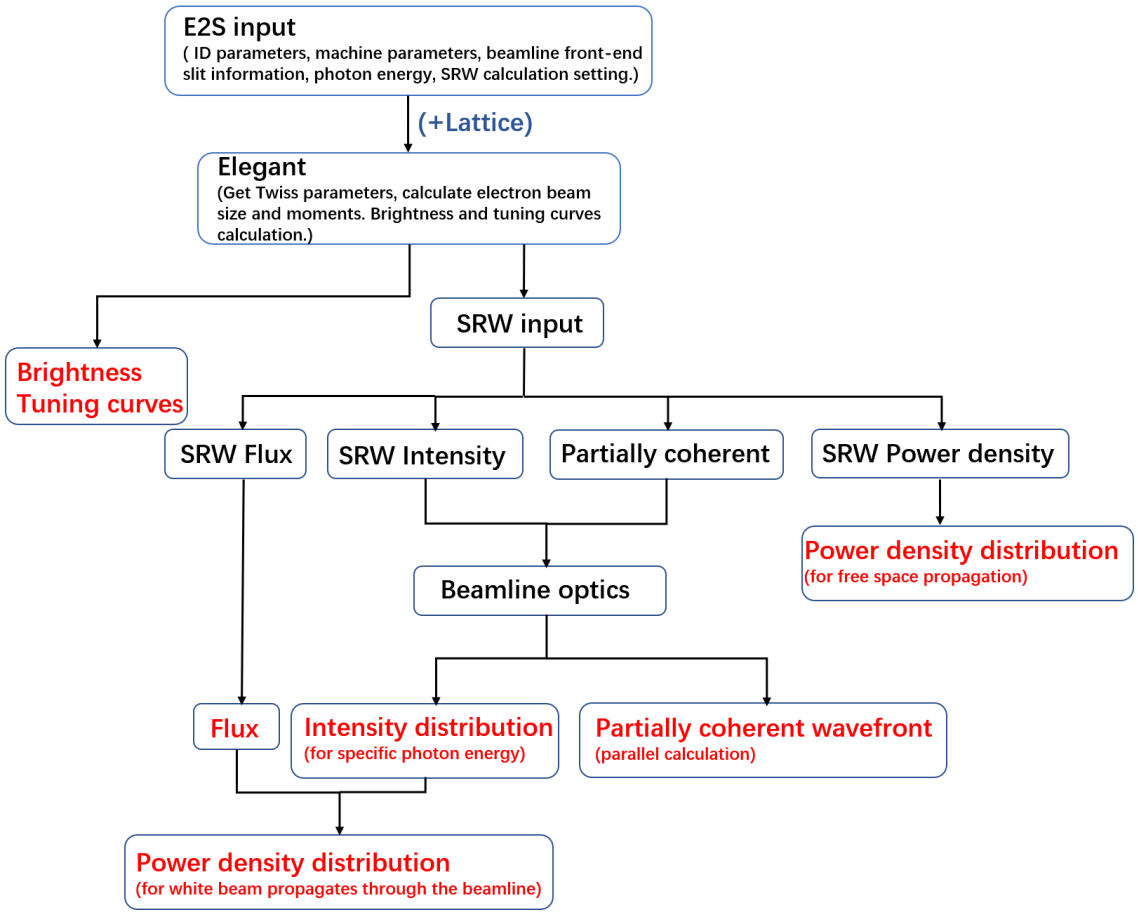

Figure A.2: A flow chart to show the code structure for brightness, tuning curves, flux, intensity and power density simulations in E2S.

Another part of E2S is the optimiser. Two optimisers have been developed in E2S, E2S-SRW optimiser and E2S-SHADOW optimiser. Fig. A.3 shows the code structure for the two optimisers. For the E2S-SRW optimiser, the SRW intensity calculation is involved in the NSGA II optimisation. The E2S-SHADOW optimiser is built based on the SHADOW-Python. The input file of SHADOW-Python contains both the emission and propagation of the photon beam, therefore the distribution of the photon beam can be calculated directly by running the SHADOW-Python input

file. The analysis process is the same for both optimisers and users can select the desired photon beam spot size from fronts map to obtain the corresponding optimised beamline configuration.

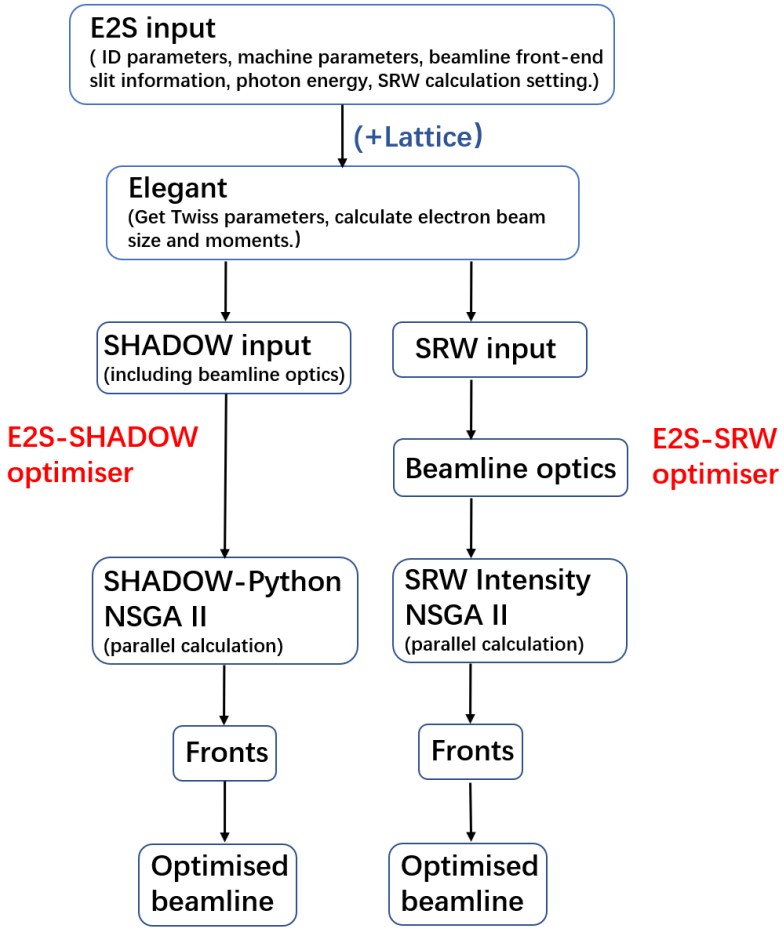

Figure A.3: A flow chart to show the code structure for E2S-SRW optimiser and E2S-SHADOW optimiser.

Bibliography

[1] A. Liénard. *Champ électrique et magnétique produit par une charge électrique concentrée en un point et animée d'un mouvement quelconque*. G. Carré et C. Naud, (1898).

[2] F. Elder, A. Gurewitsch, R. Langmuir, and H. Pollock. Radiation from electrons in a synchrotron. *Physical Review*, 71(11): 829, (1947).

[3] J. Schwinger. On the classical radiation of accelerated electrons. *Physical Review*, 75(12): 1912, (1949).

[4] T. Pulampong. *Ultra-low emittance lattice design for advanced synchrotron light sources*. DPhil thesis, University of Oxford, (2015).

[5] S. Gayadeen. *Synchrotron electron beam control*. DPhil thesis, Oxford University, UK, (2014).

[6] H. Winick. Fourth generation light sources. In *Proceedings of the 1997 Particle Accelerator Conference (Cat. No. 97CH36167)*, volume 1, page 37. IEEE, (1997).

[7] H. Onuki and P. Elleaume. *Undulators, wigglers and their applications*. CRC Press, (2002).

[8] K Codling. Applications of synchrotron radiation (ultraviolet spectral light source). *Reports on Progress in Physics*, 36(5): 541, (1973).

[9] D. Alferov, Y. A. Bashmakov, and E. Bessonov. Radiation of relativistic particles in an undulator. *Soviet Physics Technical Physics*, 17: 1540, (1973).

[10] V. Baier and A. Milstein. To the theory of a free-electron laser. *Physics Letters A*, 65(4): 319, (1978).

[11] H. Winick and R. H. Helm. Standard wiggler magnets. *Nuclear Instruments and Methods*, 152(1): 9, (1978).

[12] S Doniach, K Hodgson, I Lindau, P Pianetta, and H Winick. Early work with synchrotron radiation at stanford. *Journal of synchrotron radiation*, 4(6): 380, (1997).

[13] K. Wille. Synchrotron radiation. *Proceedings of the CERN Accelerator School 2013*, (2013).

[14] R. P. Walker. Insertion devices: undulators and wigglers. *Proceedings of the CERN Accelerator School*, (1998).

[15] D. F. Alferov, Y. A. Bashmakov, and E. G. Bessonov. Undulator radiation. *Sov. Phys.-Tech. Phys. (Engl. Transl.)*, 18(10): 1336, (1974).

[16] S. Krinsky. Undulator for the 700 MeV VUV-Ring of the National Synchrotron Light Source. Technical report, Brookhaven National Lab., Upton, NY (USA), (1979).

[17] I. P. S. Martin. *Short pulse X-ray generation in synchrotron radiation sources*. DPhil thesis, University of Oxford, (2011).

[18] D. Attwood and A. Sakdinawat. *X-rays and extreme ultraviolet radiation: principles and applications*. Cambridge University Press, (2017).

[19] K.-J. Kim. Brightness, coherence and propagation characteristics of synchrotron radiation. *Nuclear Instruments and Methods in Physics Research Section A: Accelerators, Spectrometers, Detectors and Associated Equipment*, 246(1-3): 71, (1986).

[20] J. Schwinger. On the classical radiation of accelerated electrons. *Physical Review*, 75(12): 1912, (1949).

[21] K.-J. Kim. Angular distribution of undulator power for an arbitrary deflection parameter K. *Nuclear Instruments and Methods in Physics Research Section A: Accelerators, Spectrometers, Detectors and Associated Equipment*, 246(1-3): 67, (1986).

[22] R.P.Walker. Radiation damping. *Proceedings of General Accelerator Physics, CERN Geneva*, (1990).

[23] K. W. Robinson. Radiation effects in circular electron accelerators. *Physical Review*, 111(2): 373, (1958).

[24] Diamond light source. `https://www.diamond.ac.uk/Home.html`. [Online; accessed 10-10-2020].

[25] Diamond Light Source. Diamond-II | Advancing Science. https://www.diamond.ac.uk/Home/About/Vision/Diamond-II.html. [Online; accessed 10-10-2020].

[26] R Bartolini, C Abraham, M Apollonio, C. Bailey, M. Cox, A Day, R. Fielder, N. Hammond, M. Heron, R Holdsworth, et al. Double-double bend achromat cell upgrade at the Diamond Light Source: From design to commissioning. *Physical Review Accelerators and Beams*, 21(5): 050701, (2018).

[27] Diamond Light Source. Diamond-II | Conceptual Design Report. https://www.diamond.ac.uk/Home/About/Vision/Diamond-II.html. [Online; accessed 10-10-2020].

[28] B. W. Batterman and D. H. Bilderback. X-ray monochromators and mirrors. *Handbook on synchrotron radiation*, 3: 105, (1991).

[29] L. Gregoratti. Scanning photoemission microscopy: applications and examples. *School on Synchrotron and Free-Electron-Laser Sources and their Multidisciplinary Applications*, (2010).

[30] G. V. Marr. *Handbook on Synchrotron Radiation: Vacuum Ultraviolet and Soft X-ray Processes*, volume 2. Elsevier, 2013.

[31] W. B. Peatman. *Gratings, mirrors and slits: Beamline design for soft X-ray Synchrotron radiation sources*. CRC Press, (1997).

[32] Summary of the performance of Common X-ray Optics. https://www.sigray.com/xray-optics-primer. [Online; accessed 18-11-2020].

[33] P. Kirkpatrick and A. V. Baez. Formation of optical images by X-rays. *JOSA*, 38(9): 766, (1948).

[34] Spectroscopic Properties of Gratings. https://www.spectrogon.com/product-services/gratings/spectroscopic-properties-of-gratings/. [Online; accessed 10-10-2020].

[35] N. W. Ashcroft and N. D. Mermin. *Solid state physics*. Harcourt College, (1976).

[36] T. Matsushita and H Hashizume. X-ray monochromators. *Handbook on Synchrotron Radiation*, 1: 261, (1983).

[37] J Härtwig and S Grosswig. Measurement of X-ray diffraction angles of perfect monocrystals with high accuracy using a single crystal diffractometer. *physica status solidi (a)*, 115(2): 369, (1989).

[38] J. Prins. The reflection of X-rays on absorbing ideal crystals. *Journal for Physics*, 63(7-8): 477, (1930).

[39] D. Koningsberger and R. Prins. *X-ray absorption: principles, applications, techniques of EXAFS, SEXAFS, and XANES*. (1988).

[40] F. Seitz, D. Turnbull, and H. Ehrenreich. *Solid state physics*. Academic Press, (1968).

[41] N Kato. A note on the darwin-prins rocking curve for perfect crystals. *Acta Crystallographica Section A: Foundations of Crystallography*, 48(6): 829, (1992).

[42] A. Snigirev, V. Kohn, I. Snigireva, and B. Lengeler. A compound refractive lens for focusing high-energy x-rays. *Nature*, 384(6604): 49, (1996).

[43] Compound refractive X-ray optics. `http://www.rxoptics.de`. [Online; accessed 10-10-2020].

[44] D Weiss, G Schneider, B Niemann, P Guttmann, D Rudolph, and G Schmahl. Computed tomography of cryogenic biological specimens based on x-ray microscopic images. *Ultramicroscopy*, 84(3-4): 185, (2000).

[45] O. Wilhelmi, S. Reyntjens, C. Mitterbauer, L. Roussel, D. J. Stokes, and D. H. Hubert. Rapid prototyping of nanostructured materials with a focused ion beam. *Japanese Journal of Applied Physics*, 47(6S): 5010, (2008).

[46] J. Kirz. Phase zone plates for X rays and the extreme UV. *JOSA*, 64(3): 301, (1974).

[47] J. Tummler. *Development of Compound Refractive Lenses for Hard X-rays: A Novel Instrument in Hard X-ray Analysis*. Shaker Verlag, (2000).

[48] P. F. Tavares, S. C. Leemann, M. Sjöström, and Å. Andersson. The MAX IV storage ring project. *Journal of synchrotron radiation*, 21(5): 862, (2014).

[49] P. Raimondi. ESRF-EBS: The extremely brilliant source project. *Synchrotron Radiation News*, 29(6): 8, (2016).

[50] L. Liu, N. Milas, A. H. Mukai, X. R. Resende, and F. H. de Sá. The SIRIUS project. *Journal of synchrotron radiation*, 21(5): 904, (2014).

[51] S. Henderson et al. Status of the APS upgrade project. In *6th Int. Partile Accelerator Conf. IPAC'15,Richmond, USA*, 1791, (2015).

[52] C. Steier, A. Anders, J. Byrd, K. Chow, S. De Santis, R. Duarte, J.-Y. Jung, T. Luo, H. Nishimura, T. Oliver, et al. ALS-U: A Soft X-Ray diffraction limited

light source. In *North American Particle Accelerator Conference. Proceedings of NAPAC2016, TUB1CO03, Chicago, IL, USA*, (2016).

[53] A. Streun, T. Garvey, L. Rivkin, V. Schlott, T. Schmidt, P. Willmott, and A. Wrulich. SLS-2–the upgrade of the Swiss Light Source. *Journal of synchrotron radiation*, 25(3): 631, (2018).

[54] L. Nadolski, P Betinelli, F Bouvet, P Brunelle, A Buteau, L Cassinari, C Benabderahmane, M. Couprie, X Delétoille, C Herbeaux, et al. SOLEIL Operation and On-going Projects. *MOPRO051, IPAC'14*, (2014).

[55] M. Apollonio, L. Alianelli, F. Bakkali Taheri, R. Bartolini, A. Dent, and J. Li. Evaluating the Impact of Diamond-II Possible Lattices on Beamlines. In *9th Int. Particle Accelerator Conf.(IPAC'18), Vancouver, BC, Canada, April 29-May 4, 2018*, 4033. JACOW Publishing, Geneva, Switzerland, (2018).

[56] M. Borland. Elegant: A flexible SDDS-compliant code for accelerator simulation. Technical report, Argonne National Lab., IL (US), (2000).

[57] O. Chubar and P Elleaume. Accurate and efficient computation of synchrotron radiation in the near field region. *In proc. of the EPAC98 Conference*: 1177, (1998).

[58] K. Deb, A. Pratap, S. Agarwal, and T. Meyarivan. A fast and elitist multiobjective genetic algorithm: NSGA-II. *IEEE transactions on evolutionary computation*, 6(2): 182, (2002).

[59] B Lai and F Cerrina. Shadow: a synchrotron radiation ray tracing program. *Nuclear Instruments and Methods in Physics Research Section A: Accelerators, Spectrometers, Detectors and Associated Equipment*, 246(1-3): 337, (1986).

[60] D. M. Ritchie, B. W. Kernighan, and M. E. Lesk. *The C programming language*. Prentice Hall Englewood Cliffs, (1988).

[61] H. Grote and F. C. Iselin. The MAD program (methodical accelerator design): version 8.10; user's reference manual. Technical report, CM-P00049316, (1993).

[62] M. Borland. A self-describing file protocol for simulation integration and shared postprocessors. In *Proceedings Particle Accelerator Conference*, volume 4, 2184. IEEE, (1995).

[63] Advanced Photon Source. Getting Started with Elegant. `https://wiki.jlab.org/ciswiki/images/6/68/130312_GTS.pdf`. [Online; accessed 10-10-2020].

[64] R. Walker. Near field effects in off-axis undulator radiation. *Nuclear Instruments and Methods in Physics Research Section A: Accelerators, Spectrometers, Detectors and Associated Equipment*, 267(2-3): 537, (1988).

[65] O. Chubar. Precise computation of electron-beam radiation in nonuniform magnetic fields as a tool for beam diagnostics. *Review of scientific instruments*, 66(2): 1872, (1995).

[66] O. Chubar. Theory of synchrotron infrared emission. *ESRF userreport*, BP 220, F-38043 Grenoble Cedex, France.

[67] O. Chubar et al. Synchrotron Radiation Workshop. `https://github.com/ochubar/SRW`. [Online; accessed 10-10-2020].

[68] J. D. Jackson. *Classical electrodynamics*. American Association of Physics Teachers, (1999).

[69] M. Born and E. Wolf. *Principles of optics: electromagnetic theory of propagation, interference and diffraction of light*. Elsevier, (2013).

[70] F. Cerrina, C Welnak, G. Chen, and M Sanchez del Rio. Shadow primer. *Center for X-ray Lithography, University of Wisconsin, Wisconsin, USA*, (1994).

[71] F.Cerrina. SHADOW User's Guide. `http://ftp.esrf.eu/pub/scisoft/shadow/documentation/shadow-source.pdf`, (1998). [Online; accessed 10-10-2020].

[72] F. Cerrina, C. Welnak, G.J. Chen, and M. Sanchez del Ri. SHADOW TRACE 2.0. `http://ftp.esrf.eu/pub/scisoft/shadow/documentation/shadow-trace.pdf`, (2002). [Online; accessed 10-10-2020].

[73] N. Canestrari, O. Chubar, and R. Reininger. Partially coherent x-ray wavefront propagation simulations including grazing-incidence focusing optics. *Journal of synchrotron radiation*, 21(5): 1110, (2014).

[74] O. Chubar, L. Berman, Y. S. Chu, A. Fluerasu, S. Hulbert, M. Idir, K. Kaznatcheev, D. Shapiro, Q. Shen, and J. Baltser. Development of partially-coherent wavefront propagation simulation methods for 3rd and 4th generation synchrotron radiation sources. In *Advances in Computational Methods for X-Ray Optics II*, volume 8141,814107. International Society for Optics and Photonics, (2011).

[75] X. Shi, R. Reininger, M. Sanchez del Rio, and L. Assoufid. A hybrid method for X-ray optics simulation: combining geometric ray-tracing and wavefront propagation. *Journal of synchrotron radiation*, 21(4): 669, (2014).

[76] A. Hofler, B. Terzić, M. Kramer, A. Zvezdin, V. Morozov, Y. Roblin, F. Lin, and C. Jarvis. Innovative applications of genetic algorithms to problems in accelerator physics. *Physical Review Special Topics Accelerators and Beams*, 16(1): 010101, (2013).

[77] C. Rau. Imaging with coherent synchrotron radiation: X-ray imaging and coherence beamline (I13) at Diamond Light Source. *Synchrotron Radiation News*, 30(5): 19, (2017).

[78] B Singh, R Bartolini, R Fielder, E. Longhi, I. Martin, U. Wagner, and C Rau. Double Mini-Beta Y Plus Virtual Focussing Optics For Diamond Storage Ring. *Proc. of PAC, Vancouver, BC, Canada*, (2009).

[79] T. Tanaka and H. Kitamura. Spectra: a synchrotron radiation calculation code. *Journal of synchrotron radiation*, 8(6): 1221, (2001).

[80] F. Masiello, G. Cembali, A. I. Chumakov, S. H. Connell, C. Ferrero, J. Härtwig, I. Sergeev, and P. Van Vaerenbergh. Rocking curve measurements revisited. *Journal of Applied Crystallography*, 47(4): 1304, (2014).

[81] O. L. Sergey A. Stepanov Eric Gullikson and E. Kondrashkina. Crystal susceptibilities for X-ray scattering and Bragg diffraction. `https://x-server.gmca.aps.anl.gov/x0h.html`. [Online; accessed 10-10-2020].

[82] F. Bakkali Taheri, M. Apollonio, R. Bartolini, J. Li, and B. Singh. Genetic Optimisation of Beamline Design for DIAMOND. In *10th Int. Partile Accelerator Conf. IPAC'19, Melbourne, Australia, 19-24 May 2019*, 3753. JACOW Publishing, Geneva, Switzerland, (2019).

[83] O. Chubar, A. Fluerasu, L. Berman, K. Kaznatcheev, and L. Wiegart. Wavefront propagation simulations for beamlines and experiments with" synchrotron radiation workshop". 425(16): 162001, (2013).

[84] S. Diaz-Moreno, M. Amboage, M. Basham, R. Boada, N. E. Bricknell, G. Cibin, T. M. Cobb, J. Filik, A. Freeman, K. Geraki, et al. The spectroscopy village at diamond light source. *Journal of synchrotron radiation*, 25(4): 998, (2018).

[85] A. Terebilo. Accelerator modeling with matlab accelerator toolbox. In *PACS2001. Proceedings of the 2001 Particle Accelerator Conference (Cat. No. 01CH37268)*, volume 4, 3203. IEEE, (2001).

[86] S. Diaz-Moreno, S. Hayama, M. Amboage, A Freeman, J Sutter, and G Duller. I20; the versatile X-ray absorption spectroscopy beamline at diamond light source. 190(1): 012038, (2009).

[87] J. Sutter, G Duller, S Hayama, U Wagner, and S Diaz-Moreno. Performance of multi-crystal bragg x-ray spectrometers under the influence of angular misalignments. *Nuclear Instruments and Methods in Physics Research Section A: Accelerators, Spectrometers, Detectors and Associated Equipment*, 589(1): 118, (2008).

[88] Z. HUANG, X. DONG, F. GAO, and C. XU. Slope error and aberration analysis for XRDX beamline toroidal focusing mirror. *Optics and Precision Engineering*, 1, (2004).

[89] S. Y. Lee. *Accelerator physics*. World Scientific Publishing, (2018).

[90] G. H. Golub and C. Reinsch. Singular value decomposition and least squares solutions. In *Linear Algebra*, page 134. Springer, (1971).

[91] M. Sanchez del Rio, N. Canestrari, F. Jiang, and F. Cerrina. SHADOW3: a new version of the synchrotron X-ray optics modelling package. *Journal of Synchrotron Radiation*, 18(5): 708, (2011).

[92] J. Gurland and R. C. Tripathi. A simple approximation for unbiased estimation of the standard deviation. *The American Statistician*, 25(4): 30, (1971).

[93] J. C. Lagarias, J. A. Reeds, M. H. Wright, and P. E. Wright. Convergence properties of the nelder–mead simplex method in low dimensions. *SIAM Journal on optimization*, 9(1): 112, (1998).

[94] G. Geloni, V. Kocharyan, and E. Saldin. Brightness of synchrotron radiation from wigglers. *Nuclear Instruments and Methods in Physics Research Section A: Accelerators, Spectrometers, Detectors and Associated Equipment*, 807: 13, 2016.

[95] B. Singh, R. Bartolini, J. Bengtsson, H. Ghasem, and A. Streun. Lattice options for DIAMOND-II. *Proc. IPAC'18, Vancouver, Canada*, 4050-4053, (2018).

[96] S. G. Alcock, I.-T. Nistea, R. Signorato, R. L. Owen, D. Axford, J. P. Sutter, A. Foster, and K. Sawhney. Dynamic adaptive X-ray optics. Part II. High-speed piezoelectric bimorph deformable Kirkpatrick–Baez mirrors for rapid variation of the 2D size and shape of X-ray beams. *Journal of synchrotron radiation*, 26(1): 45, (2019).

[97] O Marcouille, N Bechu, P Berteaud, P Brunelle, L Chapuis, C Herbeaux, A Lestrade, J.-L. Marlats, A Mary, M Massal, et al. In vacuum permanent magnet wiggler optimized for the production of hard X rays. *Physical Review Special Topics-Accelerators and Beams*, 16(5): 050702, (2013).

[98] S. Koda and Y. Takabayashi. Interference effect of edge radiation at three-pole wiggler section. *Japanese Journal of Applied Physics*, 55(9): 096301, (2016).

[99] H. Winick, G. Brown, K. Halbach, and J. Harris. Wiggler and undulator magnets. *Physics Today*, 34(5): 50, (1981).

[100] A. Dent, G Cibin, S. Ramos, S. Parry, D Gianolio, A. Smith, S. Scott, L Varandas, S Patel, M. Pearson, et al. Performance of B18, the Core EXAFS Bending Magnet beamline at Diamond. In *Journal of Physics: Conference Series*, volume 430, 012023, (2013).

[101] A. Dent, G Cibin, S. Ramos, A. Smith, S. Scott, L Varandas, M. Pearson, N. Krumpa, C. Jones, and P. Robbins. B18: A core XAS spectroscopy beamline for Diamond. In *Journal of Physics: Conference Series*, volume 190 of number 1, 012039. IOP Publishing, (2009).

[102] This idea was proposed in a private communication with Marco Apollonio in Accelerator Physics group in Diamond Light Source.

[103] S. Ramberger and S. Russenschuck. Genetic algorithms for the optimal design of superconducting accelerator magnets. No.LHC-Project-Report-275, (1999).